MICH ST

(57)

FLOWERS, LED

This is to certify that the

thesis entitled

Characterization of the Burst Strength of
Polycrystalline Diamond Thin Films

presented by

Lyndon Edward-David Flowers

has been accepted towards fulfillment
of the requirements for

Master's degree in Materials Science

K. Mukherjee for (E. Case)
Major professor

Date 4/8/94

O-7639

MSU is an Affirmative Action/Equal Opportunity Institution

CHARAC

CHARACTERIZATION OF THE BURST STRENGTH OF POLYCRYSTALLINE DIAMOND THIN FILMS

By

Lyndon Edward David Flowers

A THESIS

Submitted to
Michigan State University
in partial fulfillment of the requirements
for the degree of

MASTER OF SCIENCE

Department of Mechanics and Materials Science

1994

CHARACTE

The bur
testing und
diamond p
deposited
(CVD) pr

DTF
the Si wa
edges by
jected to

Burs
edges a
are disc
pressu

ABSTRACT

CHARACTERIZATION OF THE BURST STRENGTH OF POLYCRYSTALLINE DIAMOND THIN FILMS

By

Lyndon Edward David Flowers

The burst strengths of diamond thin film (DTF) diaphragms were determined by burst testing under uniform loading. Si (100) single crystal wafers were abraded with a 1 micron diamond powder, and photoresist treated to enhance diamond nucleation sites. DTF's were deposited on the abraded Si wafers via a microwave assisted chemical vapor deposition (CVD) process forming DTF on Si wafer samples.

DTF diaphragms were formed by etching small (~2 to 6 mm diameter) holes through the Si wafers. The circular DTF diaphragms thus produced were supported around their edges by the Si wafer. The DTF diaphragms were mounted in a pressure vessel and subjected to an increasing gas pressure until failure.

Bursting of the diaphragms were modeled as circular plates rigidly clamped at the edges and subjected to a uniform load. The maximum stresses and corresponding strains are discussed, and correlations are made between normalized diaphragm radius and burst pressure, and between grain size and burst pressure.

DEDICATION

To my brother and greatest teacher, Michael Adrian Kenworth Flowers.

I would

academic care

point on. I bel

I also acknow

undergraduat

me in the wor

Eldon D. Cas

His funding o

Bill H. Glime

my committe

research.

ACKNOWLEDGEMNETS

I would like to thank Mrs. Norma Pandy-Flowers for giving me the first boost in my academic career, by having me recite the multiplication tables at an early age. From that point on, I believe, my colleagues and I considered myself to be strong in the mathematics. I also acknowledge the moral and financial support of my immediate family through my undergraduate and graduate years. My mother was always near, willing, and able to help me in the worst of times. My father I thank for molding me. I acknowledge my advisor Dr. Eldon D. Case for his belief in my abilities, even when I thought no other eyes could see it. His funding of my project is also appreciated. I would also like to thank my colleagues Bill H. Glime, Kiyoung Lee, and Carol Gamlen for their help in this project. I also thank my committee members Dr. Don Reinhard and Dr. Stan Flegler for their guidience in my research.

Table of Contents

page

List of Tables:

Figure 1 (a
chemical rea
abstracting a
mesh circles
diagonal line
resents hydr

Figure 1 (b
radical then
bon atoms (
large fine m

Figure 1 (c
from the su

Figure 1 (
forms a C-
acetylene r
After [7].

Figure 1 (
another m
depicted

Figure 1
molecule.

Figure 1
atom leav

List of Figures:

Figure 27
sic 1333
character

Figure 28
in this stu
d is the fi

Figure 29
burst in t
and d is t

Figure 3
values w
slight pa
tance fro
to a high
of the de

Figure A
seen at t

Figure A
are obse
of DF-N
indicated

Figure A
0.53 mic
appears
indicated

Figure A
dominat
2.5 micr

Figure A
(100),an
cated.

Figure A
facets d

Figure A7
dominate
mined fro

Figure A
top surfac
ture is se

Figure A
through t
microgra

Figure A
evident t
microgra

Figure A
was dete
on the de
thickness

Figure A
rons was
interfacia

Figure A
microns

Figure A
morpholo
in a pota
bar is ind

Figure A
specimen
and botto
bar is ind

Figure A
with a fe

Figure A
magnific
ture that
see. A 1.

Figure B1
WF=25-1-
the protec
Si and the
Figure B
grains are
was deter
indicated.

Figure B
grains are
mined fro

Figure C
square fa
microns
bar is ind

Figure C
square fa
microns
bar is inc

Figure C
square fa
microns
bar is ind

Figure C
square fa
microns
bar is in

Figure
3.6 micr
tures of
micron

Figure
3.2 micr
tures of
micron

1. Intr

On
around t
the ultim
nology. I
Diamond
Certainly
sidered ev
affinity t

Di
netic tran
room ten
material
the limite
monds, H
their aest
material.
monds ca

Mo
form, as r
of polycry
establishe
one of the

1. Introduction

One of the earliest documentation of diamond dates back to about 46 AD and centers around the early city of London [1]. It is fair to say that diamond has been long regarded as the ultimate in aesthetic value, among materials. Today, with the help of advancing technology, it is amazing to learn that diamond is indeed a unique material in many respects. Diamond is unique in its mechanical, optical, electrical, chemical, and thermal properties. Certainly these superior qualities of diamond compared to other materials were not appreciated even 100 years ago. It is interesting to ponder why people have had such a strong affinity to diamond so long before it's many unique properties were even established.

Diamond's remarkable properties such as hardness [2], broad range of electro-magnetic transparency [3,4], high electrical resistivity [3,5], excellent chemical resistivity at room temperature [3,5], and high thermal conductivity [3], makes diamond the ultimate material candidate for many applications. However, the high cost of natural diamonds and the limited knowledge of its growth mechanism (which limits the synthetic abilities of diamonds) have kept diamonds from wide spread use. It is not likely that diamonds will loose their aesthetic appeal to people, therefore natural diamonds may never become a cheap material. The ability to produce cheap synthetic diamonds seems the only way that diamonds can possibly see wide spread use.

Most of the well established properties of diamond are based on its single crystal form, as natural single crystal diamonds were always available for testing. The properties of polycrystalline diamond however, especially its growth mechanism, are not as well established. Synthetic diamond has only become popular in recent decades, which may be one of the reasons why many of their properties are not well established. It is

conceivable
diamond's p
diamonds w
dependent

The c
scattering
transparen
than at gra
of polycry

Wi
character
someday
of practi
strengths
related t

1.1 Dia

Many si
can be u
as a goo
insulato
that mig
heat co

conceivable that some of the properties of single crystal diamond might also be found in diamond's polycrystalline form. However, it is unlikely that all the properties of the single diamonds will be realized in polycrystalline diamond. Properties that are grain boundary dependent might be inherent in polycrystalline diamond.

The optical transparency of polycrystalline diamond may be significantly affected by scattering due to grain size and concentration. Grain boundary impurities might affect the transparency of polycrystalline diamond by increasing its absorbancy. Impurity concentration at grain boundaries might also affect the diffusive, electrical and chemical properties of polycrystalline diamond.

With the ability to synthesize single and polycrystal diamonds has come the desire to characterize and to control these properties. This desire is certainly based on the hope of someday harnessing the aforementioned exceptional properties of diamond for a multitude of practical uses. To this end much research is being done. In this investigation the burst strengths of diamond polycrystalline thin films were tested under uniform loading and related to film thickness, diaphragm diameter and grain size.

1.1 Diamond Thin Films (DTF)

Many situations exist in which the properties of a diamond polycrystalline thin film (DTF) can be utilized. Diamond's high electrical resistivity and good heat conductivity suggests it as a good coating for integrated circuits. The diamond polycrystalline coating, being a good insulator, would protect the integrated circuit from shorting out due to dust particles etc. that might fall on the integrated circuit. The diamond polycrystalline coating, being a good heat conductor, would also enhance heat dissipation. Diamond's extremely high hardness makes it u

to the IR

erties of h

the requi

Norans e

DT

propertie

ability to

Th

in engin

ers usin

1.2 M

The ma

groupe

relativ

metho

peratu

used c

makes it useful as a wear protective coating. Diamond's optical transparency from the UV to the IR region, including the visible, makes it a candidate as a window. Diamond's properties of high chemical inertness, and optical transparency at high temperatures would fill the requirements for many unique window applications such as might be found in some (Noran) energy dispersive x-ray analysis equipments.

DTF's may be fabricated to be piezoresistive [6], which, combined with the other properties mentioned, suggests DTF's possible use in pressure sensing devices with the ability to operate in harsh environments.

The results of this experiment may someday be useful information to anyone involved in engineering polycrystalline diamond windows and/or possibly future pressure transducers using piezoresistive polycrystalline diamond diaphragms.

1.2 Methods of CVD

The methods employed to fabricate diamond single crystals and polycrystals can be grouped into five categories [3].

(1) Conversion of graphite to diamond by dynamic shock. This method produces relatively small diamond crystals.

(2) Conversion of graphite into diamond by a high temperature, high static pressure method. This process yields relatively small crystals, as in (1).

(3) Diamond formation from graphite by contact with a molten metal at high temperature and pressure which is the method used to produce most of the larger single crystals used commercially.

(4) A method similar to (3) which uses small diamond crystals as a precursor and

ar proc

(

types of

Th

More p

diamo

1.3 Pr

An acc

ferent

tion pr

config

ments

hydroc

ferent

$(C_2H_2$

[7].

1.3.1

A simp

acetyl

mond

growth

can produce diamonds of well-controlled impurity level and produces large single crystals.

(5) Chemical vapor deposition (CVD) of diamond thin films (DTF) onto different types of substrates.

The chemical vapor deposition (CVD) method is employed in this investigation. More precisely, a microwave assisted plasma CVD method was used to deposit the DTF's (diamond thin films) onto (100) single crystal Si wafers.

1.3 Proposed CVD Growth Mechanisms

An accepted mechanism describing the growth of DTF's has not yet been established. Different mechanisms trying to accommodate all the different trends observed in the deposition processes have been proposed, but many questions are yet unanswered and many conflicting propositions exists [7,8]. A major disagreement exists on what is the key monomer(s) responsible for the growth of diamond. Researchers generally agree that some hydrocarbon species is responsible for the diamond growth in CVD processes. Of the different hydrocarbon species suggested as being responsible for diamond growth, acetylene (C_2H_2), and methyl (CH_3), seems to be the most commonly suggested monomer species [7].

1.3.1 A Simple Proposed Mechanism

A simple mechanism was proposed [7] in which a sequence of chemical reactions utilizing acetylene, from the pyrolysis of methane, lead to the formation of sp^3 carbon-carbon or diamond bonds. The continued formations of these sp^3-bonds leads to epitaxial diamond growth. This simple mechanism (Figure 1) can be applied to any plane; the dominant {111}

Figure 1
hydrogen
ta to 1
ties with
gen atom

Figure 1
to the ad
represen

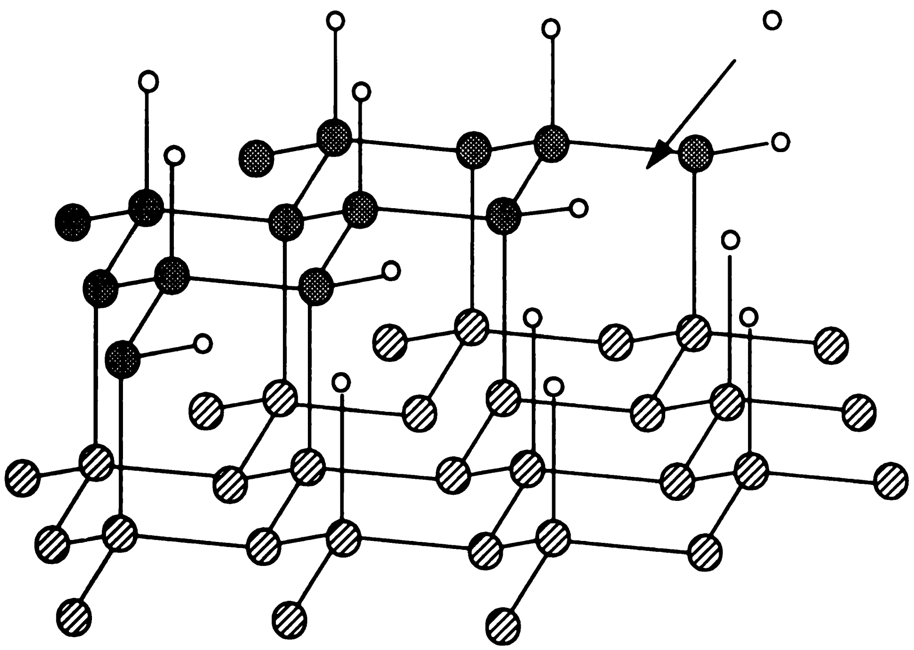

Figure 1 (a). Proposed growth mechanism showing the sequence of chemical reactions. A hydrogen atom activates the surface by abstracting a surface H atom creating a radical site, 1(a) to 1(b). The large coarse mesh circles are the top layer carbon atoms and the large circles with diagonal lines are lower layer carbon atoms. The small circles represents hydrogen atoms. After [7].

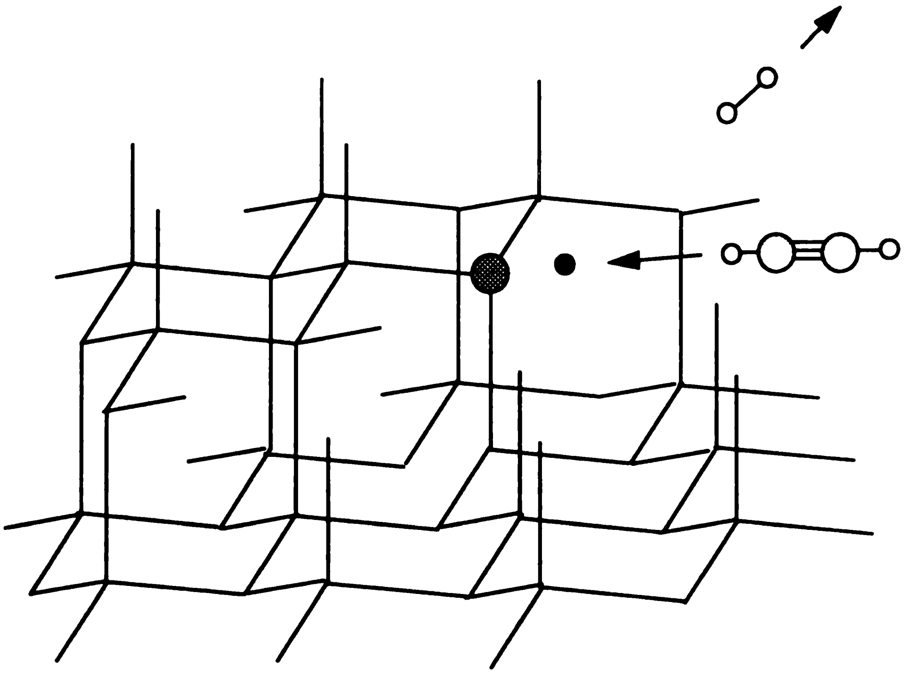

Figure 1 (b). An acetylene molecule is added to the radical site. The radical then propagates to the added molecule, 1(b) to 1(c). The carbon atoms of the added acetylene molecule are represented by the large fine mesh circles, and the radical site by a black dot. After [7].

Figure 1
carbon at

Figure 1
the carbo
the adja

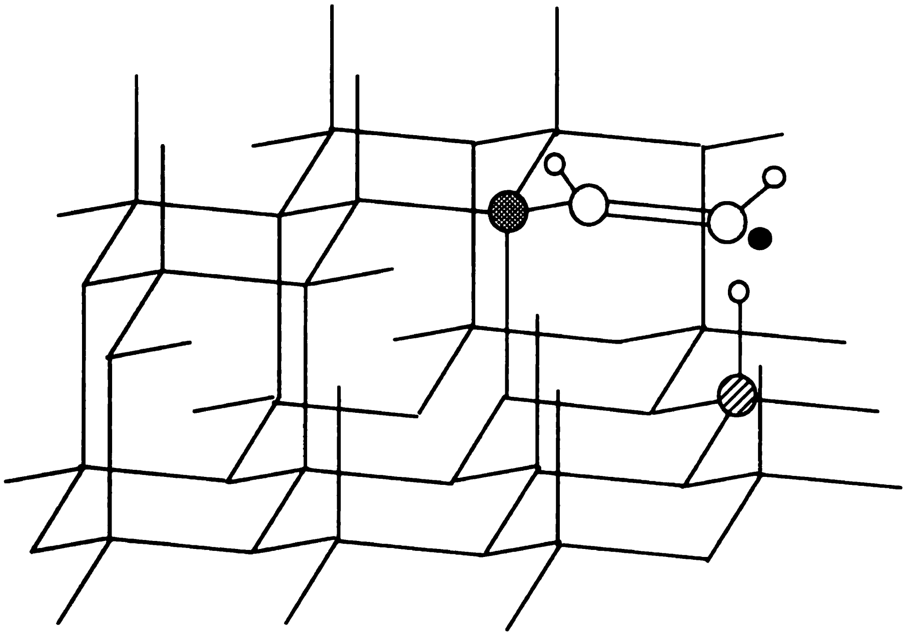

Figure 1 (c). The radical then bonds to the hydrogen atom abstracted from the surface carbon atom of the lower layer, 1(c) to 1(d). After [7].

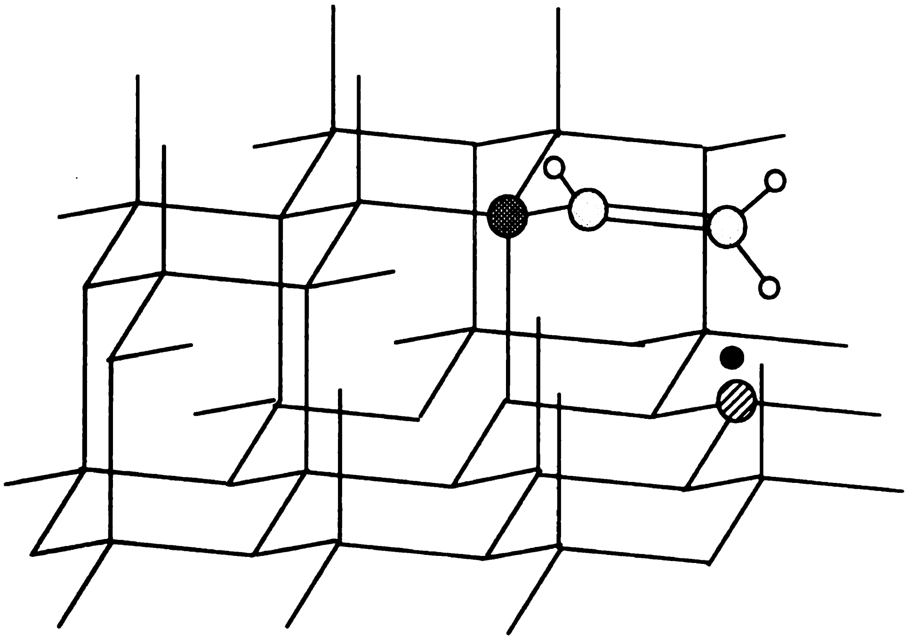

Figure 1 (d). The carbon radical available on the lower layer then forms a C-C bond with the carbon atom of the originally added acetylene molecule. This creates a free radical on the adjacent carbon, 1(d) to 1(e). After [7].

Figure 1
cule sta

Figure

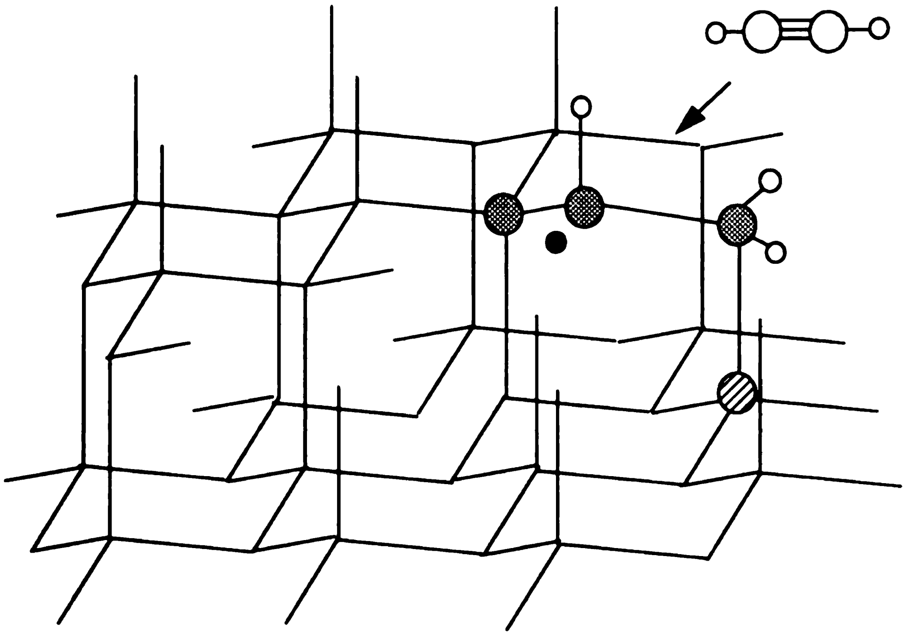

Figure 1 (e). The sp^3 bond is formed by this step. The addition of another acetylene molecule starts a similar reaction sequence which is depicted in (f) through (i). After [7].

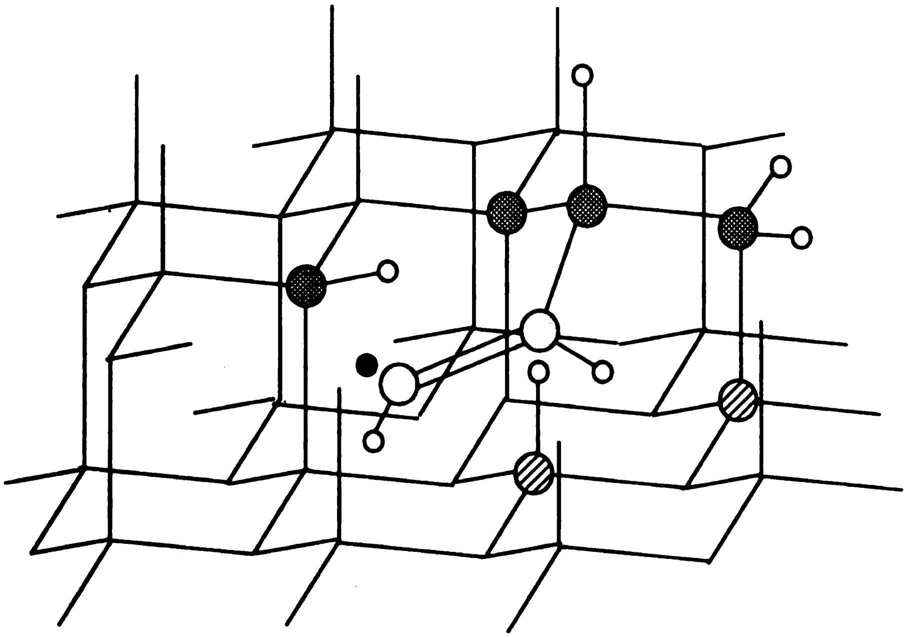

Figure 1 (f). The radical site is propagated to the added acetylene molecule. After [7].

Figure 1 (g)
on radical.

Figure 1 (h)
newly added

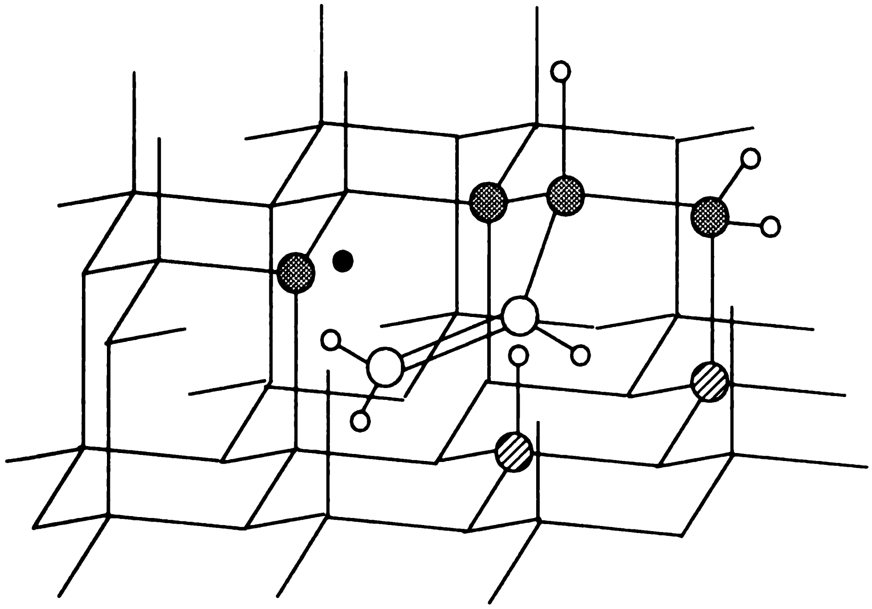

Figure 1 (g). A hydrogen atom is abstracted from a top layer carbon atom leaving a carbon radical. After [7].

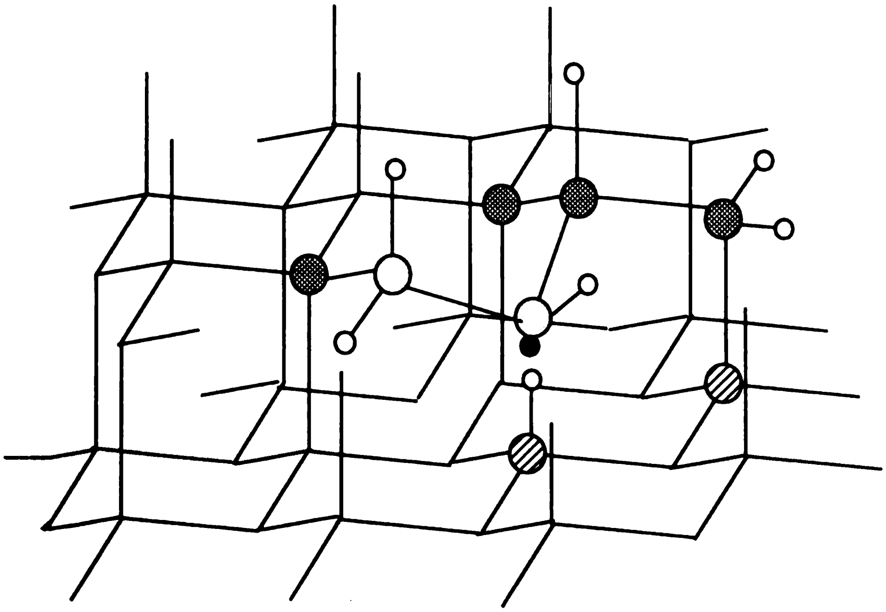

Figure 1 (h). The carbon radical forma a C-C bond with another carbon atom from the newly added acetylene molecule propagating the radical to the molecule. After [7].

Figure 1
carbon at

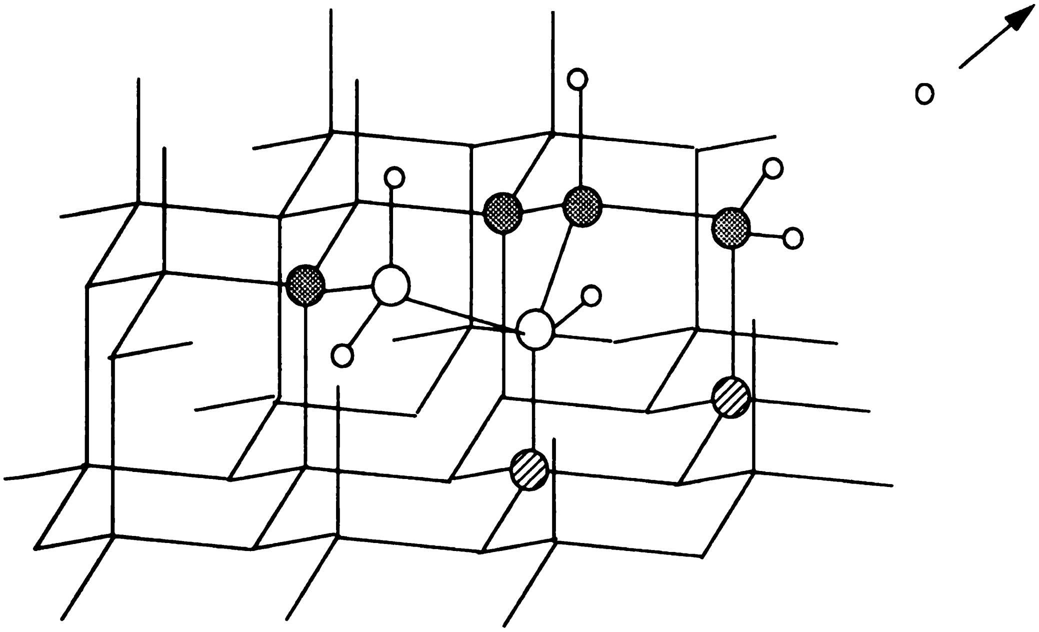

Figure 1 (i). The radical on the acetylene molecule forms a C-C bond with a lower layer carbon atom while abstracting a hydrogen atom from the lower layer. After [7].

an

thr

C-F

are

Fig

and

bin

asy

ther

in

in

in

dee

CH

res

1.3

Hy

gen

stu

Pro

and {100} planes for example. A hydrogen atom activates and removes another H atom from the surface plane of the diamond to produce a radical site (Figure 1 (a) to 1 (b)). The C_2H_2 acetylene molecule then attaches itself to the radical site propagating the radical (Figure 1 (b) to 1 (c)) which abstracts a hydrogen atom from the carbon atom of the lower layer (Figure 1 (c) to 1 (d)). The carbon radical now available forms a C-C bond with the carbon atom of the originally added acetylene molecule.creating a free electron on the adjacent carbon (Figure 1 (d) to 1 (e)). The hybrid sp bond of the acetylene molecule is transformed to a sp^2 bond upon attaching itself to the solid carbon atom. Another C_2H_2 monomer species then attaches itself to this radical site in a similar manner. This sequence of C_2H_2 addition to radical sites on the diamond surface propagates to form the DTF (Figure 1 (e) to 1 (i)).

It is proposed elsewhere however, that C_2H_2 is an insignificant species in the deposition of DTF's [8]. This conclusion is based on data that shows the mole fraction of C_2H_2 in the deposition atmosphere to be less than $1.0\text{x}10^{-7}$. A mole fraction of $1.0\text{x}10^{-7}$ was deemed too low to be responsible for film formation. Besides CH_4, whose mole fraction is 0.7 in the deposition atmosphere, only C_2H_6 and CH_3 have concentrations above 10^{-7}, thus CH_4, C_2H_6, and CH_3 were suggested to be the only monomers that could possibly be responsible for the diamond film formation [8].

1.3.2 Role of Hydrogen in DTF Deposition

Hydrogen is used as the carrier gas in most CVD processes. Methane (CH_4) and often oxygen (O_2) gases in small amounts are added to an abundance of H gas to makeup the deposition precursor gases. The two most important roles of hydrogen atoms in the deposition process is (1), hydrogen preferentially etches the graphitic/amorphous phases of carbon over dia

tions res

over the

ducing a

mechanis

Hy

such as h

increasing

sen for th

ature [14,

methane, (

increase in

increase in

increase.

Hyd

(ERD) spe

nuclear re

wave plas

1.3.3 Ro

The additi

tion that is

added to t

over diamond phase [7,9,10,11,12], and (2), hydrogen suppresses of the aromatic hydrocarbons responsible for diamond [9,13]. The preferential etching of the non-diamond phases over the diamond phase by hydrogen causes diamond growth rate to dominate, thus producing a quality diamond film. The preferential etching effect of hydrogen is the primary mechanism in CVD diamond formation [2].

Hydrogen is a known impurity within diamond thin films (DTF's) [4]. Impurities such as hydrogen, may increase the compressive stresses in a film [14]. It is thought that increasing the deposition temperature decreases the H content [4,14], which may be the reason for the decrease in the compressive stress associated with increased deposition temperature [14,15]. The overall intrinsic stresses of the film is decreased by increasing the methane, CH_4, concentration of the precusor gas. This intrinsic stress decrease is due to an increase in the compressive stresses in the film. The compressive stresses are caused by the increase in the hydrogen concentration which is associated with the methane concentration increase.

Hydrogen content in deposited diamond can be determined by elastic recoil detection (ERD) spectroscopy [14,18] and by nitrogen nuclear reaction analysis [4,14]. Nitrogen nuclear reaction analysis has been used to determine that films grown by a particular microwave plasma assisted CVD process contained 0.7 to 8.0 percent hydrogen [4].

1.3.3 Role of Oxygen in DTF Deposition

The addition of oxygen to the precursor gases decreases the quantity of non-diamond carbon that is codeposited with the diamond. Oxygen also increases film growth rate [5]. When added to the methane-hydrogen precursor gas mixture, oxygen increases the effective

hydr
carbo
in gra
growt
ing.

1.4 L

A thin
appro
interfa
after a
growt
partic
formi
[18], a
faster

1.5 D

Severa
precur
tempe
and qu

hydrogen concentration in the deposition atmosphere [13]. Hydrogen etches non-diamond carbon preferentially (section 1.3.2), therefore an increase in its effective concentration aids in graphite/amorphous carbon suppression. The addition of oxygen thus greatly affects film growth by increasing the hydrogen concentration and hence the effects of hydrogen etching.

1.4 Interface between DTF and Si Substrate

A thin layer of SiC is found between the DTF and the Si substrate [12]. The SiC layer is approximately 0.25 microns thick and may be continuous across the entire diamond/silicon interface [12]. Residual diamond particles (diamond seeds) left embedded in the Si wafer after abrasion by diamond powder or diamond paste act as nucleation sites for diamond film growth [17]. The deposited DTF grows directly on some or all of these embedded diamond particles. Initially the crystals grow laterally until they meet, and then they grow upwards forming columnar structures (Figure 2). The diamond film deposition rate is initially high [18] and the SiC layer (perhaps a reaction product) may dominate initially and form much faster than the diamond crystal.

1.5 Deposition Parameters and Their Effects

Several deposition parameters affect the films synthesized in a CVD process. The types of precursor gases used in deposition, the concentration of the precusor gases, the deposition temperature, the deposition pressure, and the energy source, can each affect the growth rate and quality of the DTF synthesized in a CVD process.

Figure 2. S
mond seed
growth is i
ing column

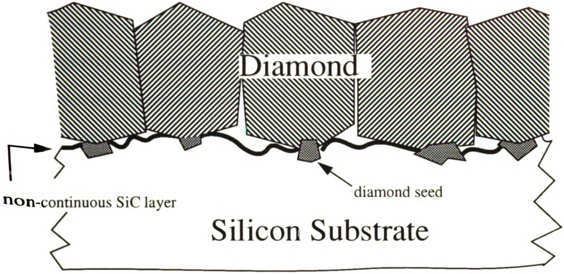

Figure 2. Sketch of DTF /Si substrate interface. The DTF and Si interface showing diamond seeds embedded in Si wafer. Grains nucleate and grow from these sites. Crystal growth is initially lateral. Upon contacting their neighbors the crystals grow upward forming columnar structures.

1.5.1 I

The ty

signi

concen

made i

mecha

I

ane-hy

bon sp

for the

and gr

indep

phous

films.

A

hydro

cence

C

as an e

inert g

under

[9]. H

He car

1.5.1 Deposition Precursor Gases

The types and relative concentrations of the precusor gases used in CVD processes have a significant effect on the nature of the diamonds produced. Varying the types and relative concentrations of the precursor gases is cheap and simple. This type of variation is often made in CVD processes to produce desirable diamonds and/or to study diamonds growth mechanism.

The most common gas combination used in diamond film CVD processes is a methane-hydrogen (CH_4-H_2) mixture. Methane is the source of the carbon which forms the carbon sp^3 bonds that characterizes diamond. Hydrogen (section 1.3.2) is primarily an etchant for the other carbon phases codeposited with diamond. Carbon phases such as amorphous and graphitic phases have a lower Gibb's free energies than diamond, therefore their codeposition with the diamond phase is always expected [11]. The etching of the amorphous and graphitic carbon phases is the most important process in the CVD of diamond films, therefore the etching effect of hydrogen is quite necessary.

Another precursor gas combination used in diamond film CVD is a methane-oxygen-hydrogen (CH_4-O_2-H_2) mixture [13] where the oxygen increases the effective hydrogen concentration in the deposition atmosphere.

Other gases may also be used in the CVD of diamond films, but their uses is usually as an experimental means of studying the growth mechanism of diamond. For example, the inert gases helium (He) and argon (Ar) were used in the CVD of diamond films to better understand the role of hydrogen in the deposition of diamond. In one particular experiment [8], H_2 (the usual carrier) was replaced by helium. CH_4 and H_2/O_2 were alternated in the He carrier as the deposition precursor gases. A substantial diamond growth rate was noticed wi

wi

rep

rev

ind

1.5

Ty

to S

dep

the

con

ind

cen

cur

hyd

oxy

Tur

1.5.

The

mon

which might indicate that hydrogen as a suppressor to the diamond forming aromatic is a significant process in the CVD of diamond. In a simulation experiment [9], Ar was used to replace H_2 to better understand hydrogen's role in the growth mechanism of diamond. The results suggested that suppression of aromatic formations by hydrogen was the key factor in diamond formation.

1.5.2 Concentrations of Precusor Gases

Typical the CH_4-H_2 mixture used for CVD of DTF ranges from approximately 0.1 percent to 5.0 percent methane in hydrogen [4,12,14]. However, a higher quality diamond film is deposited at the lower CH_4 to H_2 ratios, from approximately 0.5 to 1 percent [14,18]. As the methane to hydrogen ratio increases, the likelihood of codepositing a non-diamond carbon phase also increases. The film growth rate also increases with the concentration increase of methane in hydrogen [12].

In the CH_4-O_2-H_2 systems, the concentration range of O_2 may be from 0.5 to 5 percent [13]. The film growth rate increases with increasing oxygen concentration in the precursor gases [13], and as mentioned earlier, oxygen addition effectively increases the hydrogen concentration thus improves the quality of diamond film produced. The optimal oxygen concentration range seem to be 0.5 to 1.0 percent of the precusor gases at 45 -50 Torr [10].

1.5.3 Deposition Temperature

The diamond film growth rate also increases with temperature, but the growth rate of diamond reaches a maximum and further temperature increase leads to the increased formation

of graphite [7,18]. The temperature at which transformation from diamond formation to graphite formation occurs is not reported. Graphite formation also exhibits a temperature maximum but at a higher temperature than that of diamond [7].

The usual substrate temperature range for DTF deposition is 700° C to 1,300° C [10,13,16]. One might assumed that as the temperature increases, so would the surface mobility for diffusing hydrogen atoms therefore increasing the purity (less hydrogen impurities) of the diamond films produced at the higher growth rate [11]. However, for the temperature range of 600 °C to 887 °C, no correlation between deposition temperature and the film's hydrogen content was determined [4].

Intrinsic tensile film stress also varies strongly with deposition temperature [14,15]. The intrinsic stress increases as deposition temperature increases. The intrinsic film stress versus deposition temperature relationship might be attributed to the non-diamond (sp^2) incorporated during deposition [14]. Higher temperatures corresponds to a lower non-diamond content in the deposited film [14]. Lowering the non-diamond content increases the film's tensile stress by lowering the compressive stresses caused by the non-diamond.

The (111) and (100) faces of diamond preferentially grow in the temperature range of 750° C to 1000° C. At the higher temperatures in this range the (111) face dominate, whereas the (100) faces dominate at the lower temperatures of this range [19].

1.5.4 Deposition Chamber Pressure

Variation of the deposition chamber pressure in a diamond CVD process affects film morphology and film growth rate [10]. The morphology is the strongest determinant of the mechanical properties of synthetic diamond [20]. The deposition chamber pressure

mate
even
dep
pres

1.5.5

Sever
ments
waves
which

A

for mo
of ene
diamo
likely
atomic
lished.
which

A

ical pro
employ
ties of t
effect o

therefore would seem a reasonable parameter to use in tailoring the synthetic DTF. However, the deposition chamber pressure is not a parameter that is usually varied to tailor the deposited diamond thin film (DTF). Film growth rate increases with increasing chamber pressure [10].

1.5.5 Deposition Energy Source

Several different types of energy (heat) sources are used in the CVD of diamond. Hot filaments[19], high temperature furnaces [11], high-intensity infrared lamps [18], and microwaves [4] are some of the methods used to excite the precursor gases to a plasma state from which diamond is chemically deposited.

As mentioned earlier, the morphology of synthetic diamond is the determining factor for most of the physical properties for which diamonds are made [20]. The different types of energy sources used are not known to have any special effect on the morphology of the diamond they produce [20]. The many different methods of plasma generation in use is likely due to a search for the most economic source for the CVD of diamond. The most economic method to generate the heat necessary for the CVD of diamond is still not established. Perhaps there does not exist a most economic method. The lowest temperature at which DTF's can be synthesized may be the most economical.

Although the heat source is generally accepted as not playing any role in the mechanical properties of the synthetic diamond produced, it seems likely that the heat source employed may be important to some non-mechanical properties. Non-mechanical properties of the CVD diamond which are dependent on impurity content and/or possible the effect of heat gradients on the specimen could make the energy source a non-trivial

depositi
polycry
energy
depend
dictated
amount

A
uniform
tion cha
mixing
can be s
greater t
plicates
source fo

Ge
cussed in
crystallin
CVD pro

deposition parameter. If the types and concentrations of impurity in a single crystal or a polycrystalline thin film effect its transparency, electrical, or chemical property, then the energy source would be important. The impurity of a CVD diamond will be, to some extent, dependent on the environment in the deposition chamber. The deposition chamber is often dictated by the energy source used., thus the energy source may influence the types and amount of impurities incorporated in the synthesized diamond film.

Another non-mechanical property that might be influenced by the heat source is the uniformity of the thickness of the diamond film produced. The heat gradient in the deposition chamber is related to the thickness variation of polycrystalline thin films [21]. Minimizing the heat gradient would produce films of more uniform thickness. Heat gradients can be strongly dependent on the energy source, as in convection oven the heat gradient is greater than in a microwave oven. These considerations coupled with controlling cost complicates the task of establishing any one energy source as the most economical energy source for the CVD of diamond.

Getting away from the complexity of the CVD process, the burst test experiment discussed in this thesis is intent on the characterization of the mechanical properties of polycrystalline diamond thin films (DTF's). The DTF's were deposited by a microwave assisted CVD process.

2. Ex

water

[illegible]

place

CVD

ten to

ry the

gen ga

ured.

critica

ity of

mecha

2.1 Si

T

site de

nucleat

crystal

centrati

A

ation sit

2. Experimental Procedure

Diamond polycrystalline thin films (DTF's) were deposited on Si single crystal wafers. Circular holes were etched through the Si wafers to produce circular DTF diaphragms. These diaphragm were subsequently loaded to failure with gas pressure.

The deposition of the polycrystalline diamond thin films onto Si wafers was accomplished with the use of a microwave plasma reactor (Figure 3) via a microwave assisted CVD process. Circular holes were etched through the Si wafers with a KOH etching solution to produce circular DTF diaphragms. The circular diaphragms, supported at their edges by the Si wafer, were then mounted into a pressure vessel and uniformly loaded with nitrogen gas pressure to failure. The increasing pressure of the nitrogen gas was closely monitored, and the pressure at failure was recorded for each diaphragm that was burst. The critical load at failure, film thickness, diaphragm diameter, average grain size, and the quality of diamond polycrystalline film were all considered in the characterization of the mechanical integrity of the DTF diaphragms.

2.1 Si Wafer Pre-deposition Treatment

The initial Si wafers were abraded with diamond powder to increase their nucleation site densities prior to deposition. Microscopic scratches on Si surfaces are known to act as nucleation sites for diamond crystals during the CVD of diamond on Si wafer [5,12]. Single crystal Si wafers were therefore abraded on one side to increase their nucleation site concentration.

A photoresist pre-deposition treatment was also used to like-wise increase the nucleation site density on later specimens tested. The photoresist treatment is discussed in water fl

base pl

TCD f

type 2

Exhau

Figure

diamon

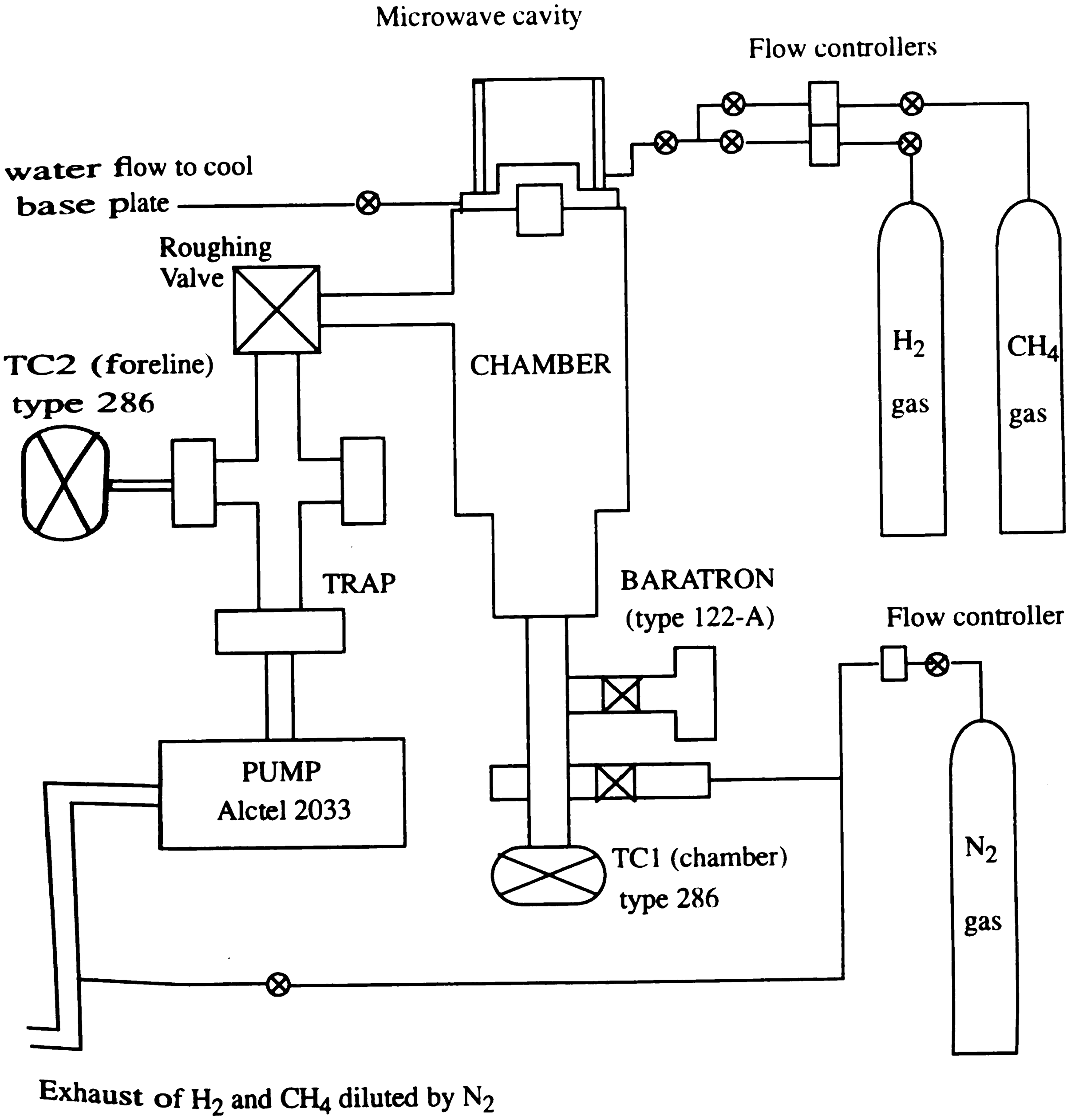

Figure 3. A schematic diagram of the microwave plasma reactor used to produce the diamond thin films utilized in this study.

eth

2.1.1

Sing

eter ar

ised

ultured

A

with t

approx

um fr

the top

was pl

sprink

of the

them t

erated

other w

mainta

T

fingers

method

duced b

section 2.9.1.

2.1.1 Abrading of the Si Wafers

Single crystal Si wafers used were received as circular disks, approximately 8 cm in diameter and 0.25 mm in thickness. The wafers each had a dull unpolished side and a shiny polished side. The shiny polished sides on which the DTF were subsequently deposited were abraded before deposition.

Abrasion was achieved by placing a wafer into a shallow glass culture dish (Corning) with its shiny polished side up (Figure 4). The diameter of the Corning glass dish was approximately 1.5 cm greater than that of the circular wafer. The edges of the dish were 1cm high. Approximately 0.015 gram of a one micron diamond powder was sprinkled over the top of this polished surface and evenly distributed. A second wafer, the wafer of interest, was placed with its polished side down on top of the one micron diamond powder that was sprinkled over the first wafer. With the diamond powder between the two polished surfaces of the wafers, the fingers were used to gently apply a mild pressure to the wafers forcing them together (Figure 4 (b)). Under this applied pressure, a circular motion was then generated with the fingers to rotate the polished side of one wafer on the polished side of the other wafer (Figure 4(c)). This circular motions, with a light pressure from the fingers, was maintained for approximately 10 minutes to achieve abrasion.

The abrasion step likely was not very reproducible. Neither the force applied with the fingers, nor the exact amount of diamond powder used was measured. However, a possible method to improve the repeatability of abrasion is to characterized the micro-scratches produced by abrading. Determining the size, depth, and area density of the scratches caused by lamina

Figure
abrade
surface

Figure
fingers,

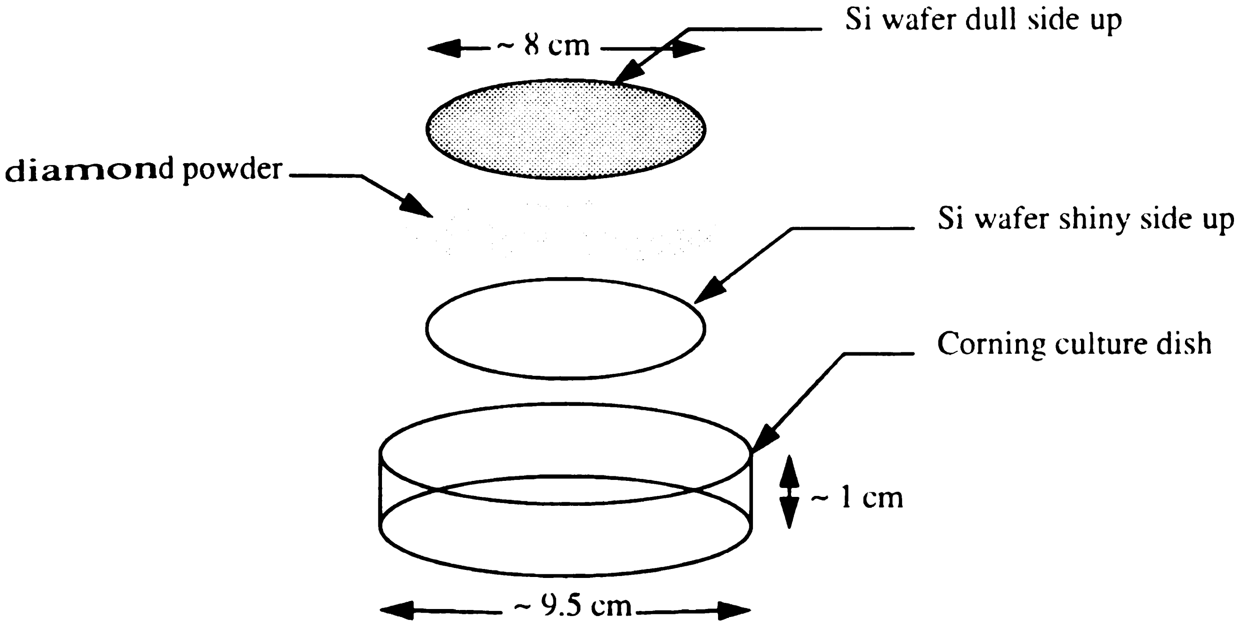

Figure 4 (a). Abrading of Si wafers. The shiny polished sides of the Si wafers were abraded with 1 micron diamond powder. Diamond powder was place between the polished surfaces of two wafers, and the sandwich placed in a dish.

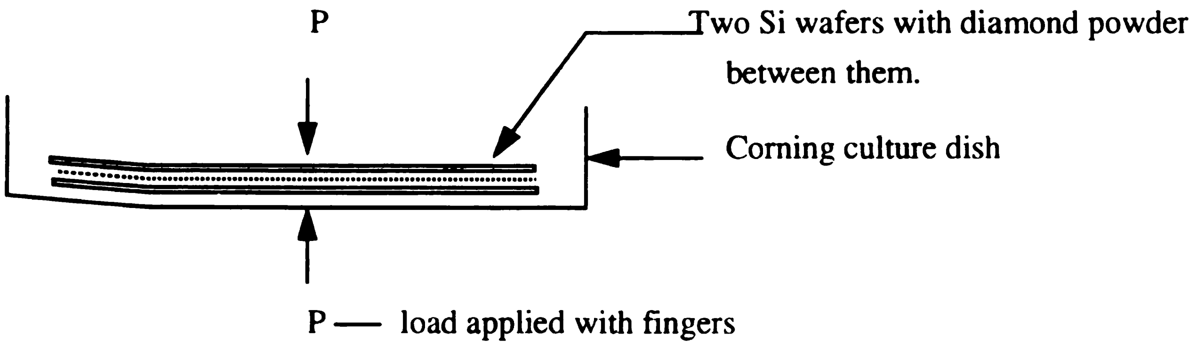

Figure 4 (b). A light load (P) was applied to the Si/diamond powder sandwich with the fingers.

Figure

side to

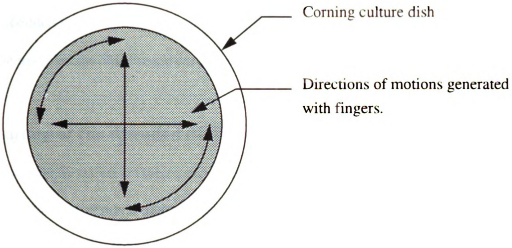

Figure 4 (c). The motion applied to the wafers with the fingers is as indicated. Twisting, side to side, and back and forth motions were applied to the sandwich.

irradia

des lef

ions co

2.1.2 (

After a

was ne

wafers

22 R-

5 minu

optimiz

Dust-O

air onto

The wa

blow-dr

taminati

not appl

2.1.3 F

The abr

the diam

tion to a

wafers. S

abrading and the size, shape, and distribution of the residual (seed) diamond powder particles left embedded in the Si wafer from abrading may allow reproduction. Such determinations can be made on the SEM using surface replication techniques.

2.1.2 Cleaning of the Abraded Si Wafers

After abrading the Si wafers on their polished sides with the 1 micron diamond powder it was necessary to clean residual diamond particles from these surfaces. The abraded Si wafers were ultrasonically rinsed (using a Fisher Scientific Ultrasonic Cleaner model B-2200R-1, Branson Cleaning Equipment Company, Shelton, CT. USA) first in methanol for 5 minutes, then in acetone for another 5 minutes. Each rinsing bath was used only once to optimize the cleaning efficiency. After ultrasonic rinsing, the wafers were blow-dried with Dust-Off Plus (Faclon Safety Products, Inc., Branchburg, N.J. 08876) directing bursts of air onto a desired area. Dust-Off Plus is a hand held canister of inert gas with a thin nozzle. The wafers were held approximately 5 inches from the nozzle of the canister while being blow-dried. Wafers were blow-dried to speed drying and possibly avoid minimal dust contamination. The blow-drying procedure however, was not considered to be critical and was not applied to later wafers.

2.1.3 Fracturing of the Si Wafers

The abraded Si wafers were fractured to a final size of approximately 1 cm by 1 cm before the diamond films were deposited on them. The wafers were fractured prior to film deposition to avoid possibly disturbing the interfaces between the deposited films and the Si wafers. Specimens from sets DF-N1, DF-N2, DF-N4, and DF-N5 were processed in this manc

(

water

amin

was m

with t

under

mach

angth

paper

paper

piece

mate

had t

fractu

5. wa

was r

manner.

Controlled fractures were obtained by a particular method (Figure 5). The abraded wafers were laid on a hard and flat surface; a table top. A diamond tip pen was used to create a minute -just visible- scratch on one edge of the abraded wafer (Figure 5 (a)). The wafer was then flipped over on two plies of tissue paper and an increasing load was slowly applied with the diamond pen tip until fracture occurred (Figure 5 (b)). The tissue paper placed under the wafers allowed the wafers to bend until it fractured. In this manner a complete fracture propagated across the wafer. The fracture initiated at the scratch and propagated at a right angle away from that same edge (Figure 5 (c)). After complete fracture the tissue papers were relatively undisturbed and many breaks were made on the same pieces of tissue paper. Fractures were orthogonal and mostly free of any chipping. The final size of each piece of Si wafer before diamond film deposition was approximately 1 cm by 1 cm.

Later specimens however, were received as large Si wafers (semicircles approximately 9.7 cm in diameter) with a DTF already deposited on them. The specimens therefore had to be fractured with the DTF's already adhered to them. These specimens were also fractured to 1 cm by 1cm squares.

Although the later specimens were fractured with the DTF's already attached to the Si wafers, a severe effect to the adhesion of the DTF on the Si substrate due to fracturing was not anticipated.

igure

igur

pre

rack

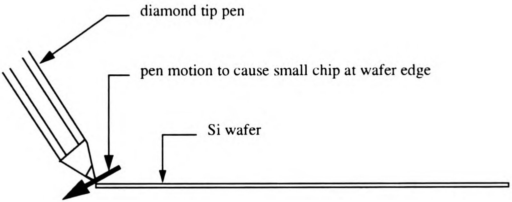

Figure 5 (a). Fracturing of Si wafers. The edge is first chipped with the diamond tip pen.

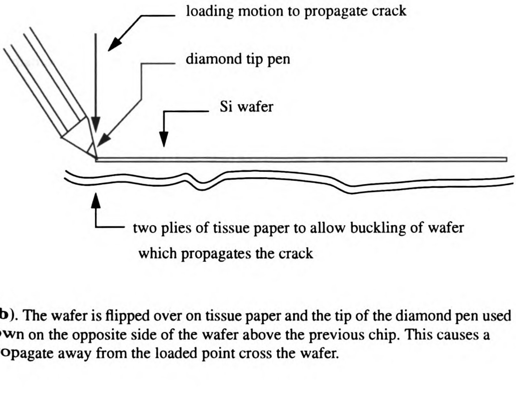

Figure 5 (b). The wafer is flipped over on tissue paper and the tip of the diamond pen used to press down on the opposite side of the wafer above the previous chip. This causes a crack to propagate away from the loaded point cross the wafer.

Figur

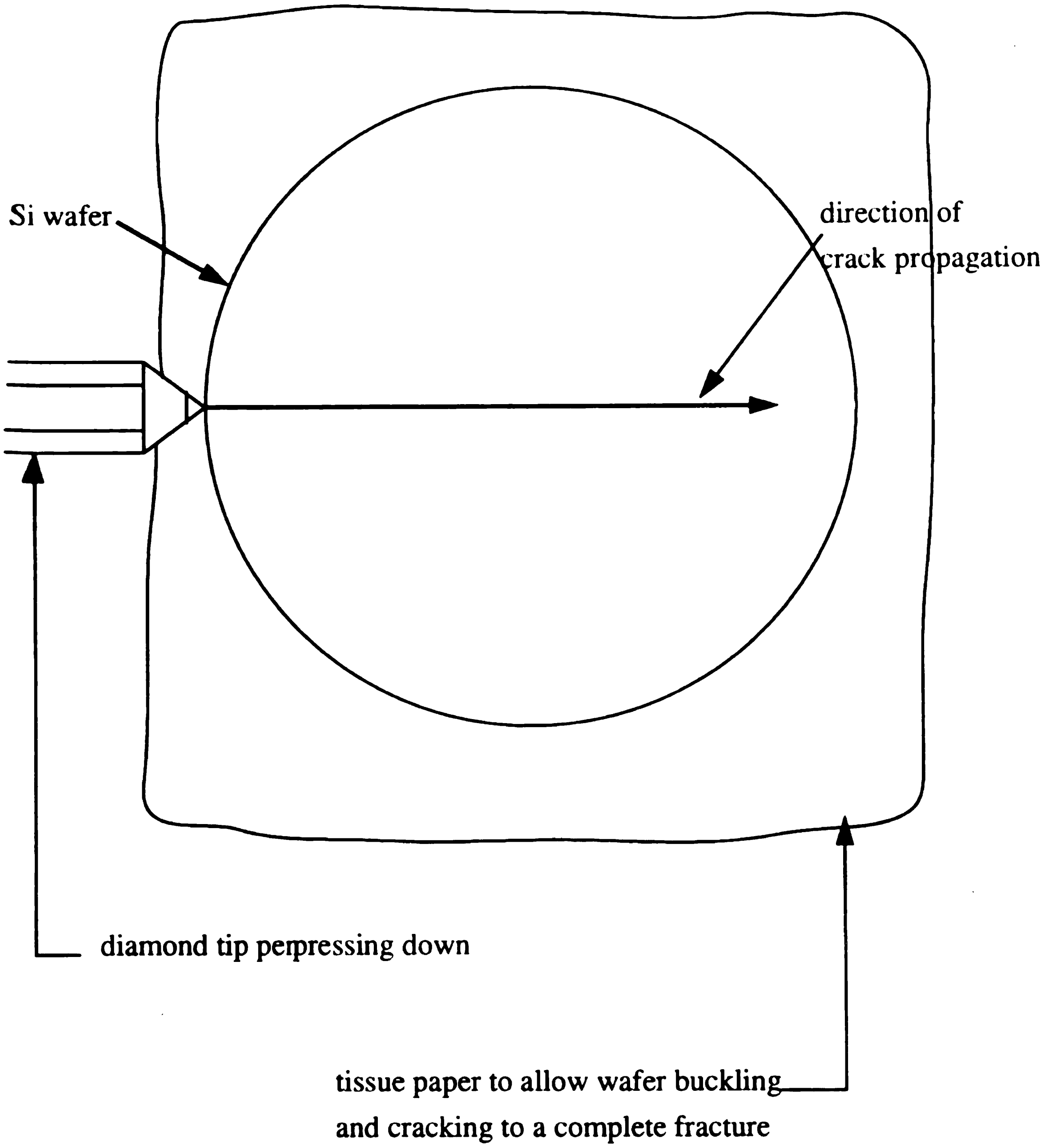

Figure 5 (c). Top view of (b) showing the crack propagation direction

2.2 Film

2.2.1 Mi

DTF's we

CVD Th

pressure

osition pr

Pump-do

was very

was calib

App

% with th

directly to

3 cm by 3

0.5 mm.

the Si wa

In th

approxim

ning. The

that was

in diamet

of Si waf

ter of the

was place

2.2 Film Deposition

2.2.1 Microwave Disk Reactor Preparation

DTF's were deposited on (100) single crystal Si wafers by microwave plasma assisted CVD. The microwave deposition system (Figure 3) was usually kept at or near deposition pressure as deposition was done at ~ 45 Torrs. If however the system was not at or near deposition pressure, approximately 10 hours were required for the system to be pumped down. Pump-down was achieved by a roughing pump followed by a diffusion pump. This process was very time consuming because the pressure transducer (Baratron type 122-A - Figure 3) was calibrated to zero at a pressure which was less than the transducer's resolution.

Approximately nine 1 cm by 1 cm Si wafers were placed on a graphite plate (Figure 6) with their abraded sides facing up. The abraded sides of the wafers were thus exposed directly to the microwave stimulated plasma. The graphite plate was square, approximately 3 cm by 3 cm, with rounded edges and a slight rim. The rim was approximately 0.5 mm by 0.5 mm. An advantage in using a graphite plate was that it reduced the thermal gradients in the Si wafers [21].

In the microwave reactor chamber (Figure 7), a heavy transparent fused silica dish approximately 8 cm deep, 8 cm outer diameter, and 1cm thick, was lifted off a rubber O-ring. The graphite plate with the nine pieces of Si wafers was placed on a fused silica tube that was under the heavy dish. The fused silica tube, 3.7 cm high and approximately 2 cm in diameter, sat vertically on one of its ends and the graphite plate carrying the nine pieces of Si wafers was placed on the top end. The fused silica tube was positioned under the center of the heavy cylindrical dish. After the graphite plate with the nine pieces of Si wafers was placed on top of the vertically standing fused silica tube, the heavy cylindrical dish was

~1.5 mm

mm

Figure 6

Each pie

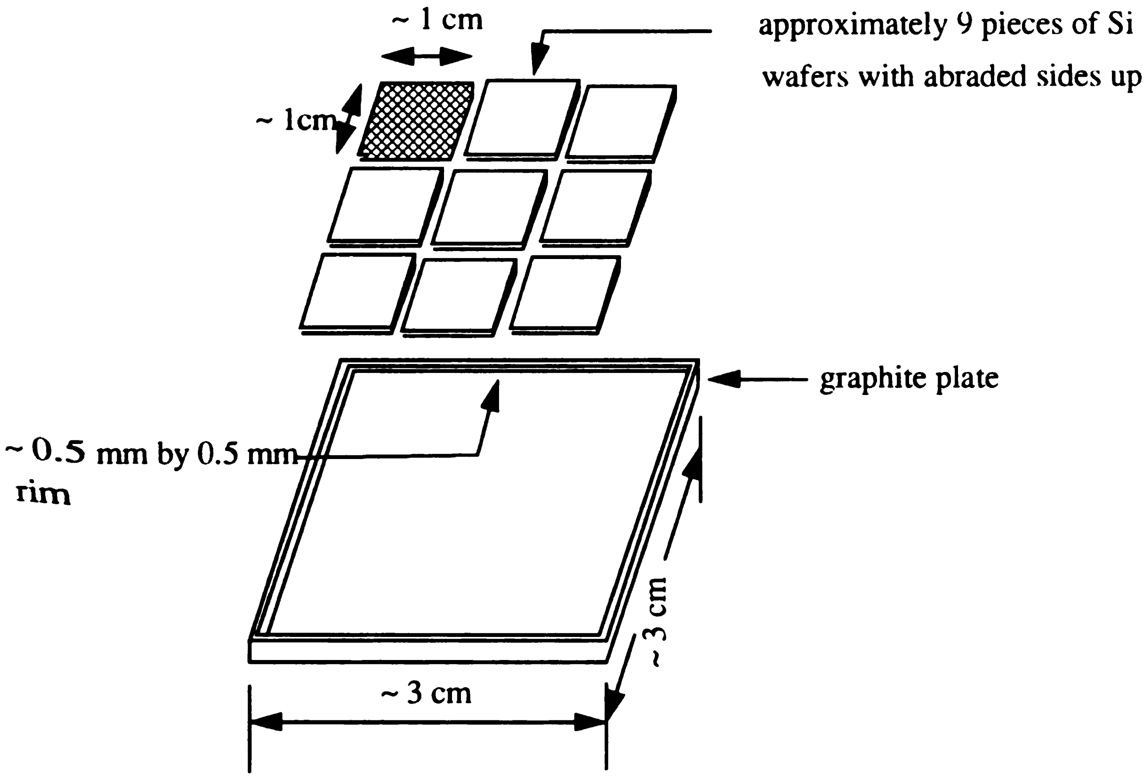

Figure 6. Approximately 9 pieces of abraded Si wafers are placed on the graphite plate. Each piece of Si wafer was approximately 1 cm by 1 cm

replaced over the rubber O-ring. The rubber O-ring formed an air tight seal between the dish's rim and the base plate which allowed the pumping-down of the inside cavity of the heavy dish. As mentioned earlier, pump-down was necessary for transducer calibration and to maintain deposition pressure.

2.2.2 Deposition of DTF's

The cavity within the dish was pumped down through a hole in the base plate beneath the fused silica tube (Figure 7). The pressure transducer was calibrated to zero at a pressure less than the resolution of the transducer. If the transducer was previously calibrated, the specimen chamber (cavity of the heavy dish) was pumped down to approximately 5 Torrs.

At this low pressure of ~5 Torrs, methane and hydrogen gases were allowed to flow into the specimen chamber at fixed rates. Methane was allowed to flow in at 1.5 and 2.25 standard cubic centimeter (sccm) and hydrogen at 300 sccm. These rates allowed for approximately 0.5 percent and 0.75 percent, respectively, methane in hydrogen as the precusor gas mixtures.

With ~5 Torr deposition chamber pressure and a constant inflow of the methane/ hydrogen precursor gas mixture, the microwave power was turned on and set to about 400 watts. A glowing plasma on the Si wafer specimens was immediately visible through a 4 cm diameter viewing port made of glass and wire gauze. Protective goggles were used to make these observations in order to avoid possible UV radiation to the eyes. The glow indicated that the plasma necessary for deposition was formed. If a glow was not observed the microwave power was reduced and another attempt made until a plasma was obtained

Once the glowing plasma was observed, the deposition chamber pressure was abo

guid

cylind

microw

chamb

water

duc

Figu

diam

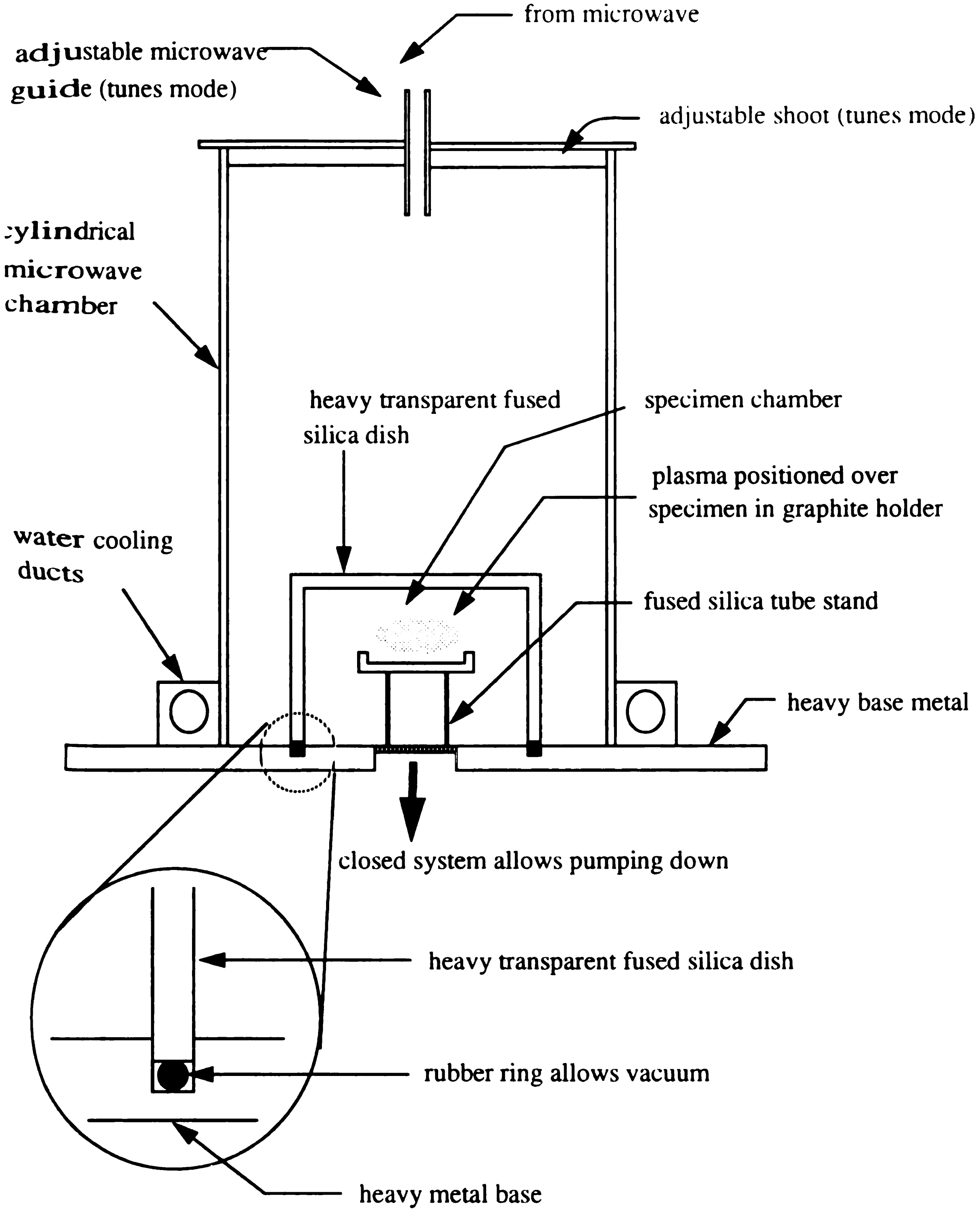

Figure 7. A schematic of the microwave reactor specimen chamber used to process the diamond thin film/silicon specimens used in this study.

increased to approximately 30 Torr. At 30 Torr the microwave power was increased to 600 watts. The deposition chamber pressure was then increased to 45 ± 5 Torr. At 45 ± 5 Torr deposition pressure the microwave power was turned to the desired wattage. Wattages of 700 and 900 watts were used in film depositions. At this point the system was left to run with constant monitoring of the deposition pressure. A leak valve for the methane and hydrogen gases from the deposition chamber was periodically adjusted to maintain the deposition pressure at 45 ± 5 Torr.

The microwave energy was directed from the top of the cylindrical microwave cavity downward into the cavity by a wave guide (Figure 7). Inside the cylindrical microwave cavity the microwave energy excited the CH_4-H_2 gas mixture in the fused silica dish into a plasma state (Figure 7). The nine pieces of Si wafers on the graphite plate were positioned by the silica tube to be in the plasma of a TM_{012} excitation mode.

The TM_{012} excitation mode in the cylindrical cavity had a minimum reflected power of approximately 3.8 percent. The TM_{012} excitation mode was tuned by an adjustable sliding short and an adjustable microwave guide. The tuned TM_{012} excitation mode located the plasma to coincide with the position of the graphite plate containing the pieces of Si wafers (Figure 7).

In the excited plasma, carbon atoms are in a supersaturated state. As the carbon atoms move from the high temperatures of the plasma to lower temperatures outside the plasma they readily crystallize onto any suitable surface. The Si wafers are positioned in this lower temperature region of supersaturated carbon atoms and their abraded or photoresist-treated surfaces are suitable for the crystallization of the supersaturated carbon atoms. Diamond is nucleated either in the abrasions, on imbedded seed diamonds, or on other suitable sites

[5,12]. A continuous 0.25 micron SiC layer forms around these nucleation sites before, during, or after nucleation, and the diamond crystals then grew from these sites upwards in columns [12], thus forming the polycrystalline DTF.

The temperature of the Si wafer surfaces were determined during deposition for DF-N4 and DF-N5. Four temperature readings were taken for set DF-N4 at approximately one hour intervals with a pyrometer (IRCON Ultimax infrared thermometer, serial number 11003, Niles, ILL. 60648). For set DF-N5, readings were taken form the four corner specimens and from the center specimen. The emissivity on the pyrometer was set at 0.65 for the temperature readings.

2.2.3 Deposition Conditions and Specimen Labeling

Five deposition runs were made under different conditions as listed in Table 1. Approximately nine specimens were deposited in each run. The first run was done at 0.5 percent methane in hydrogen and at 900 watts for 6 hours. This set was titled DF-N1 to indicate diamond film (DF), on n-type Si wafer (N), and first run (1). The second run was done at 0.5 percent methane in hydrogen at 900 watts for 8 hours. This set was titled DF-N2 in a similar manner, but (2) indicating the second run. The third run was done at 0.75 percent methane in hydrogen and at 900 watts for 6 hours and was entitled DF-N3 in a similar manner. The fourth run was done at 0.5 percent methane in hydrogen and at 700 watts for 6 hours and the was entitled DF-N4. The fifth set was deposited at 0.5 percent methane in hydrogen and 900 watts for 10 hours and was entitled DF-N5. A sixth set, deposited at 0.5 percent methane in hydrogen and 900 watts for 12 hours, was also attempted. However, deposition was terminated after 2 hours due to the detection of sufficiently strong

Table 1

NA-no

Table 1. Deposition conditions of sets DF-N1, DF-N2, DF-N3, DF-N4, and DF-N5.

Specimen Set	Percent C_4 in H_2	Deposition time (hr.)	Microwave power (W)	Substrate temperature (°C)
DF-N1	0.50	6	900	NA
DF-N2	0.50	8	900	NA
DF-N3	0.75	6	900	NA
DF-N4	0.50	6	700	766
DF-N5	0.50	10	900	774

NA -not available

microw

T

lows. D

ate fro

2.3 Op

Immedi

under a

differen

possibly

a good

to indic

good qu

Si

lyzes by

and gra

2.4 Di

To obta

were no

were et

ported a

microwave radiation leak.

The individual 1 cm by 1 cm specimens from the different runs were labeled as follows: DF-N1-1, DF-N1-2, DF-N1-3, etc. from set DF-N1, DF-N2-1, DF-N2-2, DF-N2-3, etc. from set DF-N2, and likewise for sets DF-N3, DF-N4, and DF-N5.

2.3 Optical Microscopy

Immediately after each deposition run a few of the specimens from that set were observed under an optical microscope to determine film quality. Optical microscopy may roughly differentiate between a well faceted diamond polycrystalline film and a poor faceted and possibly amorphous or graphitic film. A film covered with facets was assumed to indicate a good polycrystalline diamond film. A smooth film with a few or no facets was assumed to indicate that large regions of amorphous or graphitic carbon were present, thus not of a good quality diamond film.

Since optical microscopy is a qualitative technique, the films were subsequently analyzes by Raman spectroscopy, which yields more definitive information on the diamond and graphitic content of the film (Raman spectroscopy is discussed in section 2.6).

2.4 Diaphragm Preparation

To obtain circular diamond diaphragms from the ~1 cm square pieces of Si wafers which were now coated on one side with polycrystalline diamond thin films (DTF), circular holes were etched through the Si wafers. The etching resulted in circular DTF membranes supported along the edges by the Si wafers.

2.4.1 Protective Coating for Si Wafers

To etch a circular hole through the Si wafer, a circular area of the Si wafer was exposed to the etchant. All other surfaces of the Si wafer except the circular hole were protected from the etch. A protective coating was needed to protect the Si areas from the etch.

A thin sputtered gold coating (SEM sample preparation method, section 2.5.2) was inadequate protection from both a KOH and a NaOH etchant. The thickness of the gold coating sputtered onto the Si wafer was likely on the typical order of ten to one hundred angstroms, but the thickness was not ascertained. The gold coating on contacting the KOH and the NaOH etchants, both at 55 °C, immediately peeled away from the Si wafer surfaces. The KOH etchant was a 22:28 ratio by weight mixture of dry KOH pellets to deionized H_2O and the NaOH etchant was a 1:3 ratio by weight mixture of dry NaOH pellets to deionized H_2O.

Torr Seal epoxy, (Varian Vacuum Products, Lexington, MA.), was a successful protective coating against the KOH etchant. Torr Seal epoxy as a protective coating and KOH as the etchant was therefore used in all subsequent etchings.

To leave only a circular area of the Si wafer unprotected and exposed to the etch, small fused silica tubes with outer diameters of 2 mm, 3 mm, and 4 mm, and 2 to 5 mm in height were centered on the unprotected surfaces of the Si wafers. The silica tubes were then surrounded with the Torr Seal product (Figure 8 (a)).

The Torr Seal epoxy came in two tubes of different sizes. The larger tube contained the base resin and the smaller tube contained the hardener resin. Equal lengths of both the Torr Seal epoxy base and the hardener resins were squeezed from the tubes onto a sheet of notebook paper and thoroughly mixed together. Two pieces of wooden sticks

Figure
Seal
tected

Figure
water th

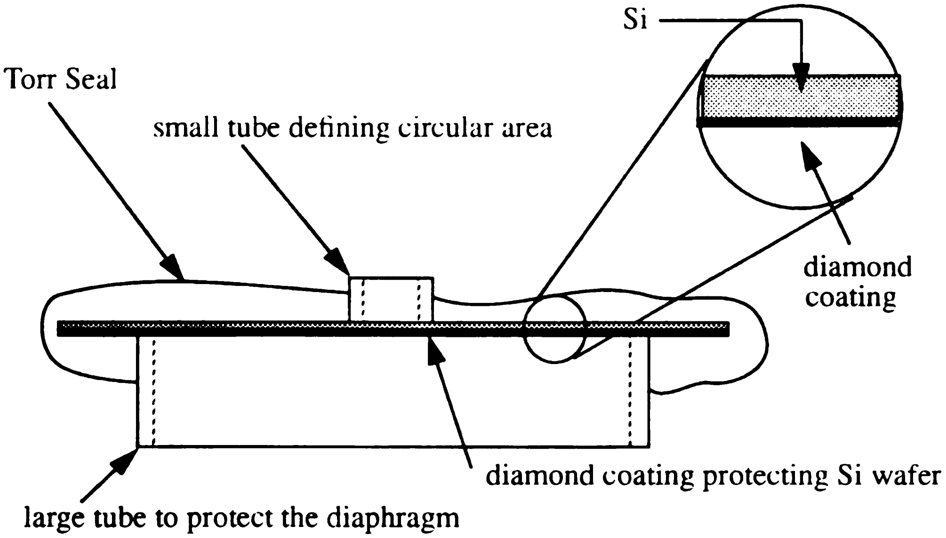

Figure 8 (a). Protective coating for the Si wafers. The Si wafer is protected by Torr Seal on top and edges and by the diamond coating on the bottom. The only area unprotected form the etch was through the circular tube.

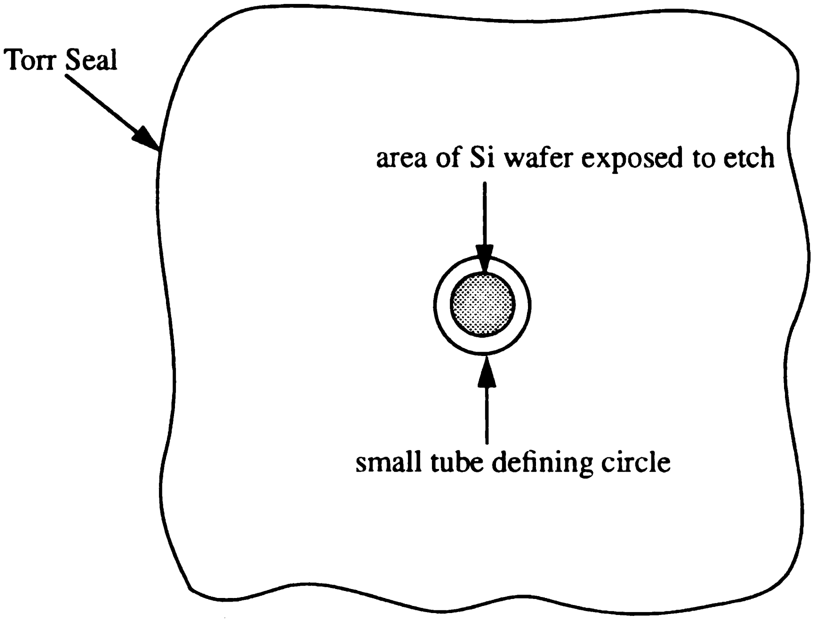

Figure 8 (b). Top view of the Torr Seal protected Si wafer showing the unprotected Si wafer that was exposed to the etch.

[illegible]

res

spe

S w

2.4.

Afte

the e

lim

[illegible]

reac

reac

wate

and

by a

to a

time

hours

Place

approximately 5cm long and 1mm in diameter was used to mix the base resin and hardener resin and to hold the tubes in position on the wafers while the Torr Seal was applied to the specimens. The mixed epoxy was then spread around the fused silica tubes centered on the Si wafers to cover the unprotected surfaces and the edges of the Si wafers.

The Torr Seal epoxy cured in 24 hour at room temperature and in 1.5 hours at 70 °C.

2.4.2 Etching of Si Wafers

After coating with the Torr Seal epoxy, the only Si surface area that remained exposed to the etch was the area inside of the small circular tubes (Figure 8 (b)). The etch was thereby limited to attacking only the exposed circular areas and so only circular holes were etched through the Si wafers.

Etching began on the exposed Si surface and proceeded through the wafers until it reached the DTF on the opposite side of the wafers. Etching was stopped when the etchant reached the DTF to avoid excessive lateral etching and even total etching away of the Si wafers.

The KOH etching solution was prepared with a mixture of 22 grams dry KOH pellets and 28 grams deionized H_2O. The bath was kept at 60 °C during the entire etching process by a Constant Temperature Circulator, Model 800 Fisher Scientific, which was connected to a 2,000 ml. jacketed beaker (Figure 9), Fisher Scientific, Pittsburgh, PA. The average time it took to etch a circular hole through the 0.5 mm thick wafer was approximately 24 hours.

The KOH was mixed in 100 ml glass beakers. The Torr Seal protected specimen was placed into the 100 ml beaker. The 100 ml beaker, with the specimen inside, was then

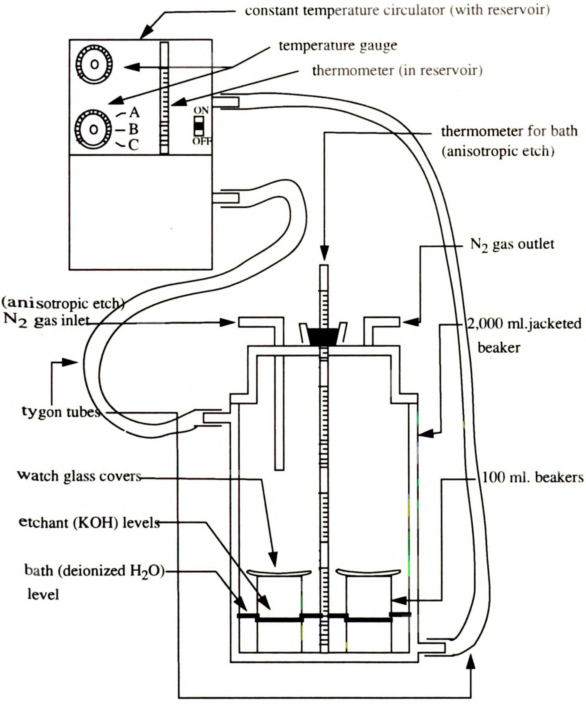

Figure 9. Etching Apparatus. Each specimen was placed into a 100 ml. beaker which had KOH etchant in it. The 100 ml beakers were then placed into the deionized water bath in the 2,000 ml. jacketed beaker. The KOH etch was kept at ~60° C.

[illegible]

[illegible]

[illegible]

[illegible]

[illegible]

[illegible]

2. [illegible]

[illegible]

[illegible]

[illegible]

[illegible]

[illegible]

[illegible]

[illegible]

[illegible]

[illegible]

[illegible]

[illegible]

[illegible]

[illegible]

placed into the 2,000 ml jacketed beaker. The water level in the 2,000 ml beaker was adjusted so that it was approximately the same as the level of the KOH solution in the 100 ml beakers. The walls of the 2,000 ml jacketed beaker was kept at 60 °C by water circulating through it, the water inside the 2000 ml beaker was kept at 60 °C by the water in the walls of the beaker and the KOH in the 100 ml beakers were kept at 60 °C by the 60 °C water surrounding it (Figure 9).

2.4.3 Anisotropic Etching of Si Wafers

In an attempt to produce a more circular DTF diaphragm, an anisotropic etch, 20 percent dry KOH pellets, 64 percent deionized H_2O, and 16 percent isopropanol alcohol (IPA), by weight, was tried. The anisotropic etch preferentially attacks the (100) surface planes of the single crystal Si wafers [22], and so was expected to produce holes with sides perpendicular to the surface of the wafers as it proceeded through the wafers. The circular shape of the area initially exposed to the etch would thus be maintained as the etch proceeded down through the wafers in the <100> direction.

Nine specimens were etched with the anisotropic etch. Two of the these nine specimens were etched under a nitrogen atmosphere. The nitrogen atmosphere was used in successful anisotropic etching done elsewhere [22], but its exact role was not understood. The gases produced by the chemical process were not known to be toxic, and any other purpose for the nitrogen atmosphere, besides that of a diluting solvent gases, was ambiguous.

The apparatus used in the anisotropic etching (Figure 10) consisted of a high pressure cylindrical tank with an Airco regulator, a 2,000 ml jacketed beaker and its lid, an escape valve, and a 500 ml beaker 3/4 filled with oil. Tygon tubing was used to conduct the N_2 gas

A

cylin

tanc

stanl

Figur
used t

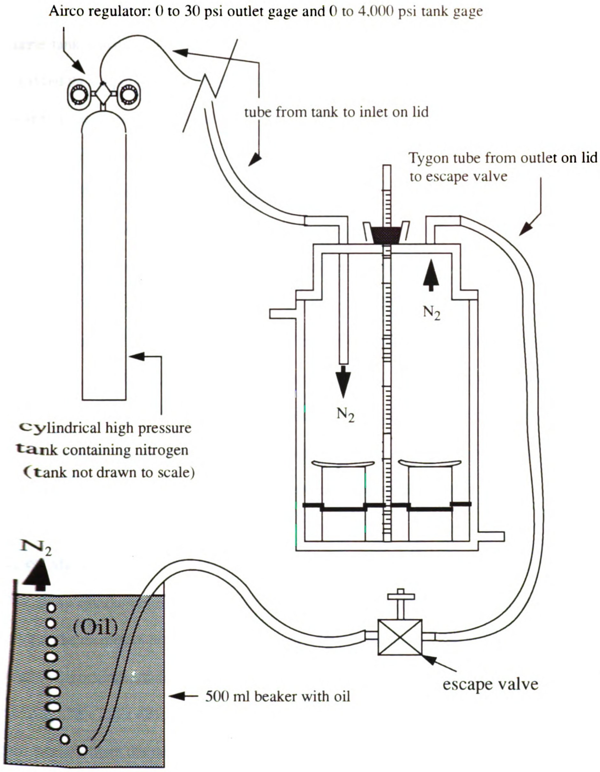

Figure 10. Anisotropic Etching Apparatus. The same method as regular etching was used but the etching occurred in an N_2 atmosphere.

2.5

and

the

through the etching apparatus. The Airco regulator, screwed onto the top of the high pressure tank, consisted of a tank gage, a output gage, and a manually operated valve that controlled the output pressure. Tygon tubes connected the outlet of the regulator to the inlet port on the lid of the 2,000 ml jacketed beaker, the outlet port of the beaker lid to a flow valve, and the flow valve to the 500 ml beaker oil.

With the beaker lid tightly sealed onto the beaker, the pressure regulator on the cylindrical pressure vessel was opened to approximately 2 psi. The valve between the 2000 ml beaker lid and the 500 ml beaker of oil was opened slightly to allow bubbles to escape through the oil at the end of the tube. Observing the N_2 gas escaping through the oil allowed manipulation of the escape rate of the gas.The bubbles escaping were adjusted to a rate at which single bubbles, and not a continuous stream of gas, was coming out of the end of the Tygon tube in the oil. The flow of nitrogen bubbles seen escaping through the oil confirmed that a nitrogen atmosphere existed in the beaker and also assured that no air was allowed back into the chamber where the anisotropic etching was occurring.

2.5 Measuring DTF's Diameters

Etching circular holes through the Si wafers produced circular DTF diaphragms (Figure 11). The diameters of these DTF diaphragms were determined from micrographs of x7.5 and x10 magnifications. Diameters were determined by multiplying the actual measurement of the inner diameter of the protective tube by a ratio of the diaphragm diameter over the tube's inner diameter. The ratio of the diaphragm diameter over the tube's inner diameter was taken from photomicrographs of the specimens such as Figure 11.

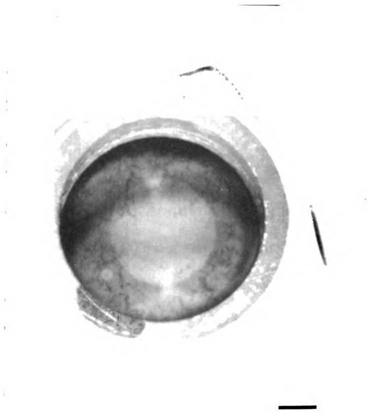

Figure 11. Photomicrograph of the diamond diaphragm of specimen WF#60-6. The diaphragm is the lite gray circular area in the middle. The bar represents 1.3 mm.

2.6 Raman Spectroscopy

Raman spectroscopy combined with optical microscopy was sufficient to verify that a given specimen was a high quality DTF [8]. A 488 nm (blue) laser light with a 2 microns spot size, was used on a 1,200 groove grading for the Raman spectroscopy.

2.7 Diaphragm Bursting

2.7.1 Pressure Vessel and Data Acquisition Apparatus

The apparatus used to burst test the DTF diaphragms (Figure 12) consisted of a generic cylindrical high pressure tank containing nitrogen gas, a built-to-order cylindrical pressure vessel, an MKS type 122AA-05000BB-SPCAL transducer, and an MKS model PDR-D-1 power supply/readout (MKS Instruments Inc. Andover MA.). The high pressure tank was similar to that used in the anisotropic etching. It had an open/close valve on top. On this valve were two pressure gages and a manual pressure regulator. The first gage registered the tank's internal pressure and the second gage registered the regulator's outlet pressure. A manually regulator controlled the output pressure. The 122A pressure transducer had an operating pressure range of 0 to 100 psia with an output of 0 to 10 volts of direct current, accurate to ± 0.5 percent of the reading. The necessary input signal was ± 15 volts of direct current at 35 milliampere. The operating temperature range of the 122A pressure transducer was 0 to 50 °C. The transducer was connected to the pressure vessel by a standard cajon 8VCR fitting. The PDR-D-1 power supply/readout was accurate to ± 0.01 percent of its display and had a resolution of 1 millivolt. The power supply/readout had a conversion rate of 2.5/sec. and a power supply output of ± 15 volts at 35 milli-amp and a maximum operating temperature of 50 °C.

I

cylind
tank c
tank m

Figure 12.

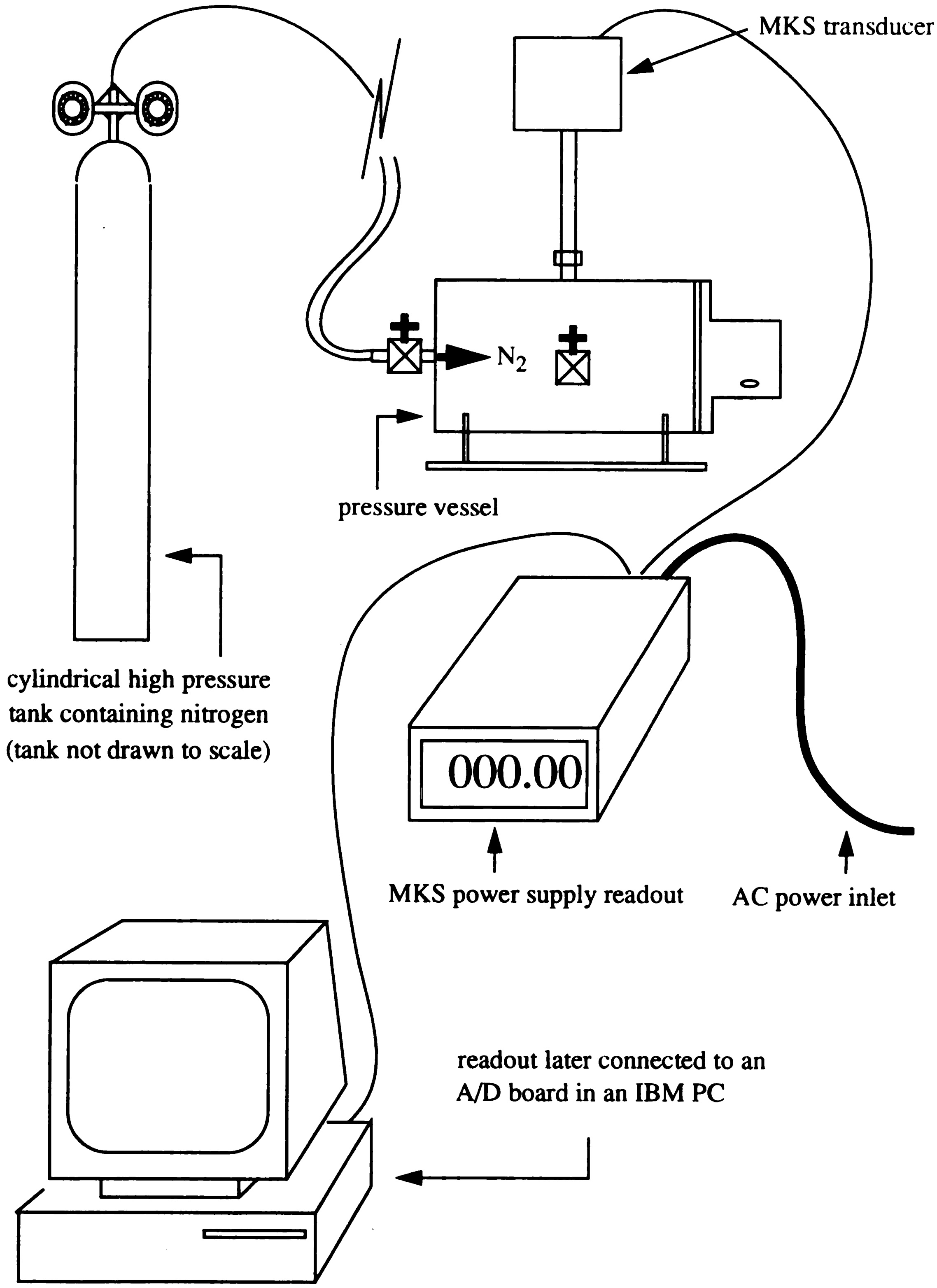

Figure 12. Burst Testing Apparatus

Figu
stud

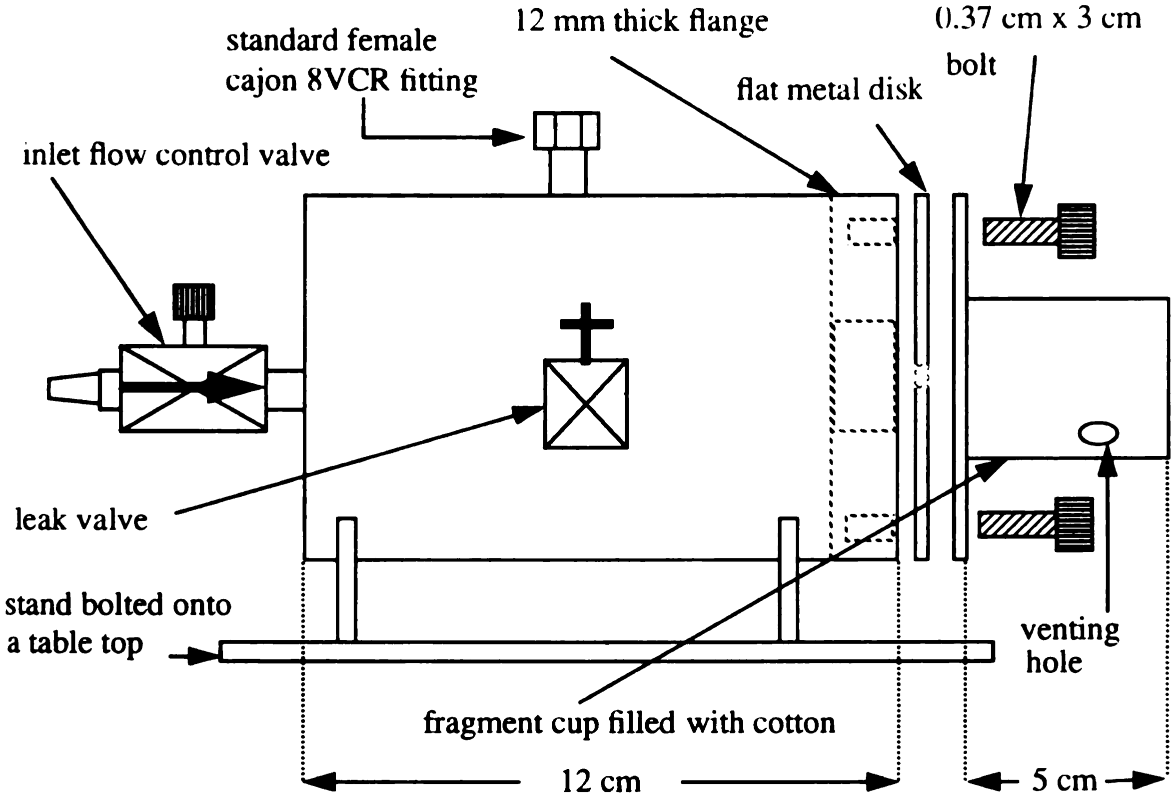

Figure 13 (a). Side view of pressure vessel used to burst the DTF diaphragms used in this study. The pressure vessel was bolted horizontally onto a table top.

Figur

Figu
three

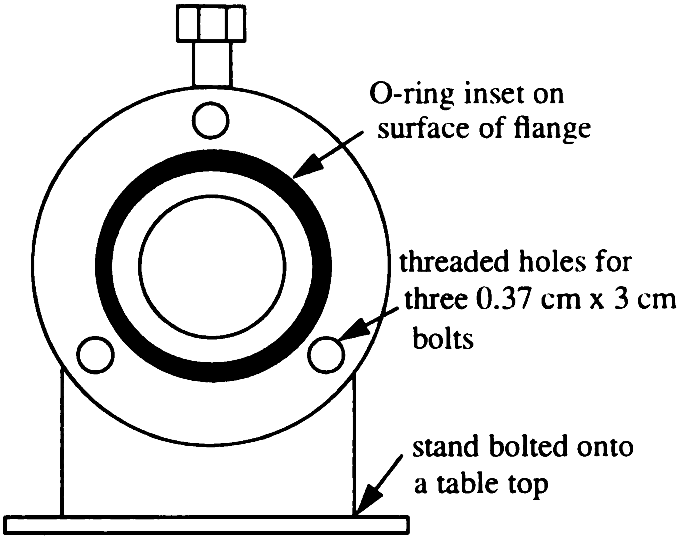

Figure 13 (b). Front view of pressure vessel showing the inset rubber O-ring.

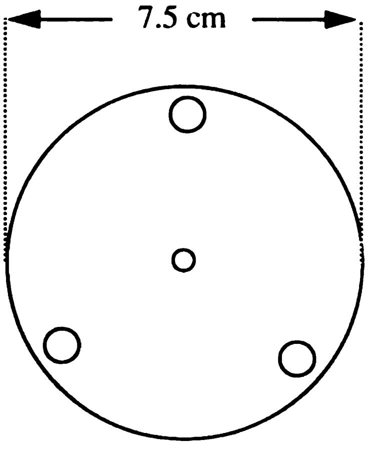

Figure 13 (c). Front view of flat metal disk showing the 2.5 mm hole in the center and the three holes for the bolts.

The pressure vessel (Figure 13) was a cylinder 12 cm long by 7.5 cm in diameter. At one end was the pressure inlet flow control valve (model F02, ARO Inc.). The maximum capacity of the inlet flow control valve was 200 psi. At the other end of the cylinder was a 12 mm thick 7.5 cm diameter flange. The flange had a 4.5 cm diameter 3.5 mm thick rubber O-ring inset on its outer surface (Figure 13 (b)) so that an air tight seal could be obtained between the flange and the flat metal disk bolted down onto the flange. A flat metal disk held the specimens being tested. Three bolts, ~ 0.37 cm diameter by 3 cm long, were used to fasten the flat metal disk against the flange. The flange was 12 mm thick so that the three holes threaded into the flange for the bolts would not go through the flange. A thick flange was used in an effort to form a better seal. Any hole through the flange would be a potential source of a leak. The flat metal specimen disk, which was fastened over the O-ring, had a 2.5 mm hole bored through its center (Figure 13 (c)) over which the specimen was glued.

The specimen was glued with its larger (5 to 6 mm) protective tube attached to the metal disk (Figure 14). The glue used was a plastic model cement called Testers (The Tester Corporation, Rockford IL.). The glue was squeezed onto the flat cross-sectional end of the large protective tube in an amount just sufficient to wet and form an air-tight seal between the flat cross-sectional end of the larger tube and the flat metal disk. The glue was then allowed at least three hours of curing before burst testing.

Connected to the outside of the flat metal disk was a fragment cup, 3.8 cm diameter by 6.4 cm long, which was filled with cotton and placed behind (relative to the bursting direction) the flat metal disk (Figure 13). The cotton caught the fragments of the DTF films as the film burst. The cotton was about 8 mm from the DTF diaphragm when the burst chamber was assembled. The fragment cup was attached to the flange by the same three

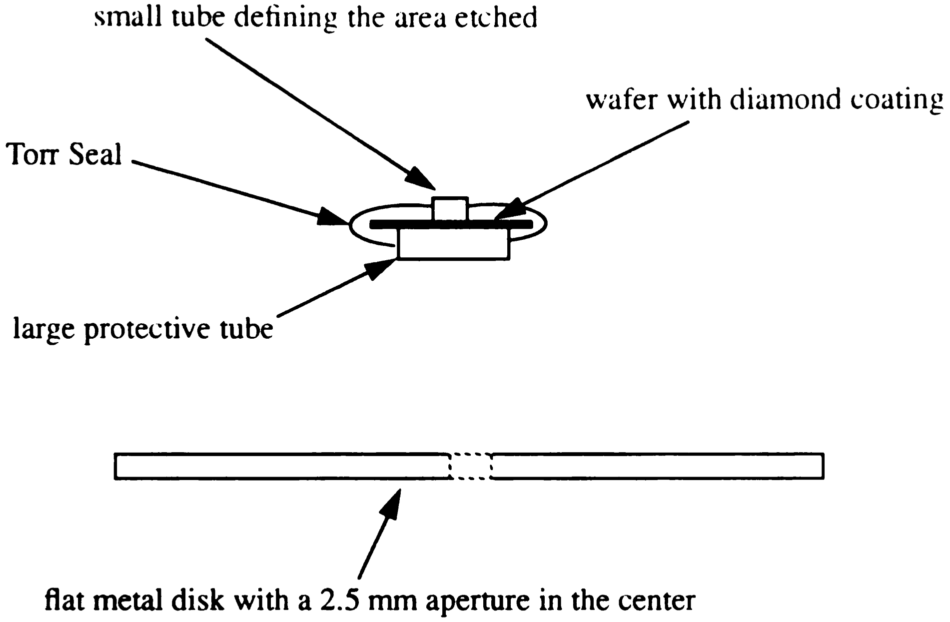

Figure 14 (a). Diamond thin film diaphragm specimen and flat metal disk.

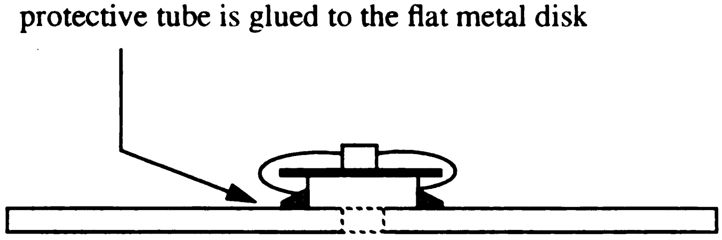

Figure 14 (b). The specimen is glued onto the flat metal disk. The metal disk, with the specimen glued in place, is then ready to be mounted into the pressure chamber for burst testing.

hus

can

stan

are

are

LED

inst

the

mea

the

of a

pre

2.7

The

som

and

pre

pre

be

bu

bolts that held the flat metal disk onto the flange. The fragment cup was aligned concentrically along the cylindrical pressure vessel's axis of symmetry. A hole drilled into the side of the fragment cup allowed instantaneous venting of nitrogen gas when the DTF burst.

On one side of the pressure vessel was a leak valve which allowed the internal pressure to be reduced from a high chamber pressure to ambient pressure if necessary. The pressure transducer, mounted on top of the pressure vessel, was connected to a power supplying LED readout that was visually monitored during testing.

A Computer Board Inc. model CIO-AD08-PGL A/D data acquisition board was later installed in an IBM PC-8086 for more accurate data collection (Figure 12). The signal from the 122A pressure transducer was channeled into the CIO-AD08-PGL A/D data acquisition board. The acquisition board had a resolution of 0.024 psi. The software installed [23] in the PC, see appendix D, sampled the pressure transducer output approximately ever tenth of a second. After five samplings, the highest values was written to a data file. The highest pressure value attained in the pressure vessel was thus recorded in the data file.

2.7.1.1 Leak Testing the Pressure Vessel

The pressure vessel was tested for air leaks. An air tight chamber was desirable for two reasons. First, so that nitrogen gas was not unreasonably spent during each burst test, and second, and more importantly, to obtain more accurate chamber pressure readings. If the pressure vessel had any substantial leaks, pressure fluctuation would cause incremental pressure increases to be impossible. Small incremental pressure increases were desirable because the LED readout was visually monitored during burst testing, and a more accurate burst pressure could be determined if the pressure on the readout was increased in small increments. After the automatic data acquisition was operational, small pressure leaks did not interfered with the accuracy of the data collected.

To obtain an air-tight pressure vessel, as many joints as possible were welded (Figure 13). A threaded male joint for the inlet flow control valve was welded to the center of a circular metal plate and the plate then welded to one end of a cylindrical vessel. Teflon tape was used on the threaded male joints to seal the flow control and leak valves. The threaded male joint for a leak valve was also welded on the side of the cylinder. At the other end of the cylindrical vessel the 12 mm thick flange was also welded into place.

A rubber O-ring inset on the outside of the flange would form an air-tight seal with the flat metal disk as the flat metal disk was fastened down onto the flange. A standard female cajon 8VRC fitting for the transducer was also welded onto the top of the pressure vessel. With the male cajon 8VRC fitting of the transducer fastened in place, this joint too was air-tight.

To test the pressure chamber, the 2.5 mm aperture (figure 14 (a)) in the flat metal disk was covered with scotch tape. The disk was then fastened down onto the rubber O-ring on the flange for an air-tight seal. The leak valve was closed, and the transducer mounted into its 8VCR cajon fitting. Approximately 5 psi of nitrogen gas from the high pressure tank was then allowed into the pressure vessel and the inlet flow control valve closed. The tygon tube to the flow control valve and the electrical wire to the transducer were quickly disconnected and the pressure vessel then submerged in a sink of tap water. The pressure vessel was totally submerged in water to cover everything but the attached transducer. If bubbles came from any joint, the joint was unfastened and re-taped with a thicker layer of teflon tape in order to improve the seal. This procedure was repeated until leaks were minimal.

2.7.2 Diaphragm Bursting Procedure

The burst pressure determined for each specimen was a differential pressure, therefore the ambient pressure was recorded before each test. The flat metal disk with the DTF diaphragm specimen glued onto it was bolted onto the flange. The fragment cup was bolted behind the small hole on the flat metal disk through which the fragments of the film would emerge upon bursting (Figure 13(a)). The three 0.37 cm diameter by 3 cm long bolts were fastened tightly into the flange to insure a good seal between the flat metal disk and the rubber O-ring. The leak valve on the side of the pressure vessel was closed and the N_2 gas inlet flow control valve was opened.

The open/close valve on the high pressure tank was opened and the tank gage immediately showed the pressure inside the tank. The regulator valve was then opened until the regulator gage read approximately 5 psi. The flow control valve was opened slowly while the pressure readout was monitored. The manually operated regulator valve was not sufficiently sensitive to allow the pressure in the pressure chamber to be increased incrementally, thus, the chamber pressure was increased slowly and continuously. The rate of pressure increase in the pressure vessel was monitored and kept at approximately 0.1 psi per second. This rate was visually approximated and set only in an attempt to minimize the human error in recording the burst pressure from the digital readout. If the pressure in the pressure vessel rose too rapidly the digits on the readout would be changing too rapidly to visually detect the maximum value displayed at burst. On the other hand, the pressure in the pressure vessel could be raised too slow for practicality. In adjusting the pressure increase rate in the pressure vessel, if the rate of pressure increase in the burst chamber was too fast the N_2 inlet flow control valve would be closed slightly to lower the rate. If the rate

was too slow the flow control valve would be opened to increase the rate.

Once the pressure-increase rate was set, the pressure was increased at a constant rate while visually monitoring the LED readout until the DTF diaphragm burst. The DTF diaphragm would always be the weakest place in the chamber walls and therefore the first to fail under the increasing pressure. The DTF diaphragm failed with an audible pop and an immediate drop in vessel pressure to ambient pressure. The maximum pressure that was seen on the LED readout was then recorded as the failure pressure of the DTF diaphragm.

After the automated data acquisition system was installed, the testing procedures were the same except that the LED readout was not monitored for the maximum pressure. The maximum pressure attained in the vessel was immediately displayed on the PC monitor after each test. A data file of pressure versus time was also created for each test.

2.7.2.1 Obtaining the Burst Pressures

At the start of each test, the ambient pressure was recorded. The failure pressure, the maximum pressure attained in the pressure vessel, was determined at the end of the test. The burst pressures for each specimen was calculated by subtracting the ambient pressure from their failure pressure.

2.8 SEM's Preparation and Testing Procedures

Once the diamond diaphragms were burst and the burst pressures recorded, the fragments of the burst diamond diaphragms were inspected in the SEM to determine their grain sizes, film thicknesses, and to study the morphology of the diaphragms. Three different SEM's were used in this investigation, a JEOL JSM-35CF, a Hitachi S-415A, and a Hitachi

S-2500C.

To prepare the diamond film fragments for SEM testing, it was necessary to retrieve the film fragments from the cotton-ball fibers (Figure 13 (a)), mount the fragments onto the SEM stubs, and then gold coat the mounted fragments to make them electron conductive thus suitable for SEM use.

2.8.1 Retrieving and Mounting of the DTF Fragments

The cotton balls with the entangled fragments were removed from the fragment cup (Figure 13) after each burst. The fragments of the DTF diaphragms were retrieved (untangled) from the cotton ball fibers with the use of a toothpick.

The fragments from each burst test were untangled over a SEM stub which had a sticky tab (catalog # AT, M.E. Taylor Engineering, Inc.) on its top surface (Figure 15 (a)). Sticky tabs are a standard SEM specimen mounting device. The fragments fell onto the sticky tabs and stuck in random positions and locations (Figure 15 (b)). They were left in the positions and locations in which they fell because they were too small to handle, and positioning them to simplify thickness measurements would be impossible.

A large number of fragments from each burst test was dropped onto a stub in order to increase the probability of getting one or more fragments to stick at an angle of 30 to 90 degrees with the surface of the stub. This angle of 30 to 90 degrees between the flat fragments and the surface of the stub would allow easier thickness measurements of the edges of the film fragments to be made.

Each specimen stub was given the label of the DTF fragments mounted on it to avoid confusion during SEM testing.

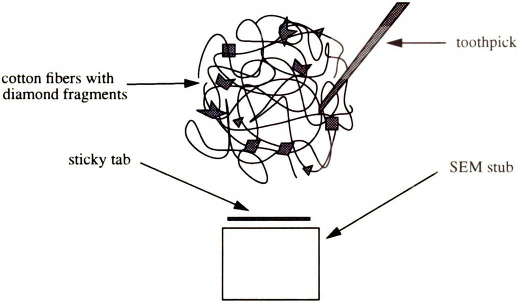

Figure 15 (a). Fragment mounting on SEM stubs. The DTF fragments were entangled in cotton fiber after the burst test. The fragments were retrieved by using a toothpick to pull the cotton fibers apart.

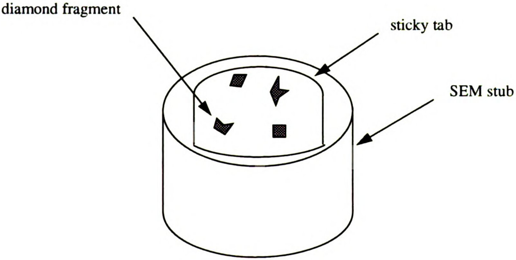

Figure 15 (b). The fragments fell onto the sticky tab on the SEM stub and remained in the random positions and locations in which they fell.

The specimen stubs used were all made of aluminum. The stubs for the JEOL JSM-35CF were 0.5 cm height and 0.9 cm in diameter. The stubs for the Hitachi S-415A were 1 cm high and 1.5 cm in diameter. The same stubs of the Hitachi S-415A were also used in the Hitachi S-2500C. Although not the proper stub for the Hitachi S-2500C, the S-415A stubs were adhered onto the actual S-2500C stub with a double sided carbon tape (Figure 16). The actual S-2500C stub was 0.75 cm high and 3.5 cm in diameter.

2.8.2 Coating the Mounted Fragments

The DTF fragments mounted on the SEM stubs were then gold coated using an Emscope Sputter Coater model SC500M (Ashford, KT.) The sputtering rate was 7 nm per minute and sputtering was done for approximately 3 minutes. A gold coating of approximately 21 nm thick (7 nm per minute by 3 minutes) was thus sputtered over the entire fragment and SEM stub. The gold coating was necessary to make the specimens conductive to avoid charging during testing. Charging causes excessive brightness and distortion in the SEM image. After gold coating the specimens were then ready for SEM observation.

2.8.3 Specimen Insertion into the SEM's

Specimen insertion and exchange procedures were quite similar for the newer JEOL JSM-35CF and Hitachi S-2500C SEM's. However, the specimen insertion and exchange procedures for the Hitachi S-415A SEM was quite different than those of the other two SEM's. The main difference was due to the fact that the specimen chamber for the Hitachi S-415A had to be pumped-down from ambient pressure after each specimen insertion, but for the JEOL JSM-35CF and Hitachi S-2500C only a small insertion (waiting) chamber had to be

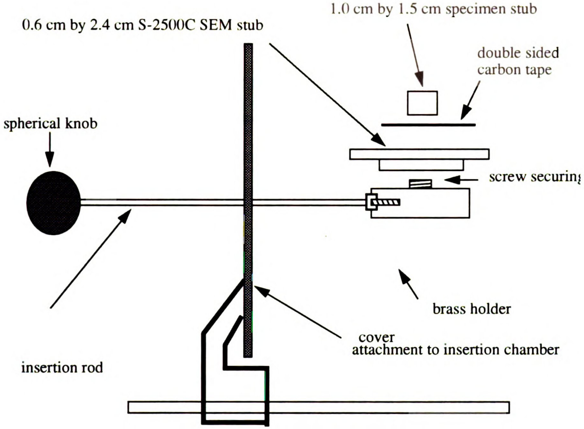

Figure 16. Hitachi S-2500C SEM specimen holder. The specimen holder assembly is attached to the insertion chamber by the temporary cover. The 1.0 cm by 1.5 cm specimen stub was adhered to the S-2500C SEM stub with a carbon tape. The S-2500C SEM stub was screwed securely onto the brass holder which is inserted into the specimen chamber by the spherical knob and insertion rod and remained there during testing.

pumped-down, which required less time. This made the JEOL JSM-35CF and Hitachi S-2500C SEM's more convenient to use, because exchanging specimen was less time consuming.

However, exchanging specimens on the Hitachi S-2500C SEM was not as quick as on the JEOL JSM-35CF. On the Hitachi S-2500C SEM, the accelerating voltage was discharged before each specimen removal and recharged after each specimen insertion. This procedure of discharging and recharging of the LaB_6 gun with the accelerating voltage took approximately 20 minutes and was done as a safety precaution to protect the costly LaB_6 gun from possible burn-out during specimen exchange. On the JEOL JSM-35CF this procedure of discharging and recharging was not performed, making the JEOL JSM-35CF the most time efficient of the three SEM's.

Before turning on any of the SEM's, the water pressure for the cooling pumps were checked to make sure an adequate pressure was in the lines. The chamber pressures of the JEOL JSM-35CF and the Hitachi S-2500C were also checked to verify operating chamber pressure. The specimen chamber pressure for the JEOL JSM-35CF and the Hitachi S-2500C SEM's were usually maintained at operating pressure, $\sim 10^{-6}$ psi. The specimen chamber pressure for the Hitachi S-415A SEM however, was not maintained at operational pressure between use and pumping-down the chamber was necessary before each insertion.

2.8.3.1 Hitachi S-415A

Once the water-coolant pressure was checked to be in an operational state, the S-415A power switch was turned on. The mounted and gold coated film fragments on the 1.0 cm high by 1.5 cm diameter aluminum stub was then secured onto the specimen holder (Figure 17). The specimen chamber was vented and the cover of the entrance port pulled out to reveal a stage onto which the specimen holder was place. The stage, built onto the inside of the door, was designed to hold the specimen holder snugly and allowed x, y, and z motions, rotation, and tilting of the specimen (the terms x, y, and z signifies three dimensional Carteian coordinates). The specimen on the holder was placed securely on the stage and the entrance cover to the port was replaced. The specimen chamber was then pumped-down to operational pressure and the SEM was ready for testing.

2.8.3.2 JEOL JSM-35CF

Once the water coolant pressure and the specimen chamber pressure were checked to be in operational state, the JSM-35CF power switch was turned on. The mounted and gold coated film fragments on the 0.5 cm high by 0.9 cm diameter aluminum stub was placed onto the specimen holder (Figure 18). The height of the stub was adjusted with the height adjustment screw (Figure 18) to make it flush with the top of the brass holder. The stub was then secured in place with the securing screw (Figure 18). The temporary cover was moved toward the brass stage until it clipped into place. The clip kept the stage from moving inwards during pump-down of the insertion chamber.

A red vent/vac button on top of the entrance to the small insertion chamber (Figure 19) was pressed which immediately vented the insertion chamber to ambient pressure. The

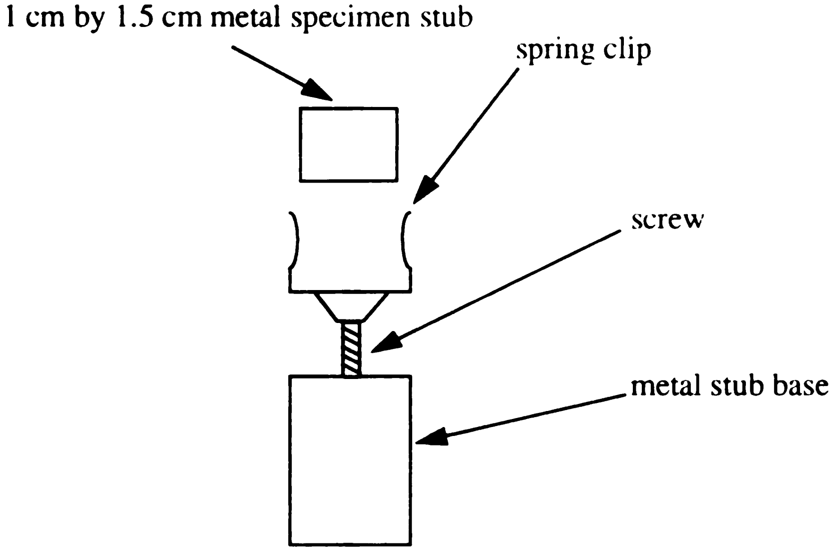

Figure 17. The Hitachi S-415A SEM specimen holder consisted of a metal stub base, and a spring clip which held the 1 cm by 1.5 cm specimen stub in place. The spring clip is height adjustable and screws into or out of the metal stub base to adjust the specimen into focusing range.

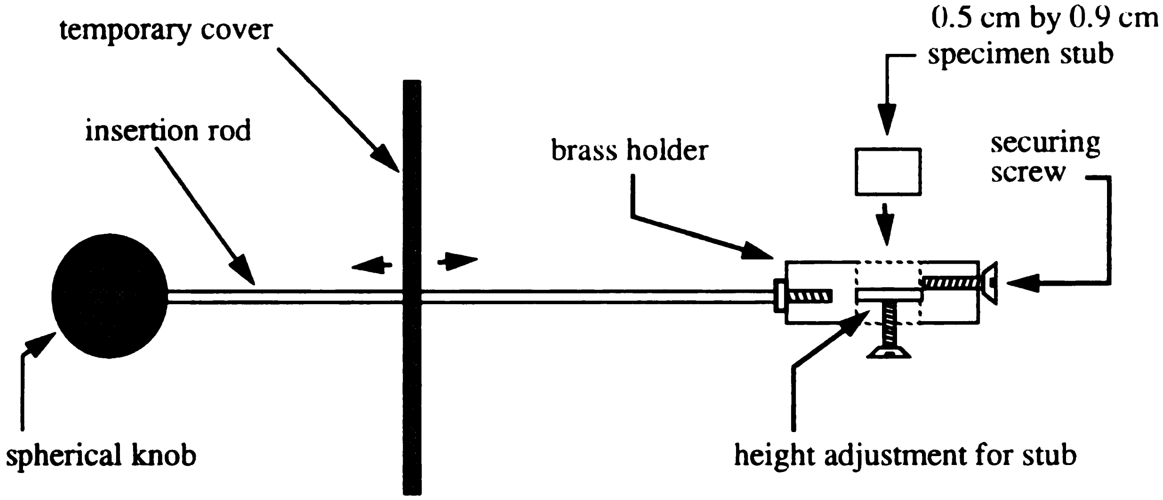

Figure 18. JEOL JSM-35CF SEM specimen holder assembly. The spherical knob was used to screw the steel rod into the brass stage. The knob was also used to move the brass stage between the insertion chamber and the specimen chamber. The temporary cover would replace the true cover only while the specimens were being loaded

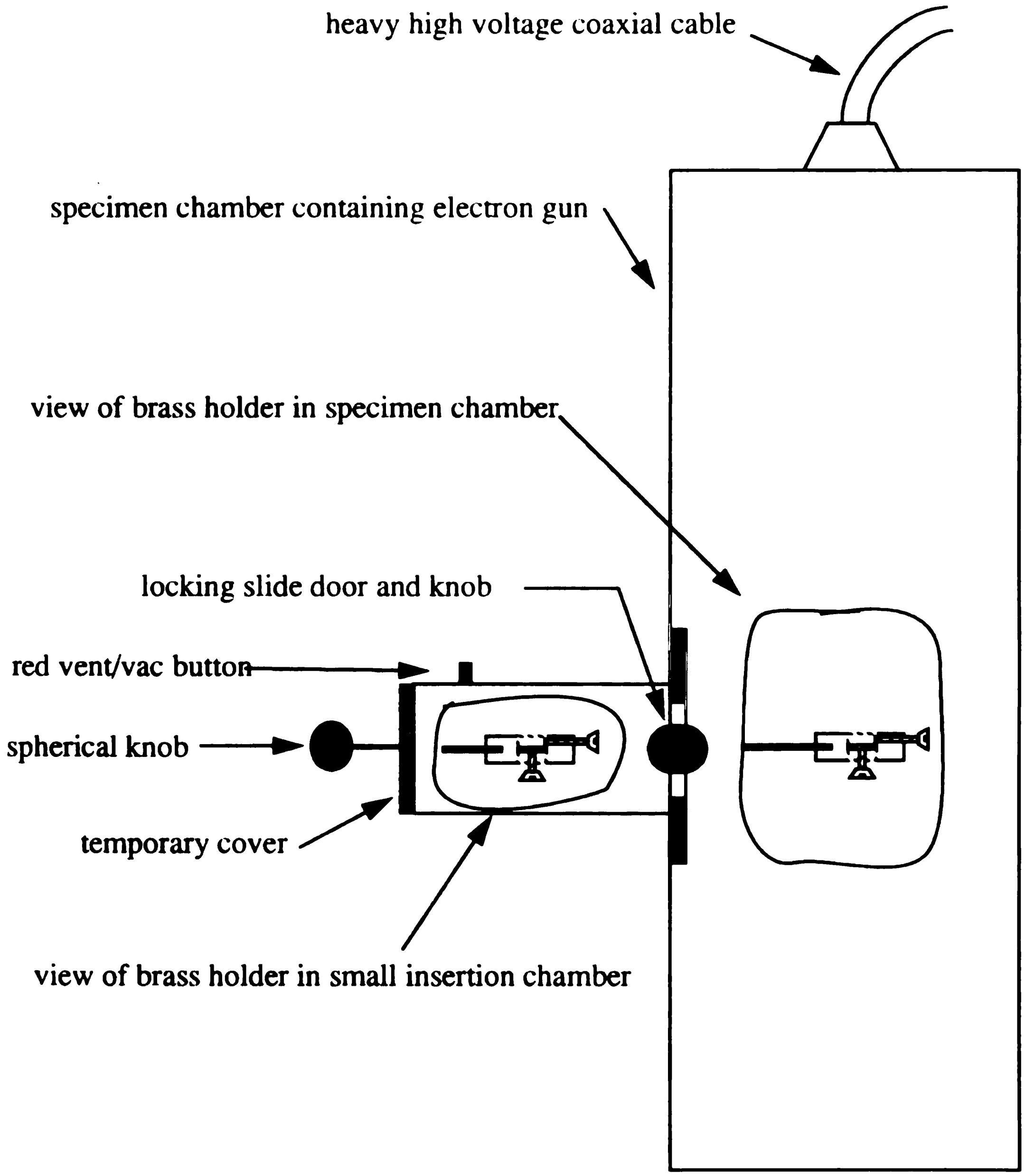

Figure 19. JEOL JSM-35CF specimen chamber and insertion chamber.

metal cover on the port of the insertion chamber was removed from the entrance once the chamber was vented. The metal cover of the entrance was similar in size and shape to the temporary cover (Figure 18) built onto the specimen holder assembly. The stage with the specimen was placed in the insertion chamber. The temporary cover on the specimen holder assembly covered the entrance port. The red button on top of the insertion chamber was pressed again which pumped-down the insertion chamber. When the pressure in the insertion chamber became equal to that in the specimen chamber, the locking slide door separating the two chambers (Figure 19) was opened by pulling out the slide door knob. The brass holder containing the specimen was then moved from the insertion chamber into the specimen chamber with the insertion rod (Figure 19). The rod was unscrewed from the brass stage and retracted leaving only the stage with the specimen in the specimen chamber. The locking slide door was returned to lock position and the specimen was ready to be tested.

2.8.3.3 Hitachi S-2500C

The water coolant pressure and specimen chamber pressure were checked to be in operational state, before the S-2500C SEM was switched on. At the push of a similar vent/vac button, the insertion chamber was aired and its cover was pulled away from the entrance to reveal the brass holder (Figure 16). The specimen holder assembly on the S-2500C was built onto the insertion chamber cover. A 1 cm high by 1.5 cm diameter aluminum stub with the mounted and gold coated film fragments on the it was then secured onto the S-2500C stub with a double sided carbon tape (Figure 16).The S-2500C stub was screwed securely onto the brass specimen holder. The double sided carbon tape which held the two stubs together was used for several consecutive specimen stubs.

Once the specimen stub was secured on the S-2500C stage, the stage was pulled back until a clip held it in position near the cover. The entire door assembly was then slid back in place over the port of the insertion chamber. The vent/vac button was depressed again. which pumped down the insertion chamber.

Within 15 seconds the insertion chamber containing the specimen was at a pressure equivalent to that in the specimen chamber, approximately 10^{-6} psi. A locking slide door separating the insertion chamber and the specimen chamber (similar to Figure 19) was then opened and the specimen pushed from the insertion chamber into position in the specimen chamber. The rod was then unscrewed from the brass stage using the spherical knob and retracted from the specimen chamber. The locking slide door between the two chambers was then locked. The S-2500C was then ready for testing.

2.8.4 SEM Procedures for Testing Specimens

Procedures for grain size, film morphology, and film thickness determination were quite similar for the three different SEM's once the specimen was in the specimen chamber and ready for testing. Once in the specimen chamber, each SEM was capable of maneuvering the specimen in order to take grain size, film morphology, and film thickness micrographs. The only differences were the positioning of the controls and the resolution capability on each SEM. The Hitachi S-2500C was generally thought to have greater resolution than the JEOL JSM-35CF, and the JEOL JSM-35CF was thought to have a better resolution than the Hitachi S-415A. The resolution of the micrographs taken by the Hitachi S-415A were visibly lower than the resolution of those taken by the JEOL JSM-35CF and the Hitachi S-2500C. However, the resolution of the micrographs taken by the JEOL JSM-35CF showed revisio

.9 Gra

nce th

and y

mong

nd als

N

nents

he sp

differ

fragm

sub

grain

tion.

An a

M6

This

side

of f

she

imen

no obvious difference to those taken by the Hitachi S-2500C.

2.9 Grain Size

Once the specimen was in the specimen chamber, the specimen was maneuvered using the x and y controls to locate an appropriate fragment of which a grain size and/or film morphology micrograph was taken. An appropriate fragment was one with its faceted side up and also lying flat on the specimen stub.

Not all the fragments on the specimen stub showed their faceted side up. Some fragments had their substrate (interfacial) side up. Nor were all the fragments lying flat against the specimen stubs. Some were at an angle to the stub, the same position in which they had fallen onto the sticky tabs (section 2.7.1 Retrieving and Mounting of DTF Fragments). A fragment showing its faceted side and also lying flat against the surface of the specimen stub, or only at a small angle with the stub's surface, would give the best micrograph for grain size and film morphology because it would minimize foreshortening in each direction.

An appropriately positioned fragment was located by scanning the specimen stub at low, ~ x60, magnification to find a fragment that appeared to be lying flat on the specimen stub. This fragment was then observed at a higher, ~ x1800, magnification to see if its faceted side was up and if the fragment was truly lying flat on the specimen stub. If both conditions of faceted side up and flatness to the specimen stub was not met, another fragment was checked until a fragment satisfying both conditions was found.

If a fragment chosen for grain size micrograph was not flat to the surface of the specimen stub, the fragment was adjusted before the micrograph was taken. The angle between the fragment and the stub's surface was determined by finding a 90 degrees edge on the fragment and tilting the fragment until that edge just disappeared. At this position it was assumed that the fragment was showing a flat surface to the direction of observation and the grain size micrograph was taken.

2.9.1 The Average Line Intercept Method

The average line intercept (ALI) method required a x8,000 to x12,000 magnification SEM micrograph of the faceted surface of the DTF so that at least 10 grains spanned the shorter side of the rectangular photomicrograph. Grain sizes were on the order of a micron.

Points were marked along the perimeter of the micrograph and labeled. A straight edge was placed across the micrograph from one labeled point to another. The number of grain (diamond facet) boundaries intercepted by the straight edge were counted. The straight edges was then moved to another pair of labeled points and the grain boundary intercepts were counted again. This was done as many times as was necessary to get a total sum of at least 250 intercepts. The lengths of the line segments, whose intercepts added up to ~ 250, were also summed. The ALI value was then determined by dividing the sum of the lengths by the sum of the intercepts, ~ 250. The quotient was then divided by the magnification of the photomicrograph and reported in microns. The ALI value was then multiplied by a correction factor of 1 which gave a value characterizing the grain size of the polycrystalline diamond film. The correction factor could have a value of 1.0 to 1.5.

2.10 Film Thickness

Maneuvering the specimen for a film thickness micrograph was a more involved procedure than maneuvering for a grain size micrograph. It was necessary to get a micrograph of the edge of the film that showed the true thickness of the edge. Ideally, a fragment positioned with its edge normal to the direction of observation was desired in order to get a true length (or thickness). If maneuvering the specimen to such a position was too difficult, the true length could often be determined by using a tilt correction feature common to most SEM's.To get the true thickness of the fragment's edge, the fragment was usually positioned with its edge at a known angle to the direction of observation. An angle of 30 or 45 degrees from the direction of observation was most often used. The tilt correction was then set to correct for the 30 or 45 degrees tilt before a film thickness micrograph was taken (Figure 20). In this manner the true thickness of the film fragments were imaged. The SEM micrographs also had bar scale on them which allowed accurate determination of the film thickness.

The thickness of a CVD diamond film may also be approximated by measuring the weight gained by the Si wafer during deposition. The weight gained is divided by the mass density of the polycrystalline diamond thin film (DTF) which gives a volume. This volume is then divided by the area which is covered by the DTF which gives the film thickness; assuming a film of uniform thickness. This method of determining the film thickness however, was not done.

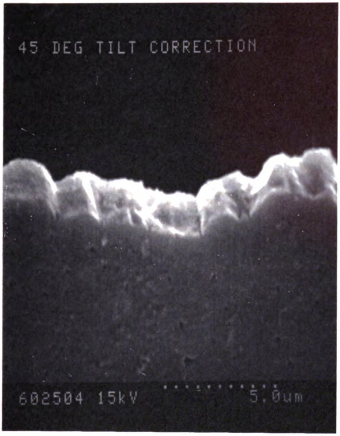

Figure 20. SEM micrograph of specimen WF#60-25 showing the thickness of a fractured polycrystalline diamond diaphragm. The dotted bar represents 5 microns.

2.11 Additional Specimens Obtained for Testing

Two additional (100) single crystal Si wafers with diamond thin films (DTF's) chemically deposited on them were later obtained for testing. These two specimens were deposited by the same microwave system as the earlier specimens, however, the microwave system was modified with a larger deposition chamber which allowed the deposition of larger DTF's. The two large specimens obtained were received as approximately 4.85 cm radius semicircles. These two semicircular specimens with DTF's on them were received with the labels WF#25 and WF#60. These labels were included in the labels given to each individual specimens taken from these wafers (section 2.11.3).

2.11.1 Photoresist Pre-deposition Treatment

The diamond coated semicircular wafers WF#25 and WF#60 were treated by a photoresist method prior to deposition [6]. The photoresist method involved centrifugally covering a wafer with a suspension of fine diamond powder in photoresist. During deposition the photoresist was baked off leaving only the diamond powder on the wafer. These diamond particles acted as nucleation sites for the DTF that was grown on the wafers.

2.11.2 Deposition Conditions

Specimen WF#25 was deposited at a microwave power of 2,098 watts, a deposition pressure of 40 Torr, and precursor gas flows of 400 sccm H_2, 4 sccm CO_2, and 4 sccm CH_4. The surface temperature of the wafer during deposition was 850 °C. The weight gain was 7.26 milligram per hour per milligram Si wafer for a deposition time of 8 hours. The Si wafers had a uniform thickness of approximately 0.53 mm.

Specimen WF#60 was deposited at a microwave power of 2,861 watts, a deposition pressure of 35 Torr, and precusor gas flows of 400 sccm H_2, 2 sccm CO_2, and 6 sccm CH_4. The surface temperature of the wafer during deposition was 776 °C. The weight gain was 9.42 milligram per hour per milligram Si wafer for a depositing of 8.5 hours. The Si wafer a uniform thickness of approximately 0.53 mm.

2.11.3 Specimen Labeling

The large semicircular wafers with DTF's on them were fractured into final specimen size, approximately 1 cm squares, as mention earlier (section 2.1.3). The individual 1 cm square specimens from each large semicircular piece were labeled as follows: from specimen WF#25, WF#25-1, WF#25-2, WF#25-3, etc. and from specimen WF#60, WF#60-1, WF#60-2, WF#60-3, etc. This was similar to the labeling of the specimens initially tested and mentioned earlier (section 2.2.3).

During the fracturing of WF#60 the relative positions of each specimen taken from that wafer was recorded (Figure 21). After all the WF#60 specimens were burst tested and their thicknesses determined on the SEM, the film thicknesses were compared to their relative position to examine if any thickness-position relationship existed.

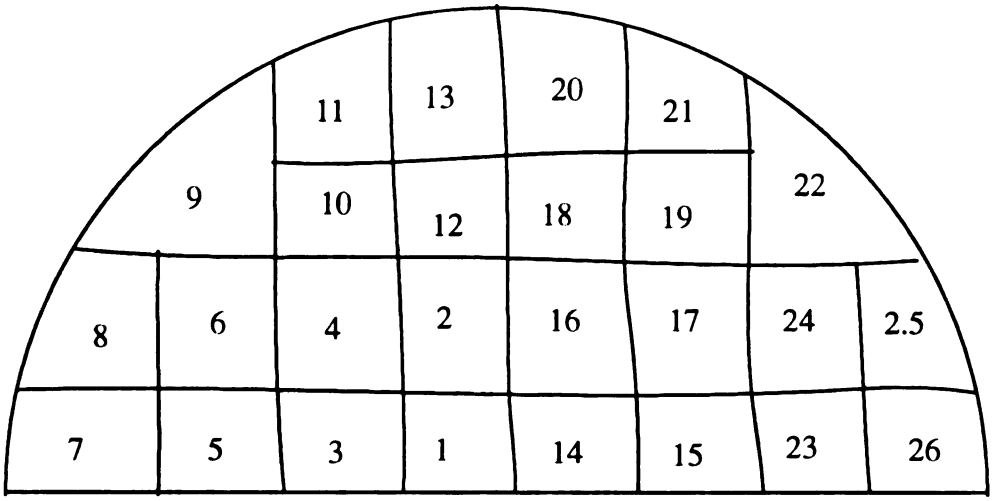

Figure 21. The relative positions for the 26 specimens taken from wafer WF#60 were recorded for later film thickness versus relative position correlation.

3. Results and Discussion

3.1 Results in Wafer Preparation

3.1.1 Results of Abrading

The method of abrading the Si wafers by hand (section 2.1.1) had a low reproducibility. The amount of diamond powder used, the load applied, the direction of the abrading motion, the frequency of the motion and time duration of the motion, were all variables that were either not monitored precisely, or not monitored at all. The average time of abrading was approximately 10 minutes, but without knowing the applied force and frequency of the abrading motion, this information would not be very useful in reproduction of the procedure.

3.1.2 Photoresist Treatment

The pre-deposition photoresist treatment to increase nucleation sites, developed by Aslam *et al* [6], seemed an acceptable method for creating nucleation sites. The WF#25 and WF#60 specimens were prepared by the photoresist pre-treatment. The DTF's and were sufficiently adhered to the Si wafer to allow fracturing, dimpling, and etching without the DTF flaking away from the Si wafer.

A clear difference however was noted between the DTF's deposited on photoresist treated Si wafers, WF#25 and WF#60, and those deposited on abraded Si wafers, DF-N1, DF-N2, DF-N4, and DF-N5. (Recall the DF-N3 specimens were assumed not to be of a high diamond content see section 3.2 and were not tested.) Most of the SEM micrographs taken of the bottom of the WF#25 and WF#60 DTF's showed distinct grains (Figure 22 (a) and (b)). No such patterns were noted on any of the other DTFs' bottoms. The DTF

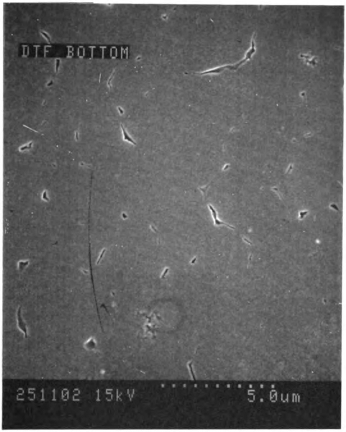

Figure 22 (a). Micrograph of the interfacial surface of the DTF specimen WF#25-11 showing distinct grain boundaries define by the dark lines. A grain size of 0.71 micron was determined from this micrograph. The dotted bar represents 5 microns.

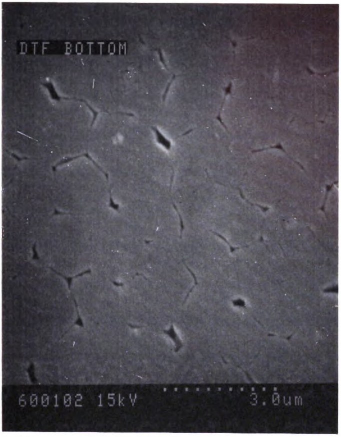

Figure 22 (b). Micrograph of the interfacial surface of DTF specimen WF#60-1 showing distinct grain boundaries define by the dark lines. A grain size of 1.00 micron was determined from this micrograph. The dotted bar represents 3 microns.

3.2 Film Deposition

Five sets of specimens were deposited: DF-N1, DF-N2, DF-N3, DF-N4, and DF-N5 (Table 1). Each set had at least nine specimens. Sets DF-N1, DF-N2, and DF-N5 varied only in deposition times of 6, 8, and 10 hours respectively. Sets DF-N1and DF-N4 varied only in their microwave deposition power of 900 and 700 watts respectively. Every set except DF-N3 was deposited at 0.5 percent methane in hydrogen. Set DF-N3 was deposited at 0.75 percent methane in hydrogen.

Set DF-N3 was believed to be amorphous as determined by optical microscopy. The thicknesses of fragments from this set were also much larger than those from the other sets which would also support the claim of the DF-N3 films being mostly amorphous. The higher concentration of methane used in the deposition precusor gas for set DF-N3 was attributed to this effect.

Concentration up to 1 percent methane in hydrogen, is typically considered the optimal concentration range for diamond deposition. However, at 0.75 percent methane in hydrogen, set DF-N3 was considered to be mostly graphitic or amorphous carbon.

The average temperature determined for set DF-N4 was 766 ± 5 °C and for set DF-N5 the average deposition temperature was 774 ± 15 °C.

3.3 Results in Diaphragm Preparation

3.3.1 Result of Etching

The polycrystalline diamond thin film did not always protect the Si wafer that it covered from the KOH etch. The DTF deposited onto the single crystal Si wafers was expected to protect the Si wafer from the strong chemical etch because of diamond's high chemical inertness [3,5]. However, some of the DTF flaked off from the Si wafers (Figure 23) after several hours of exposure to the KOH etch. Gas bubbles produced on the surfaces of the DTF's during etching indicated that etching occurred on or through those DTF surfaces. The strong KOH etch was believed to be responsible for the flaking away of the DTF's from their Si substrates because gas bubbles were evolving from the surfaces of the DTF's.

To avoid destroying the DTF's with the etchant, the DTF's were protected from the etchant with the cover slips of microscope slides. The glass cover slip was placed over the large protective tube on each specimen and then Torr Seal was used to seal the glass cover slip in place (Figure 24).

After the cover slip alteration to protect the DTF's, flaking of the DTF's from their Si substrates was no longer observed. This result indicated that the strong KOH etch was affecting the DTF's by somehow getting through the thin film and attacking the Si substrate beneath.

Two possible reasons for the adverse reaction of the DTF's to the KOH etch seems likely. One reason is that pinholes may have existed through the films, allowing the etch to attack the Si substrates beneath. Secondly, the DTF's may not have been of a high diamond quality (high percent diamond phase), but rather diamond films with an appreciable amount of graphitic and/or amorphous carbon, allowing the KOH to etch through and attack the Si

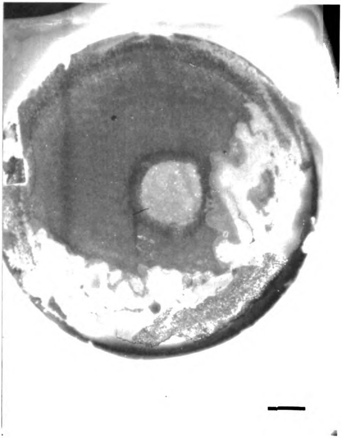

Figure 23. The flaking off of the DTF from the Si substrate is obvious on specimen WF#25-12. The etch seem to have penetrated the diamond film and attach the etch beneath. The circular diamond diaphragm is also observed in the center. The bar represents 1 mm.

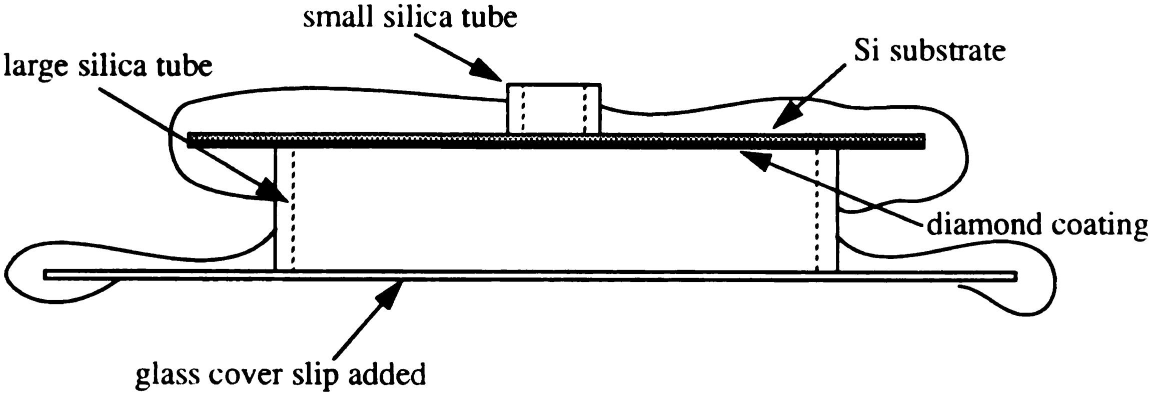

Figure 24. Cover slip modification. A glass cover slip was added to protect the diamond coating from the KOH etch. The inner diameters of the large and the small tubes were 6.8 mm and 2,3, or 4 mm, respectively.

beneath. The Raman spectroscopy results showed that there was an appreciable amount of graphitic carbon in the diamond films (Figure 27 (a) and (b)), supporting the second possibility.However, carbon is reportedly resistant to KOH (from 5 to 90 weight percent) etchant up to 160 °C [32]. This would rule out the second possibility suggested, leaving pinholes as the only suspect.

The second possibility, the effect of pinholes, may better explain the unexpected adverse effect of the KOH etch on the DTF films. It is possible that the pinholes penetrating through the films allowed the KOH etch through to attack the Si wafer beneath. Pinholes penetrating through the films would more likely be found in films whose thickness ranged with the size of the constitutive grains of the polycrystalline film. The thicknesses of the films that were etched ranged from approximately 2 to 5 microns with grain sizes ranging from approximately 0.4 to 1.1 microns. However, pinholes were not specifically searched for, and none were observed during an SEM examination.

3.3.1.1 Anisotropic Etching

The attempts made at anisotropic etching were unsuccessful since the holes resulting from the anisotropic etch were less circular than those from the isotropic etch. Usually two parallel sides resulted instead of the circular shape desired and expected. For the anisotropic etching done elsewhere [22], the shape desired was rectangular. The area initially exposed to the KOH etch was therefore also rectangular [22], as opposed to the circular shape used in this experiment. The anisotropic etch therefore seemed more suitable for producing rectangular holes than circular ones.

Perhaps as the etch proceeds through the wafer, a rectangular shape can easily be maintained since the (010) and (001) principal planes are preferentially un-attacked. In contrast, an initially circular shape defines no such edges. The preferential etching may explain the unexpected pattern of two parallel sides noticed with the anisotropic etch. The anisotropic etch was thus aborted.

The isotropic etch, which produced diaphragms of greater circularity, was used in all subsequent etching. Circularity of the diamond diaphragm was essential to the simplicity of the theoretical calculations for the biaxial strength (as determined in the diaphragm bursting experiment).

3.3.2 Result of Dimpling

Diaphragms prepared by dimpling partway through the Si wafers before etching (Figure 25) showed greater circularity than diaphragms produced by etching circular areas of the Si wafer defined by small tubes. Dimpling to define the area to be etched is a method of producing diaphragms that was developed by Bill Glime [24]. The greater circularity that the dimpling procedure produced led to the decision to produce all remaining diaphragms by the dimpling method.

Although the dimpling method produced diaphragms of higher circularity, it had the disadvantage that the Si wafer tapered down at the diaphragm edge [24]. The diamond diaphragm may be thought of as a clamped circular membrane assuming no bending moment at the boundary, but the thin edges means that likely (it was not measured), the edge does rotate, indicating a non-zero moment. Restated, the assumed boundary conditions of no lateral displacement at the diaphragm's boundary is no longer satisfied if the supporting Si is so thin that it deflects during the loading of the diamond diaphragm. The assumed boundary

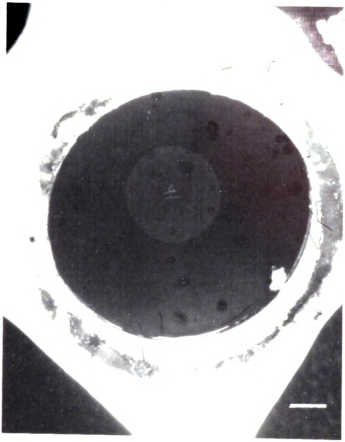

Figure 25.Typical diamond diaphragm (WF#60-15) produced by etching a concave and circular dimple that was grounded into the Si wafer with a TEM sample preparation dimpler. A1 mm bar is indicated.

conditions of the diaphragm would also be violated if the Si was so thin at the boundary that, instead of only the diamond diaphragm breaking, failure also occurred through the thin Si wafer.

3.4 Data Collected

The data acquired for each specimen included diaphragm diameter, burst pressure, grain size, and film thickness. Additional data such as Raman spectroscopy and some SEM micrographs of DTF interfacial surfaces, film morphology, and cracks in the DTF's were also taken for some of the films. The numerical data collected are tabulated in Table 2 for DF-N1, DF-N2, DF-N4, and DF-N5, Table 3 for WF#25, and Table 4 for WF#60. A maximum error of 10 percent may be present in the SEM measurements as no calibration was done to the SEM prior to testing.

3.4.1 Burst Pressures

The burst pressures for each diaphragm was determined as mentioned earlier (section 2.7.2.1).The burst pressure for the DF-N1 diaphragms were 7,172 Pa and 135,586 Pa. The burst pressure for the DF-N2 diaphragms varied from 60,552 to 265,655 Pa, for DF-N4 diaphragms from 14,276 to 252,138 Pa, and for DF-N5 diaphragms from 84,000 to 254,759. The burst pressure varied from 23,793to 370,758 Pa for the WF#25 diaphragms, and from 10,103 to 390,620 Pa for the WF#60 diaphragms.

Table 2. Burst pressures, diameters, thicknesses, and grains sizes for DF-N1, DF-N2, DF-N3, DF-N4, and DF-N5 specimens. Set DF-N3 was not included in analysis.

Specimen	Burst Pressure (Pa)	Diaphragm Diameter (mm)	Thickness (micron)	Grain Size (micron)
DF-N1-5	7,170	5.6	2.3	1.1
DF-N1-6	136,000	5.0	2.0	0.9
DF-N2-2	144,000	5.2	2.7	0.5
DF-N2-3	60,600	6.8	1.9	0.6
DF-N2-4	267,000	3.4	2.8	0.6
DF-N2-5 ⊕	255,000	5.1	3.1	0.6
DF-N2-7 ⊕	173,000	4.5	2.1	0.9
DF-N3-2	102,000	6.8	3.5	N.A.
DF-N3-5	171,000	6.2	6.4	N.A.
DF-N4-2	173,000	4.7	3.0	0.7
DF-N4-3	14,300	4.8	2.0	0.3
DF-N4-4	94,600	5.6	2.8	0.6
DF-N4-5	252,000	3.6	3.3	0.6
DF-N4-8 ⊕	128,000	6.8	2.5	0.5
DF-N5-2	191,000	3.6	4.5	0.9
DF-N5-3	144,000	6.8	3.7	0.8
DF-N5-4	100,000	6.5	4.3	1.0
DF-N5-5	84,000	6.8	4.7	0.4
DF-N5-6	140,000	6.5	5.3	0.6
DF-N5-8 ⊕	255,000	6.8	3.2	0.9

N.A. - either not available or not applicable.
⊕ - Data points removed from this set for best fit of entire data set.

Table 3. Burst pressures, diameters, thicknesses, and grain sizes of WF#25 specimens.

Specimen	Burst Pressure (Pa)	Diaphragm Diameter (mm)	Thickness (micron)	Grain Size (micron)	Grain Size of DTF bottom (micron)
WF#25-7 ⊕	126,000	2.4	5.0	0.8	NA
WF#25-8	150,000	3.4	2.5	0.8	NA
WF#25-9	155,000	2.1	2.3	0.6	NA
WF#24-10 ⊕	23,800	2.5	2.5	1.0	NA
WF#25-11	98,100	5.2	3.0	0.7	0.71
WF#25-14	92,600	2.6	2.2	0.6	0.86
WF#25-15	371,000	1.9	2.4	0.5	NA

⊕ - Data points removed from this set for best fit of entire data set.
NA - not available.

Table 4. Burst pressures, diameters, thicknesses, and grain sizes of the WF#60 specimens.

Specimen	Burst Pressure (Pa)	Diaphragm Diameter (mm)	Thickness (micron)	Grain Size (micron)	Grain Size of DTF bottom (micron)
WF#60-1	342,800	2.3	4.4	1.3	1.0
WF#60-2	94,300	4.6	3.2	1.1	NA
WF#60-3	86,900	4.6	2.5	1.1	1.0
WF#60-4	366,400	1.4	2.8	1.3	NA
WF#60-5 ⊗	77,450	4.2	3.5	1.2	NA
WF#60-6	83,520	4.7	3.6	1.0	1.0
WF#60-7 ⊕	87,240	3.8	2.2	0.5	0.8
WF#60-8 ⊗	258,300	2.4	2.5	1.1	1.0
WF#60-9	56,550	3.5	2.5	1.1	NA
WF#60-11	151,800	3.3	2.5	1.0	NA
WF#60-12	252,900	3.1	3.5	1.3	NA
WF#60-14	135,500	5.3	3.2	0.9	NA
WF#60-15	191,200	3.1	3.3	1.3	0.8
WF#60-16	132,300	4.2	3.3	1.3	1.0
WF#60-17	116,200	4.3	3.0	1.3	1.0
WF#60-18 ⊗	390,600	2.5	3.4	1.2	NA
WF#60-19	163,000	3.6	3.3	1.3	NA
WF#60-21 ⊗	72,760	3.9	3.0	0.9	NA
WF#60-23	152,500	3.4	2.5	1.3	NA
WF#60-25	119,200	3.0	2.0	1.0	1.3
WF#60-26	10,100	6.5	2.6	1.0	NA

⊗ - Data point removed for best fit WF#60 data set.
⊕ - Data points removed from this set for best fit of entire data set.
NA - not available.

3.4.2 Grain Size

The grain size of each film was measured by the average line intercept method (section. 2.8.4.1.1) from SEM photomicrographs. SEM photomicrographs of the deposition (faceted) surface were used to determine grain size for the DTF specimens. On DF-N1, DF-N2, DF-N4, and DF-N5 the interfacial surfaces, as photographed by the SEM, showed no granular structure, therefore no grain size determination were done of the interfacial surfaces for these specimens. However, some WF#25 and WF#60 films showed distinct granular structure on their interfacial surfaces. Many specimens from WF#25 and WF#60 were therefore also tested for the grain size of their interfacial surfaces.

The grain sizes for the DF-N1 DTF were 0.871 micron and 1.124 micron. The grain sizes for the DF-N2 DTF varied from 0.529 to 0.860 micron, for DF-N4 from 0.327 to 0.719 micron, and for DF-N5 from 0.423 to 1.02 micron. The grain size varied from 0.472 to 0.990 micron for WF#25, and from 0.54 to 1.26 micron for WF#60.

The grain boundaries were seen only on some of the films prepared by the photoresist pre-deposition treatment. Films WF#25 and WF#60 were prepared by using the photoresist treatment which may be the reason for their interfacial difference with the films from DF-N1, DF-N2, DF-N4, and DF-N5 prepared by abrading with the 1 micron diamond powder.

3.4.3 Film Thickness

Film thickness measurements for each DTF was taken from SEM micrographs (section 2.8.4). The film thicknesses determined for the two DF-N1 specimens were 2.0 microns and 2.3 microns. The film thicknesses determined for the DF-N2 specimens varied from 1.9 to 3.1 microns, for DF-N4 the thicknesses varied from 2.0 to 3.3 microns, and for DF-N5 film thicknesses varied from 3.2 to 5.3 microns. The film thicknesses for WF#25 varied from 2.2 to 5.0 microns, and for WF#60 from 2.0 to 4.4 microns as determined from SEM micrographs. (Additional results on thickness versus relative position for WF#60 specimens is given in section 3.7.1.1.).

3.4.4 Film Morphology

The grain size and film thickness micrographs also gave information on the DTF's morphologies. Also while scanning and checking the many DTF fragments on each SEM stub to find good views for grain size and film thickness micrographs, several interesting aspects of the different DTF's morphologies were observed and captured on micrographs.

The (111), (110), and (100) faces dominated the deposition surfaces as is common to CVD processes [17]. The (111) faces appeared as pyramids while the grains showing the (110) and (100) faces generally appeared as squares on the film surfaces. Twinning, mostly observed on the (111) facets, appear as an additional layer on one or more of the (111) pyramidal faces (Figure 26).

The pyramidal (111) facets dominated the deposition surfaces of the DF-N1, DF-N2, DF-N4, DF-N5, and the WF#25 specimens, while the (110) and/or (100) square facets dominated the deposition surface of the WF#60 specimens. This observation is verified by comparing the grain size photomicrographs in appendices A and B to those in appendix C. These difference observed between deposition surfaces could not be linked to the different deposition temperature ranges employed for each DTF (section 3.7.3).

Although most of the grain size micrographs showed good (111), (110), and (100) diamond faceting on the DTF's top surfaces, a few of the surfaces showed facets with small

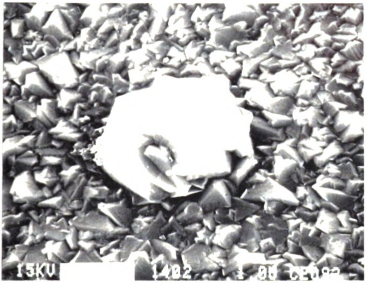

Figure 26. Twinning in specimen DF-N1-4 are indicated by arrows. A 1 micron bar is represented on the photomicrograph.

structureless particles dispersed in-between them. The particles were on the order of 5 to 10 microns across and of arbitrary shapes. What the particles were was unclear. The particles are not likely due to the thin conductive gold coating sputtered onto the films. The conductive coating, ~21 nanometer in thickness (section 2.8.2), would not be distinguishable at the magnifications at which the photomicrograph were taken.

The DTF's interfacial surfaces, as mentioned earlier (section 3.4.2), showed a very distinct difference in morphologies. The interfacial surfaces for the DF-N1, DF-N2, DF-N4, and DF-N5 films were relatively smoother with small depressions and lumps. The depressions appeared as darker spots on the surfaces while the lumps appeared as whiter spots. For the WF#25 and WF#60 films, the interfacial surfaces frequently showed distinct grain boundaries. Perhaps the different pre-deposition treatments employed in specimen preparations were responsible for this observed difference.

Films from WF#25 and WF#60 which showed grain boundaries on most of their interfacial surfaces were quite different than films DF-N1, DF-N2, DF-N4, and DF-N5 which showed no grain boundaries on their interfacial surfaces. Film WF#25 and WF#60 were photoresist treated while DF-N1, DF-N2, DF-4, and DF-N5 were abraded as pre-deposition treatments. The difference in the definition of grain boundaries as observed on the interfacial surface of the films may be related to the different pre-deposition treatments.

3.5 Raman Spectroscopy Results

Raman spectroscopy (section 2.6) verified that the deposited DTF's were indeed diamond. However, Raman spectroscopy was done only on DF-N1-6 and DF-N4-4 due to specimen size limitation. The large protective tubes on the DF-N1, DF-N2, DF-N4, and DF-N5 specc

th

the

the c

natu

ogy a

intensi

imens (Figure 8 (a)) prevented focusing of the incident beam on the diamond surfaces of the specimens. Raman spectroscopy was not performed on the specimens from sets WF#25 and WF#60. The diamond quality of the WF#25 and WF#60 films were established by the graduate student who deposited them [25]. Also, SEM pictures of WF#25 and WF#60 specimens showed distinct (111) pyramidal and (100) and (110) cubo-octrahedral diamond facets supporting the claim that WF#25 and WF#60 were indeed of good diamond quality.

Raman spectroscopy for the specimens DF-N1-6 and DF-N4-4 showed distinct 1333.5 cm^{-1} peaks (Figure 27) indicative of the presence of the diamond phase. It was assumed that all the other specimens in sets DF-N1 and DF- N4 were also of high diamond concentrations. Sets DF-N2 and DF-N5 were also assumed to be high quality diamond films (no Raman spectroscopy was done on DF-N2 and DF-N5), based only on the faceted surface textures of the DTF's of sets DF-N2 and DF-N5 as observed under the optical microscope and SEM. Also, DF-N2 and DF-N5 were fabricated in a manner similar to that of sets DF-N1 and DF-N4.

Carbons's amorphous and graphitic phases are 50 times more efficient in scattering Raman infrared radiation than diamond [5], therefore, when the diamond 1332 cm^{-1} peak dominates (Figure 27 (a) and (b)), it is probable that the diamond content is much greater than that of the amorphous and graphitic phases [5,12]. However, the relative intensities of the diamond peak and the non-diamond carbon (NDC) peak is not an absolute indication of the quality of the diamond film [26]. The intensity of the NDC peak may be sensitive to the nature of the NDC and not only the volume fraction. Variations in crystallite size, morphology and possibly the proportions of NDC with film thickness may also affect the relative intensities of the peaks. A third, and likely most frequent problem that may lead to relative

Figure 2
mond pea
observed.

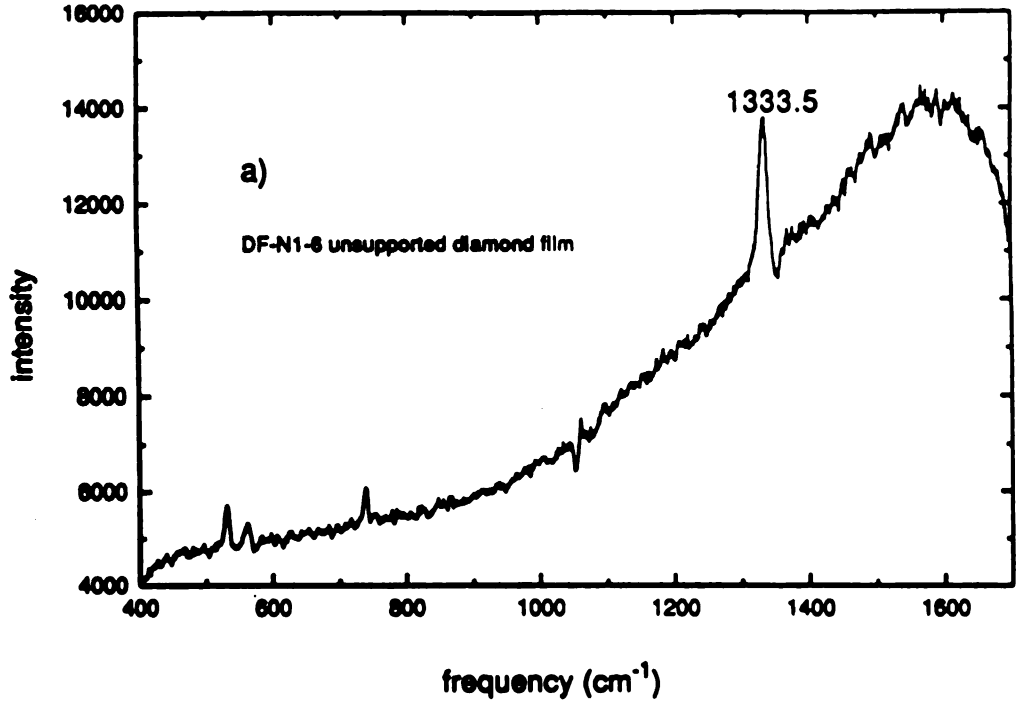

Figure 27 (**a**). Raman Spectroscopy. Raman spectra for specimen DF-N1-6 shows the characteristic 1333.5 cm^{-1} diamond peak and relatively dominant region near graphite 1500 cm^{-1} peak.

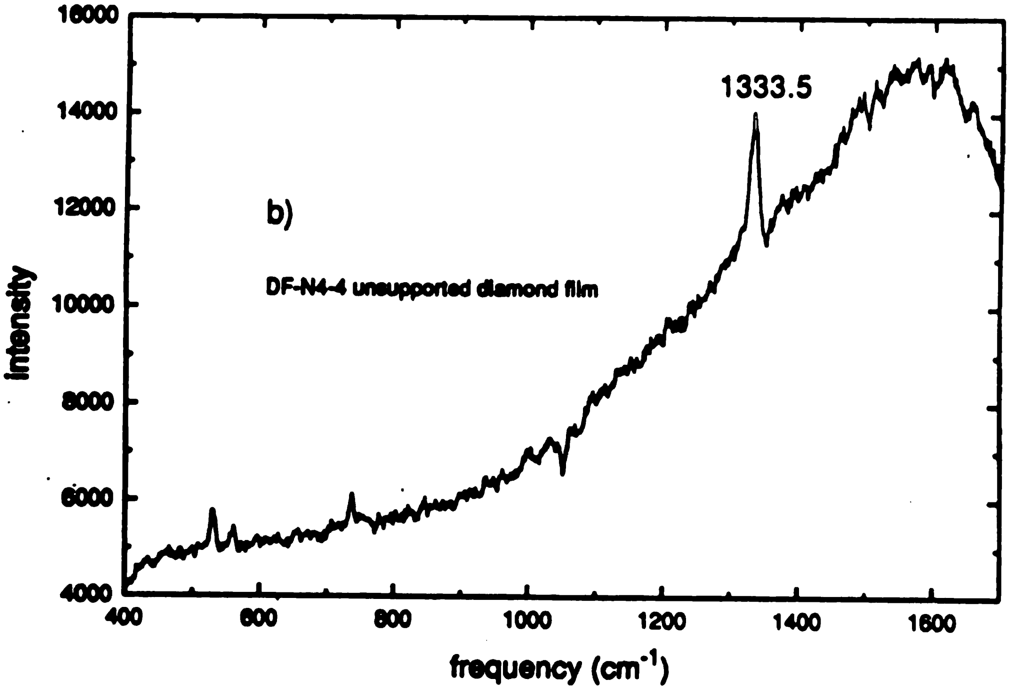

Figure 27 (**b**). Raman curve for specimen DF-N4-4. The characteristic 1333.5 cm^{-1} diamond peak and a dominant region near the characteristic 1500 cm^{-1} graphite peak is observed.

peak intensities being an inappropriate indicator of a CVD film's diamond quality is that the distribution of the NDC will also affect the intensity of the NDC peak.

As mentioned earlier, the unexpected reaction of some of the DTF's to the KOH etch may have been due to this substantial amount of non-diamond phase carbon in the film. The 1530 cm^{-1} peaks seen in both Figures 27 (a) and Figure 27 (b) may indicate the presence of a substantial graphitic phase. Although diamond is not expected to react to any chemical below ~300 °C, in some cases the KOH etch, at 60 °C, penetrated the DTF's and attacked the underlying Si substrates, often causing the DTF to fracture and curl away from the Si substrates. This effect could only happened if a non-diamond phase is present in a substantial quantity in the film and is attacked by the KOH etch. The etch would then penetrate the film by etching through the non-diamond phases and so get to attack the Si wafer beneath. However, this assumption seems unlikely since carbon is known to resist KOH etch (5 to 90 percent by weight) even at 160 °C [32].

3.6 Theoretical Modeling of the DTF Diaphragms

The DTF diaphragms formed by etching holes through the Si wafer were generally circular diaphragms supported by a silicon rim. These circular diaphragms were burst by uniformly loading them with nitrogen gas pressure to failure. The DTF diaphragms were therefore modeled as circular plates clamped at the edges and uniformly loaded in a transverse direction.

The DTF specimens' deformations and stress states were first modeled by a linear plate theory and then by a nonlinear plate theory. The pressure versus normalized deflection for the DTF diaphragms were also analyzed by an empirically derived equation. Diaphragm

The

the

tions

deflections were normalized by the thicknesses of the corresponding DTF. The actual deflections during loading were not measured. The normalized ratio, deflection over thickness, was used as a convenient way to compare the information collected on the different films.

3.6.1 Timoshenko [Linearized Model]

A classical plate theory model by Timoshenko [27] was used as a model. The circular DTF diaphragm subjected to gas pressure was modeled as a uniform and transversely loaded circular plate that is clamped along it's edge. The burst pressure (transverse load) is related to material properties and diaphragm geometry by the equation

$$P = \frac{Et^4}{3(1 - v^2)\, d^4} \left(\frac{w_0}{t} \right) \qquad (1)$$

where P is burst pressure, E is Young's modulus, v is Poisson's ratio, t is the film thickness, d is the diaphragm (film) radius, and w_0 is the maximum deflection of the film. The maximum stresses developed at the diaphragm's boundary is given by the equation [27].

$$\sigma = \frac{3}{4} \left(\frac{P d^2}{t^2} \right) \qquad (2)$$

The values determined for maximum stresses at the boundary were on the order of 10^{-6} of the 1000 GPa Young's modulus for polycrystalline diamond, or ~1 MPa.

The values for maximum deflection however, were unacceptable. Maximum deflections of nearly 1cm were calculated for the center of diaphragms that were ~0.5 cm in

S

a

lin

Cha

3.6.2

A geom

rigidly

diameter. Ceramics are not expected to deform in this manner, making the classical linear plate model inappropriate.

Timoshenko's classical plate model [27] was inadequate since it is limited to cases in which only small transverse displacements occur. Classical plate theory assumes deflections on the order of only a fraction (less than 1/3) of the thickness of the plate, so that terms involving the slope of the deflected plate's surface can be ignored [27]. Transverse displacements (displacements normal to the plane of the plate) that are on the order of the plate thickness, or greater, are too large to be treated by classical plate theory.

The DTF diaphragms in this study had diameters $\sim 10^3$ greater than their thicknesses. The geometry of these specimens thus suggests that the maximum transverse deflection may be greater than the assumed range in classical plate theory. Indeed, calculations done based on Chia's [28] nonlinear model indicated that the central deflections were 10 to 50 times greater than the plate thickness. Additionally, the measured deflections for CVD diamond diaphragms having similar thicknesses and diameters, but under point nanoindentation loading (rather than uniform loading), show maximum central deflections of more than six times the plate thickness prior to diaphragm failure [24]. The point loading was done on a nanoindentor. With deflections possibly on the order of several times the thickness, a non-linear model accommodating larger deflections seemed necessary. A non-linear model by Chia [28] was thus applied.

3.6.2 Non-linear Model

A geometrically non-linear plate model by Chia of a uniformly loaded circular plate with a rigidly clamped edge was then used to analyze the deformations and stresses of the DTF o

ten

Ho

diaphragms [28]. Chia's model accommodates deflections that are greater than the plate (diaphragm) thickness. This assumption was more appropriate for our diaphragms. Comparable deflection analysis of similar diamond diaphragms under point loading showed deflections greater than six times the plate thickness (section 3.6.1 and [24]).

Chia's model relates uniformly applied pressure to material constants and film geometry by the equation

$$P = \frac{Et^4}{3(1-\nu^2)d^4}\left[\left(\frac{w_0}{t}\right) + \frac{(1+\nu^2)(173-73\nu)}{360}\left(\frac{w_0}{t}\right)^3\right] \qquad (3)$$

where P is burst pressure, E is Young's modulus, ν is Poisson's ratio, t is the film thickness, d is the diaphragm radius, and w_0 is the maximum deflection of the film. The extreme fiber bending stress is given by the equation

$$\sigma = \frac{Et^2}{d^2}\left(\frac{4}{1-\nu}\right)\left[\left(\frac{w_0}{t}\right) + \frac{(1-\nu)(83-43\nu)}{360}\left(\frac{w_0}{t}\right)^3\right] \qquad (4)$$

For this study, the pressure P will be taken as the diaphragm burst pressure. The stresses calculated from the data using equation (3) and (4) were much greater than those determined by the linear model (section 3.6.1). The stresses calculated are on the order of 10^{-2} of the 1000 GPa Young's modulus of diamond. These large stress values, on the order of tens of Gigapascals, correspond to a maximum strain of a few percent assuming the simple Hookean constitutive relationship of

$$\sigma = E \cdot \varepsilon$$

where σ is stress, E is Young's modulus, and ε is strain.

Film deflections of ~10 to 50 times the plate thickness were calculated from Chia's geometrically non-linear model [28] which seemed intuitively more accurate than those determined by the linear model [27]. Central deflections of 10 to 50 times the diaphragm thickness seemed more credible for a diaphragm of this geometry than deflections of ~10,000 times the thickness as calculated from the linear model [27].

Both Timoshenko [27] and Chia [28] related burst pressure, radius, Young's modulus and thickness to the deflection normalized by film thickness. Equations (1) and (3) are identical except for the second term in (3), which indicates that as t/d becomes very small, the equations become identical. Banerjee [29] also shows that equation (3) characterizes the large deflections for uniformly loaded thin plate very well.

3.6.3 Analysis of WF#60 Data Points

In both equation (1) and (3) the burst pressure P is a function of the film thickness divided by the diaphragm diameter taken to the fourth power, $(t/d)^4$. Therefore the data set WF#60 was fitted to a curve of the form

$$P = \left(\frac{t}{d}\right)^4 c_1 + c_2 . \qquad (5)$$

Data set WF#60 was used because it was large compared to the other data sets, containing 21 data points. The next largest data set was for WF#25 which had 7 data points. A least-squares fit to equation (5) determined by a least-squares method gave a correlation coefficient of 0.85 with c_1 equaling 1.67×10^{16} and c_2 equaling 1.13×10^5. A correlation coeffi-

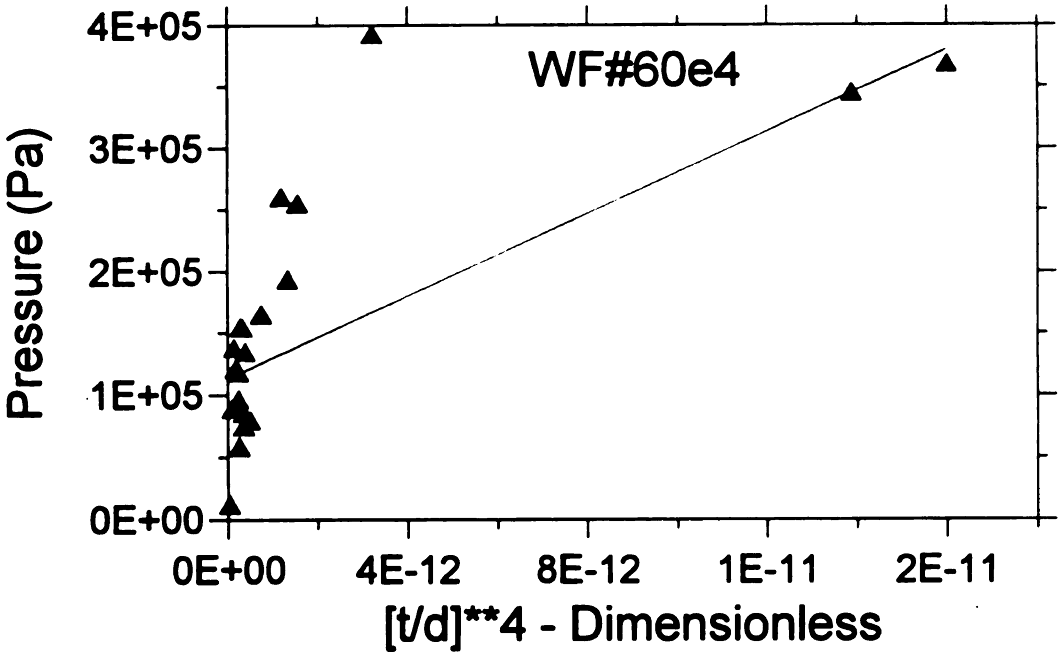

Figure 28. Plot of P versus $[t/d]^4$ for 21 WF#60 diamond films burst in this study, where P is the burst pressure , t is film thickness, and d is film diameter.

cient of 0.85 indicates no correlation, and no correlation can be seen from the fit of the data to the curve (Figure 28).

Plots of burst pressure versus the fourth power of the thickness-diameter ratio also were also made for sets DF-N1, DF-N2, DF-N4, DF-N5, and WF#25 (Appendix E). The data points were very scattered, even more so than the data for set WF#60, therefore a least-squares fit to equation (5) was not attempted for these data sets.

3.6.4 Empirical Equation

Burst pressures were also plotted (Figure 29)as a function of the non-dimensional parameter R, defined as

$$R = [t/d]^{1/2} \tag{6}$$

where t is the thickness of the film and d is the diameter of the DTF diaphragm.

The burst pressure data was fit to the equation

$$P = c_1 R + c_2 \tag{7}$$

where c_1 and c_2 are fitted constants and P is the burst pressure of the diaphragms. A least-square fit of the 21 points of data set WF#60 to equation (7) gave a correlation coefficient of 0.9 with c_1 equaling 69.9 and c_2 equaling -41.9. The removal of WF#60-5, WF#60-8, WF#60-18, and WF#60-21, the four most scattered points, gave a correlation of 0.953 with c_1 equaling 8.65×10^5 and c_2 equaling -6.73×10^5.

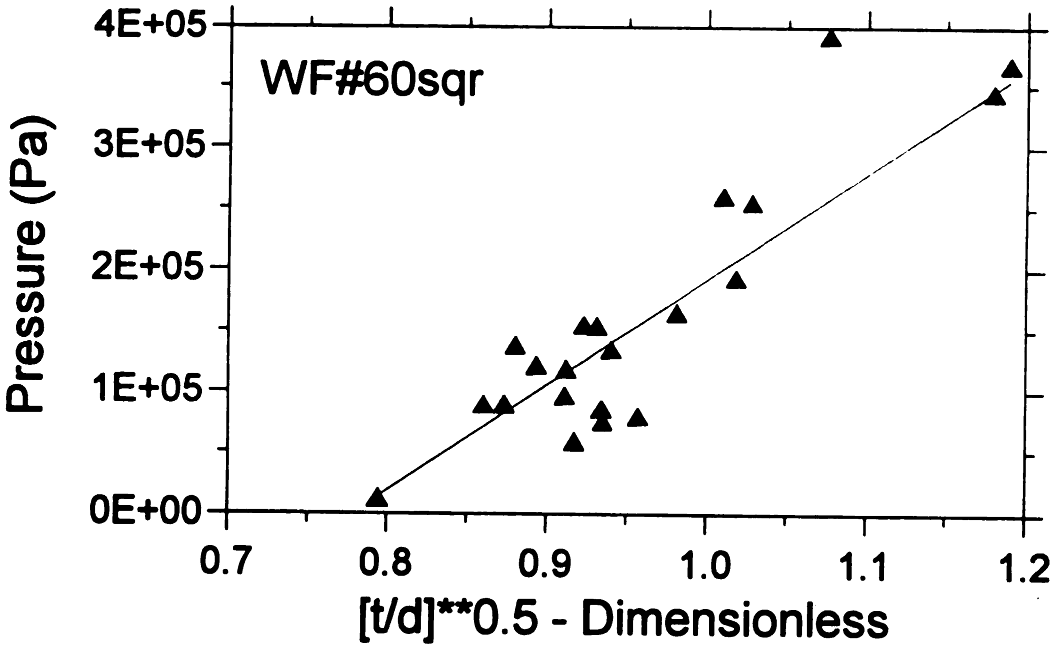

Figure 29. Plot of P versus $[t/d]^{1/2}$ for 21 WF#60 diamond films burst in this study, where P is the burst pressure , t is film thickness, and d is film diameter.

The four data points WF#60-5, WF#60-8, WF#60-18, and WF#60-21, removed from set WF#60 for the best fit exhibited no peculiarities to which their deviation from the curve fitting might be attributed. However, it is likely that the diameter measurements for specimens WF#60-5 and WF#60-21 may have both been inaccurate. The boundaries of diaphragms for WF#60-5 and WF#60-21 were difficult to determine possibly due to pinhole effects (section 3.5). The pinhole effect may occurs because the etch permeates the DTF through small holes and attacks the Si beneath. The diaphragm diameters were not clearly defined because of the pinhole effect which may have cause these data points to be scattered.

The burst pressure data also was fit to an equation of the form

$$P = c_1 X^{c2} + C_3 \tag{8}$$

where X is the ratio (t/d). Equation (7) and equation (8) fit the data equally well as determined from the nearly identical correlation coefficients obtained from regression analysis for the two equations. The correlation was 0.954 and the three free parameters c_1, c_2, and c_3 were 501,000, 0.430, and 313,000, respectively. Since equation (7) involves only two free parameters and equation (8) involves three free parameters, the curve fit was displayed only in terms of equation (7) (Figure 29).

In both equation (1) and (3), P is a function of $(t/d)^4$,while in the empirical equation (7) P is a function of $(t/d)^{1/2}$. The empirical equation (7) better represents the behavior of the limited data range collected for WF#60. Further comparison between theory and experiment would be facilitated by measurements of the central plate deflections w_0 during loading.

3.6.5 Analysis of the Total Accumulated Data Points

The total data set including all diamond diaphragms burst in this study (46 data points representing specimens from six different films) was fit to equation (7) relating burst pressure to DTF diaphragm geometry. The 7 most scattered points of the 46 points data set were taken out in order to increase the correlation coefficient. The 7 data points removed from the set were DF-N2-5, DF-N2-7, DF-N4-8, DF-N5-8, WF#25-7, WF#25-10, and WF#60-7. The constants c_1 and c_2 were 60.94 and -31.67, respectively, with a correlation coefficient of 0.674. The correlation of 0.674 is insignificant, but the values for c_1 and c_2 are interesting.

The values for c_1 and c_2 obtained from the entire data set are quite similar to those found for the best fit of data set WF#60 to equation (7). The values of c_1 and c_2 for the best fit of set WF#60 compared to c_1 and c_2 for the best fit of the entire set is for c_1, 62.17 compared to 60.94, and for $c_{2,}$ -32.38 compared to -35.14, indicating that the entire data set follows a curve similar to that of the WF#60 data set.

The correlation coefficient of 0.674 for the entire data set compared to 0.975 for the WF#60 data set may be due to several factors. First, the entire set is taken from 6 different DTF's. The different DTF's were deposited under different conditions which produces films with different physical properties, e.g. impurity content, film thickness, grain size, etc., and thus film's with different physical properties. The scattering may be partially due to these physical differences in the deposited DTF's. The data set WF#60 however, was taken from one DTF which could possibly contribute to the correlation coefficient of

0.975. Secondly, specimens DF-N1, DF-N2, DF-N4, and DF-N5 were not as circular as the diaphragms for the specimens of WF#60. The difference in circularity was due mainly to the different methods used in defining the area of the Si wafer exposed to the KOH etch (section 3.3.2 of this thesis). Thirdly, a possible cause for the scatter in the data is the shape of the Si wafer supporting the DTF diaphragms. The Si wafer tapers down to a very thin edge [24] where it supports (modeled as rigid clamped edge) the DTF diaphragm. Failure may occur only in the DTF at the edge of the diaphragm, or through the DTF and a thin part of the tapered Si wafer. If failure occurs through both the DTF and part of the tapered Si wafer, the model would not represent the boundary conditions. This misrepresented boundary conditions would cause scattering.

3.7 Other Observed Trends

The different sets of DTF's were deposited under different conditions, such as deposition time, deposition temperature, and precusor gas concentrations. Thus the physical properties of each DTF set and, most likely their mechanical behaviors, differed from set to set. Trends among the different sets might be established based on deposition conditions and the effects the conditions have on their respective films.

Sets DF-N1, DF-N2, DF-N4, and DF-N5 were deposited under differing microwave powers, differing methane concentrations, and for different deposition times. Increasing the power of the microwave generator, with all other parameters held constant, is expected to yield a high film growth rate[10]. Increasing the methane concentration, with all other parameters held constant, is expected to increase the likelihood of producing a graphitic carbon film [14], and also to increase the film growth rate [12,30]. Increasing the deposition time, with all other parameters held constant, is expected to yield thicker diamond films simply, because after an initially high rate the film thickness growth rate slows to being pretty much constant [18]. Longer deposition times is also expected to yield films with larger facets (grain sizes), because grain size increases with film thickness [12]. These trends can be investigated in the data collected from sets DF-N1, DF-N2, DF-N4, and DF-N5.

The specimens from sets DF-N1, DF-N2, DF-N4, and DF-N5 were investigated for their burst pressures, diaphragm diameters, film thicknesses, and grain sizes. From two to six DTF specimens were tested from each of these four sets. The size of these sets was deemed too small for any substantial inferences to be made, therefore only the trends observed were addressed.

3.7.1 Thickness Variation

The film thicknesses for sets DF-N1, DF-N2, DF-N4, and DF-N5 varied from 1.9 to 4.7 microns (Table 2). The film thickness of set WF#25 varied from 2.2 to 5.0 microns (Table 3). The film thickness for DTF WF#60 varied from 2.0 to 4.4 microns (Table 4).

Sets DF-N1, DF-N2, and DF-N5 differed only in their deposition times. The deposition times for DF-N1, DF-N2, and DF-N5 were 6, 8, and 10 hours respectively. The average film thicknesses for these three sets were 2.2 microns for DF-N1, 2.5 microns for DF-N2, and 4.3 microns for DF-N5. Increasing deposition time results in an increasing film thickness. The time increases were in 2 hour increments, but a corresponding incremental increase in film thickness was not observed. If thickness increases proportionally with time [18], an incremental increase in film thickness would be expected for the incremental increase in deposition time. However, the set sizes were 2 data points for set DF-N1, 5 data points for set DF-N2, and 6 data points for set DF-N5, and the DTF's thickness distribution over the substrate is known to vary considerably from thicker at the center of the substrate to thinner at the edges [21] (also section 3.7.1.1). Perhaps the small data sets, especially DF-N1, made them inadequate in exhibiting incremental increases between films with expected thickness variations.

3.7.1.1 Thickness versus Wafer Position

The relative positions of the 26 specimens taken from WF#60 were recorded and compared to corresponding film thicknesses. The pattern noticed is one of decreasing thickness with increasing of the radial distance from the center of the deposition plasma (Figure 30) and [24]. The thickness variation might be attributed to the temperature variation that also decreases from the center to the edges [21].

3.7.2 Grain Size Variation

The burst pressure versus square root of grain size was plotted for the six different sets of specimens (Appendix F). No pattern was evident from the plots. The data seemed very scattered and without any correlation between burst pressure and grain size for this range of grain sizes. It is possible that the lack of correlation between burst pressure and grain size is due to the narrow range of grain sizes tested. The grain sizes from sets DF-N1, DF-N2, DF-N4, and DF-N5 ranged from 0.33 to 1.12 microns (Table 2). The grain sizes of the DTF's taken from WF#25 varied from 0.47 to 0.99 microns (Table 3), and for WF#60 the grain size varied from 0.54 to 1.26 microns (Table 4).

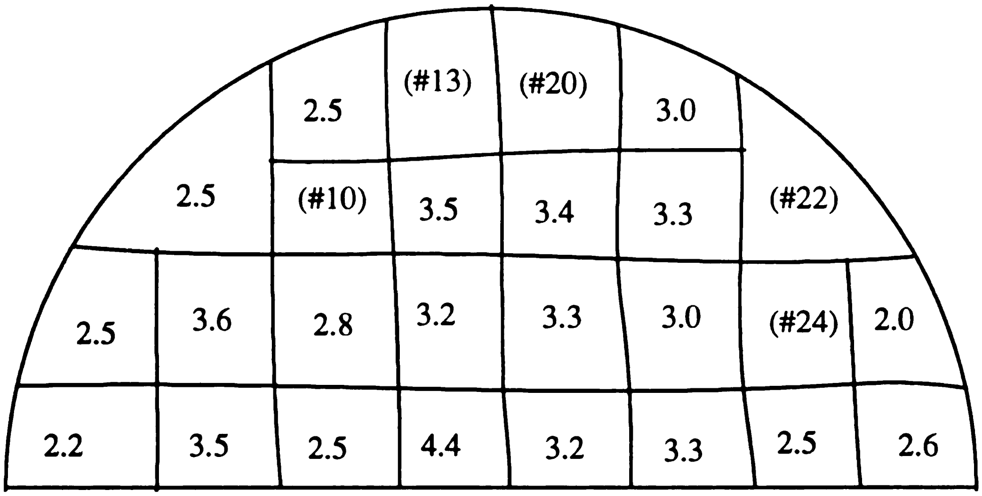

Figure 30. Thickness versus Position for WF#60. No thickness values were obtained for specimens #10, #13, #20, #22, and #24. A slight pattern of thickness decreasing with increasing radial distance from the bottom center is observed. This pattern might be due to a higher substrate temperature corresponding to a thicker regions of the deposited DTF [21].

In cases where the initial flaw is limited by the grain size, and scales with grain size, and in which brittle behavior is observed, strength (considered to be burst pressure) should vary with grain size as [31],

$$\sigma_f = K \cdot d^{-1/2}.$$

Due to the relatively narrow grain size range of ~0.9 micron to ~1.2 microns, the corresponding square root of grain size range is 0.949 $\mu m^{1/2}$ to 1.09 $\mu m^{1/2}$. The square root range varies by only a ~15 percent of its lowest value, therefore the expected effect on burst pressure would only be a 15 percent change.

The range of the grain size data collected in this study may have been too narrow to make a grain size versus burst pressure investigation. However, in studies involving a wider range of grain sizes, microstructural effects may be very significant and should be investigated.

Grain size tends to increase as DTF thickness increases. For sets of DTF's having an increasing average thicknesses (DF-N1, DF-N2, and DF-N5) the associated average grain sizes are 1.00, 0.65, and 0.79 microns, respectively. The average grain size of 1.00 microns for the DF-N1 set does not conform to the expected trend. However, only two specimens from set DF-N1 were tested, and not the average grain size over the entire DTF.

When it was possible, the grain size on the interfacial surface of the DTF's were determined. Grain boundaries on the interfacial surface of the DTF's were evident only for some WF#25 and WF#60 specimens. Two interfacial grain size determinations were make from the seven WF#25 films tested and nine from the twenty one WF#60 films tested. Interfacial grain size determinations were limited to SEM photomicrographs which showed well defined interfacial grains which is why only a total of 11 interfacial grain size determinations were made although several other photomicrographs from WF#25 and WF#60 showed a similar structure on their surfaces. Interfacial grain sizes are presented in Table 3 for the WF#25 films and Table 4 for the WF#60 films

The grain sizes of the interfacial and deposition surfaces of the same film were compared to determine if indeed grain size in polycrystalline diamond films increased with film thickness. If so, the grain size of the deposition surface should be larger than the grain size of the interfacial surface for the same film. Two of the nine interfacial grain sizes from set WF#60 were larger than their corresponding deposition surface grain sizes. This would support the what is expected. Two of the two interfacial grain sizes from set WF#25 were larger than their corresponding deposition surface grain sizes. This is not as would be expected. Perhaps again the sample size of two is just too small.

3.7.3 Temperature Variation

Sets DF-N1, and DF-N4 had the same deposition conditions except for the microwave power used in their deposition. The microwave power used for depositing DF-N1 was 900 watts, and for DF-N4 it was 700 watts. The associated specimen surface temperatures were ~800 °C at 900 watts, and ~760 °C at 700 watts (section 2.2.2). The Raman spectroscopy for specimens DF-N1 and DF-N4 (Figure 26) did not show differences in the relative intensities of the diamond peaks that might indicate the degree of the diamond content. Higher temperatures typically produce diamonds of higher purity [8,11,18].

As mentioned earlier (section 3.7.1.1) the film thickness versus film position noted across the Si wafer is likely attributable to the temperature variation across the wafer during deposition.

Another observation made from the photomicrographs was the difference that pyramidal (111) faces dominated the DF-N1, DF-N2, DF-N4, DF-N5 and WF#25 specimens' deposition surfaces, but square (110) and/or (100) faces dominated the WF#60 specimens' deposition surfaces. The different faces are known to dominate at different temperatures. The (100) faces usually dominates at the lower temperatures than the (111) faces which usually dominate between 750 °C and 1,000 °C [19].

Sets DF-N1, DF-N2, and DF-N5 were deposited at approximately 774 °C, set DF-N4 at approximately 766 °C, WF#25 at approximately 850 °C, and WF#60 at approximately 776 °C. All sets were deposited between 750 °C and 1,000 °C and are expected to show deposition surfaces dominated by pyramidal (111) faces. However, the WF#60 set shows a square (110) and/or (100) dominated surface.

4. Conclusions

A more reproducible method for abrasion would aid in standardizing the deposition procedure. Abrasion is done to increase the nucleation site density on the substrate. Nucleation site density strongly affects the adhesion of the DTF to its substrate [21] and thus is an important parameter to control. Although SEM surface replication technique may be used to determine nucleation site density , a method in which the site density can be prescribed may still be very desirable necessary. SEM testing of Si wafers that have been submerged for different periods of times in an ultasonic bath of diamond powder suspension might be tried to see if alteration in an ultrasonic bath of diamond suspension would ofter a method of producing a prescribed nucleation site density.

The different methods of nucleation site generation, abrasion and photoresist treatments, show a distinguishable difference in the morphology of the interfacial surfaces of the DTF's. No adhesion tests were done on these different DTF coatings but it would be interesting to see if differences in adhesion were associated with this morphological difference.

The modelling of the diaphragms as uniformly loaded plates with clamped edges is acceptable as a rough estimate for the particular DTF specimen included in this study. The Si rims supporting the diamond diaphragms for the specimens fabricated by using small tubes to define the holes etched through the Si wafers were not observed under the SEM. Therefore nothing is know of the shape and thickness of the Si rims where they supported the diamond diaphragms. The edges of the diamond diaphragms fabricated by dimpling were supported by a very thin Si rim [24]. The support of the edges of the diaphragms might not satisfy the assumed boundary conditions of the model. Changes must be made in either the fabrication of the diaphragms or the modelling of the diaphragms' boundary conditions.

APPENDICES

APPENDIX A

Micrographs of some specimens from sets DF-N1, DF-N2, DF-N4, and DF-N5. The micrographs are presented in the order of grain sizes, thicknesses, and other observations.

Appendix A. I. Grain Sizes.

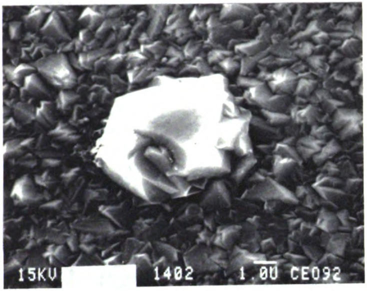

Figure A1. The deposition surface of DF-N1-4. A large grain is seen at the center of the micrograph. A 1 micron length is indicated.

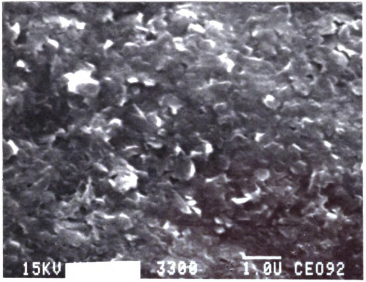

Figure A2. The deposition surface of DF-N3-3. No diamond facets are observed, therefore this film was consider (as was the entire set of DF-N3 films) to be mostly graphitic carbon. A 1 micron bar is indicated.

Appendix A. I. Grain Sizes.

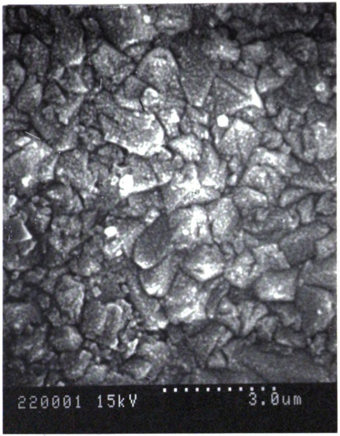

Figure A3. The deposition surface of DF-N2-2. A grain size of 0.53 microns was determined from this micrograph. The film appears to be covered with minute lumps. A 3 micron dot-bar is indicated.

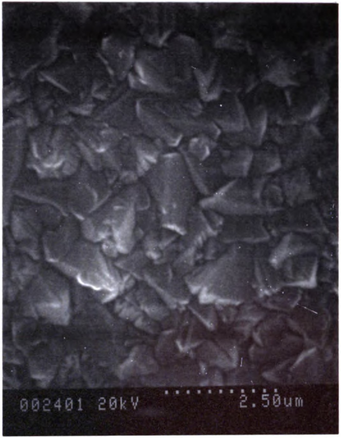

Figure A4. The deposition surface of DF-N2-4. The surface is dominated by (111) facets. A grain size of ~0.65 micron is seen. A 2.5 micron dot-bar is indicated.

Appendix A. I. Grain Sizes.

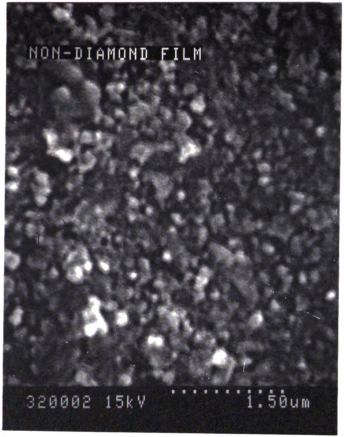

Figure A5. The non-diamond film DF-N3-2. The typical (111), (100),and (110) facets are not present. A 1.5 micron dot-bar is indicated.

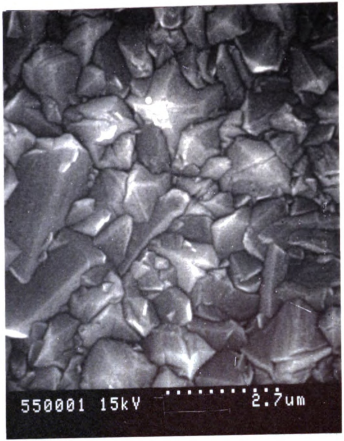

Figure A6. The deposition surface of DF-N5-5. Pyramidal (111) facets dominate the surface. A 2.7 micron dot-bar is indicated.

Appendix A. I. Grain Sizes.

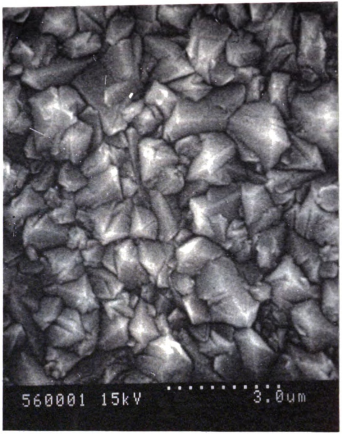

Figure A7. The deposition surface of DF-N5-6. The surface is dominated by (111) facets. A grain size of 0.64 micron was determined from this micrograph. A 3.0 micron dot-bar is indicated.

Appendix A. II. Thicknesses.

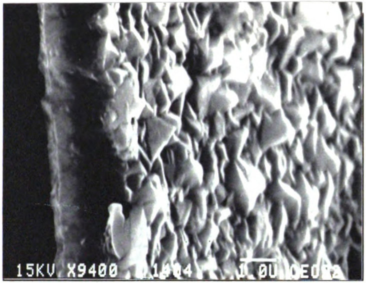

Figure A8. The deposition (top) surface and edge of DF-N1-4. The top surface is dominated by pyramidal (111) facets. Columnar structure is see on the edge of the film. A 1 micron bar is indicated.

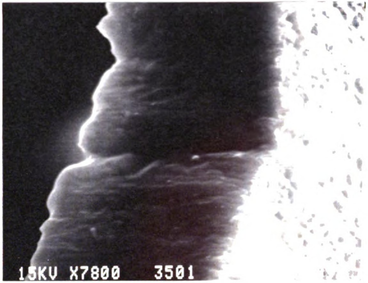

Figure A9. The edge of DF-N3-5. No columnar structure is evident through the thickness. A thickness of 6.4 was determined from this micrograph. A 1 micron bar is indicated.

Appendix A. II. Thicknesses.

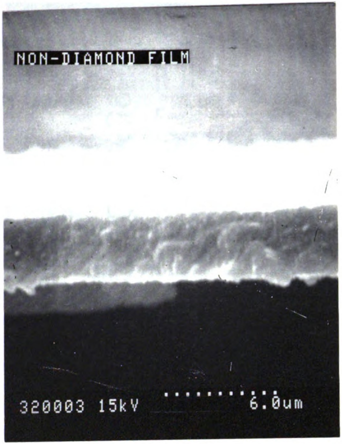

Figure A10. The edge view of DF-N3-2. No columnar structure is evident through the edge. The thickness determined from this micrograph is 3.5 microns. A 6 micron dot-bar is indicated.

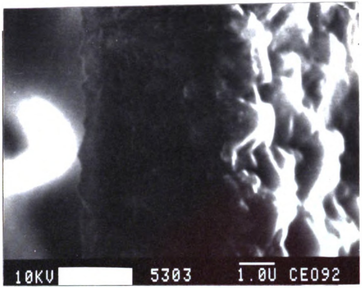

Figure A11. The edge view of DF-N5-3. A thickness of 3.7 micron was determined for this DTF. The dominant (111) pyramidal facets on the deposition surface and the columnar structures through the thickness are both evident. A 1 micron bar is indicated.

Appendix A. II. Thicknesses.

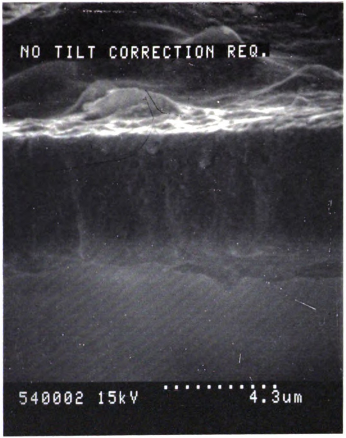

Figure A12. The edge view of DF-N5-4. A thickness of 4.3 microns was determined from this micrograph. Small lumps on the interfacial surface is also obvious. A 4.3 micron dot-bar is indicated.

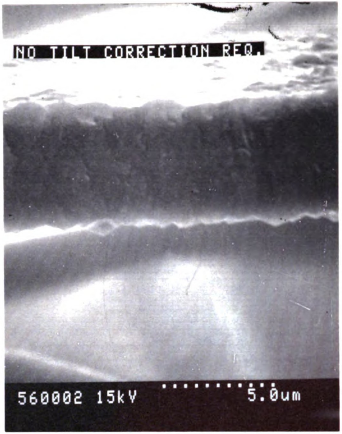

Figure A13. The thickness of DF-N5-6 was determined to be 5.3 microns from this micrograph. A 5 micron dot-bar is indicated.

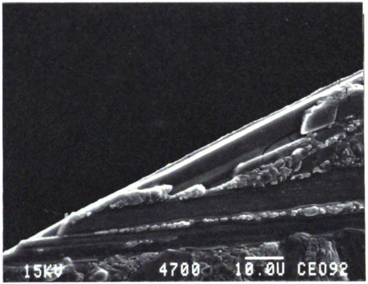

Figure A14. The bottom of the Si wafer supporting DF-N4-7. The morphology is the result of etching the (100) single crystal Si wafer in a potassium hydroxide (KOH) bath (section 2.4.2). A 10 micron bar is indicated.

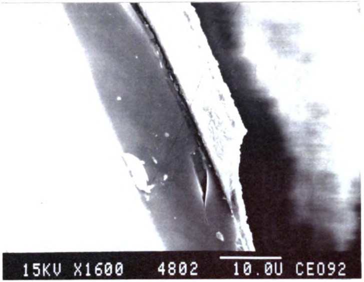

Figure A15. The edge and bottom view of the Si wafer supporting specimen DF-N4-8. The Si wafer is the thicker material. The edge and bottom of the diamond thin film (DTF) is also see. A 10 micron bar is indicated.

Appendix A. III. Other Observations

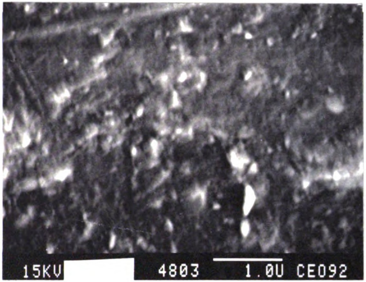

Figure A16. The interfacial surface of DF-N4-8. The surface is flat with a few scattered lumps. A 1 micron bar is indicated.

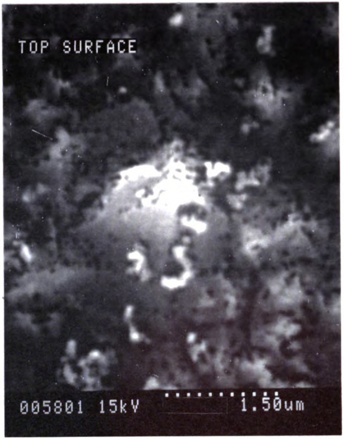

Figure A17. The deposition surface of DF-N5-8. At high (x20k) magnification minute black dots are seen on the facets. Small structure that do not resemble square or pyramidal diamond face are also see. A 1.5 micron dot-bar is indicated.

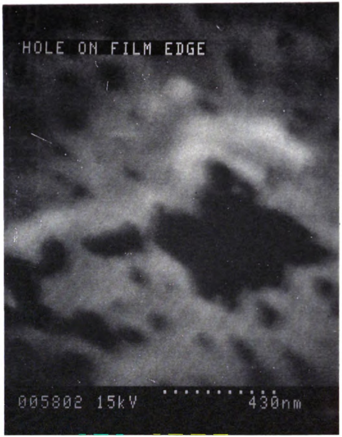

Figure A18. A high (x70k) magnification of the deposition surface of DF-N5-8. The small black dots on the surface (see Figure A17) appears to be holes, perhaps through the gold coating (section 2.8.2). A 430 nm dot-bar is indicated.

APPENDIX B

Micrographs of some specimens from WF#25. The micrographs are presented in the order of grains sizes, thicknesses, diaphragm diameters, and interfacial grains.

Appendix B. I. Grain Sizes.

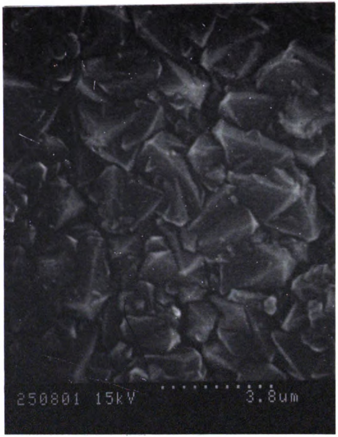

Figure B1.The Deposition surface for WF#25-8. The surface is dominated by (111) faces. A grain size of 0.75 microns was determined.A 3.8 micron dot-bar is indicated.

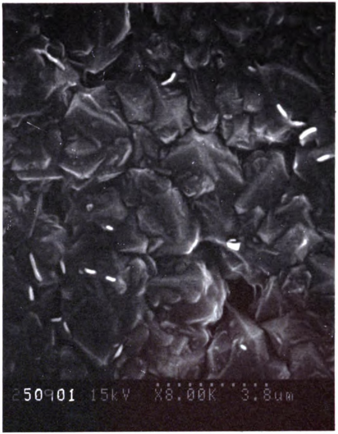

Figure B2. The deposition surface of WF#25-9. The (111) faces dominate the surface. A few large cracks are observed. A grain size of 0.6 micron was determined. A 3.8 micron dot-bar is indicated.

Appendix B. I. Grain Sizes.

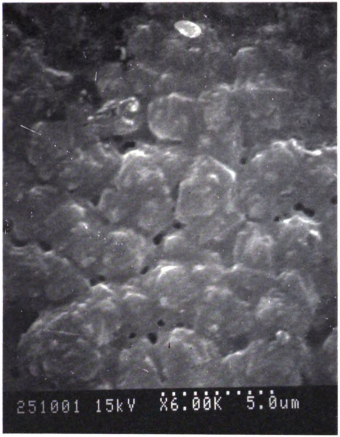

Figure B3. The deposition surface of WF#25-10. The grains are not well defined. Small holes are seen at the grain boundaries. A grain size of 0.99 was determined. A 5 micron dot-bar is indicated.

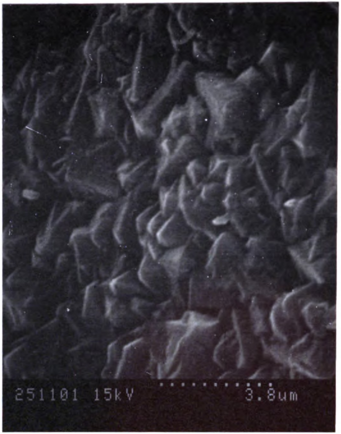

Figure B4. The deposition surface of WF#25-11. The (111) faces dominate the surface. A grain size of 0.67 was determined. A 3.8 micron dot-bar is indicated.

Appendix B. I. Grain Sizes.

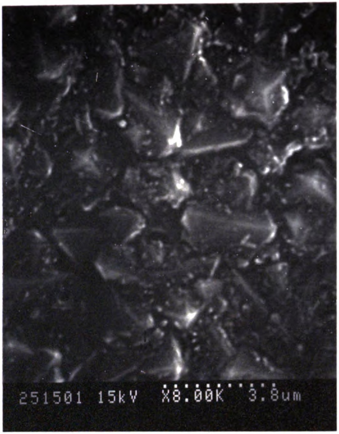

Figure B5. The deposition surface of WF#25-15. The (111) faces dominate the surface. A grain size of 0.47 micron was determined. A 3.8 micron dot-bar is indicated.

Appendix B. II. Thicknesses.

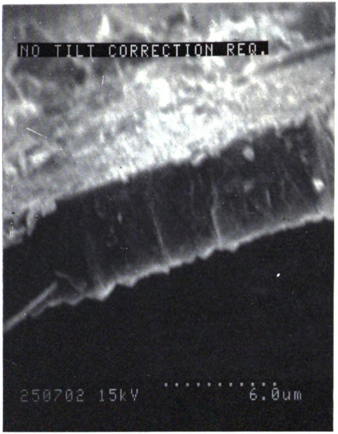

Figure B6. The edge view of WF#25-7. The edge surface was nearly parallel and showing the true length thus no tilt correction was applied. A thickness of 5 microns was determined. A 6 micron dot-bar is indicated.

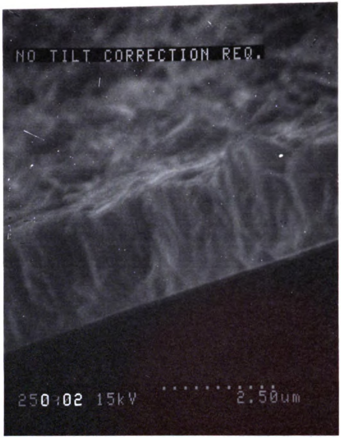

Figure B7. The edge view of WF#25-9. Columnar structure across the edge is evident. No tilt correction was required. A thickness of 2.3 was determined. A 2.5 micron dot-bar is indicated.

Appendix B. III. Diaphragm Diameters.

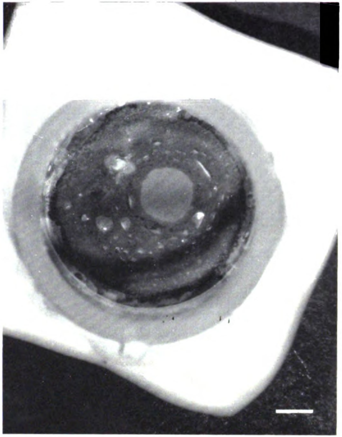

Figure B8. The diamond diaphragm (light circular center) of specimen WF#25-7. Many DTF blisters are observed on the Si, possibly due to pinholes allowing the etch to attack the Si beneath the DTF. The bar represents 1.3 mm.

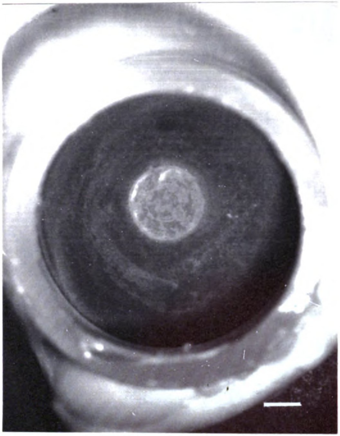

Figure B9. The diamond diaphragm (light circular center) of specimen WF#25-10. The good circularity obtained from initial dimpling is obvious. The bar represents 1 mm.

Appendix B. III. Diaphragm Diameters.

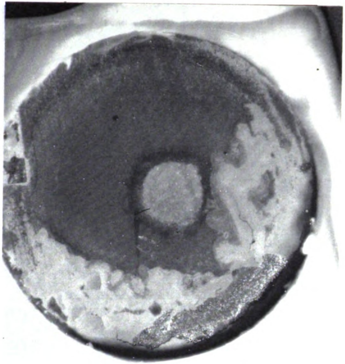

Figure B10. The diamond diaphragm (light circular center) of specimen WF#25-12. The DTF blistering is severe and causes the DTF to flake from the Si substrate. The bar represents 1 mm.

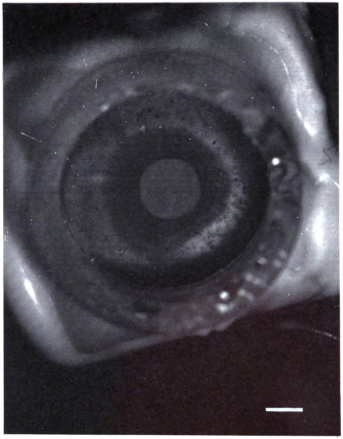

Figure B11.The diaphragm (light circular center) of specimen WF#25-14. The Torr Seal is seen on the outer edges surrounding the protective fused silica tube. Inside the tube is seen the DTF on Si and the diaphragm. The bar represents 1.3 mm.

Appendix B. IV. Interfacial Grains.

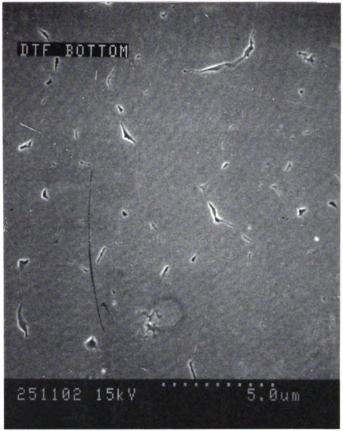

Figure B12. The interfacial surface of WF#25-11. The individual grains are partially distinguishable. A grain size of 0.71 microns was determined from this micrograph. A dot-bar of 5 micron is indicated.

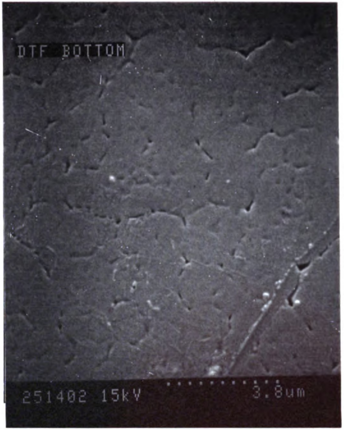

Figure B13. The interfacial surface of WF#25-14. The individual grains are distinguishable. A grain size of 0.86 microns was determined from this micrograph. A dot-bar of 3.8 micron is indicated.

APPENDIX C

Micrographs of some specimens from WF#60. The micrographs are presented in the order grain sizes, thicknesses, diaphragm diameters, interfacial grains, and other observations.

Appendix C. I. Grains Sizes.

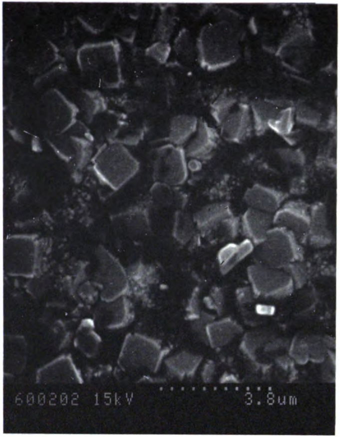

Figure C1.The deposition surface of specimen WF#60-2. The square facets of the (110) or (100) crystals. A grain size of 1.14 microns was determined from this micrograph. A 3.8 microns dot-bar is indicated.

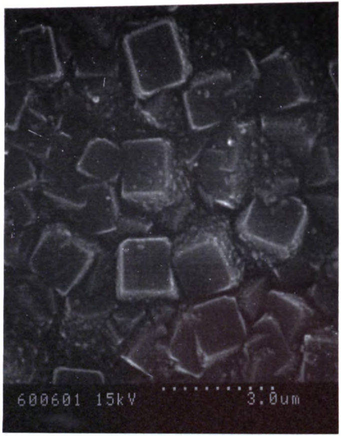

Figure C2. The deposition surface of specimen WF#60-6. The square facets of the (110) or (100) crystals. A grain size of 1.04 microns was determined from this micrograph. A 3 microns dot-bar is indicated.

Appendix C. I. Grains Sizes.

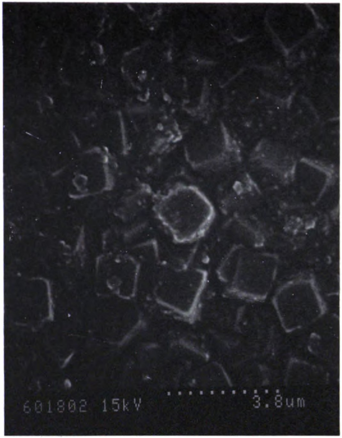

Figure C3. The deposition surface of specimen WF#60-18. The square facets of the (110) or (100) crystals. A grain size of 1.2 microns was determined from this micrograph. A 3.8 microns dot-bar is indicated.

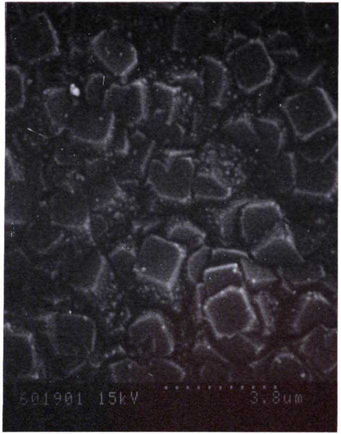

Figure C4. The deposition surface of specimen WF#60-19. The square facets of the (110) or (100) crystals. A grain size of 1.26 microns was determined from this micrograph. A 3.8 microns dot-bar is indicated.

Appendix C. II. Thicknesses.

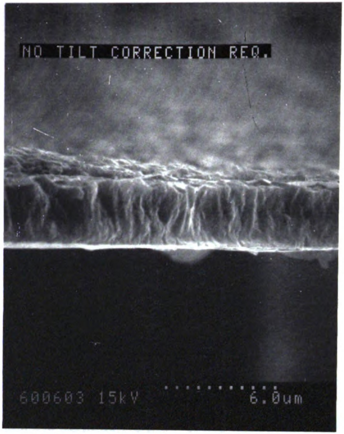

Figure C5. The edge view of specimen WF#60-6. A thickness of 3.6 microns was determined from this micrograph. Columnar structures of the diamond crystals are obvious across the thickness. A 6 micron dot-bar is indicated.

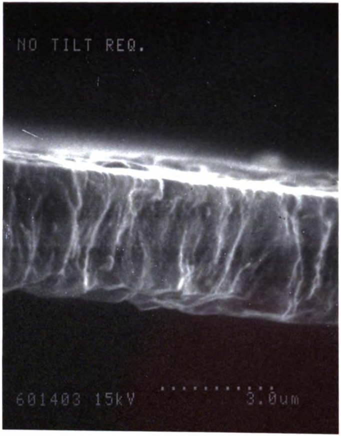

Figure C6. The edge view of specimen WF#60-14. A thickness of 3.2 microns was determined from this micrograph. Columnar structures of the diamond crystals are obvious across the thickness. A 3 micron dot-bar is indicated.

Appendix C. II. Thicknesses.

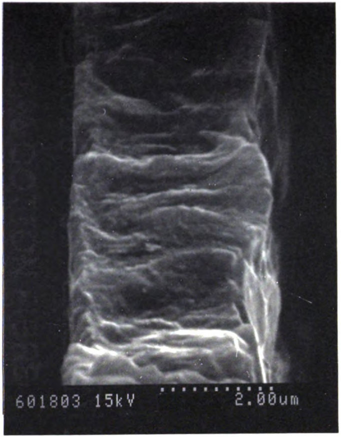

Figure C7. The edge view of specimen WF#60-18. A thickness of 3.4 microns was determined from this micrograph. Columnar structures of the diamond crystals are obvious across the thickness. A 2 micron dot-bar is indicated.

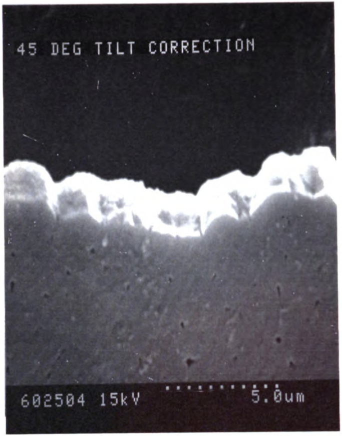

Figure C8. The edge and bottom of specimen WF#60-25. Columnar structures of the diamond crystals across the thickness are obvious. A 5 micron dot-bar is indicated.

Appendix C. III. Diaphragm Diameters.

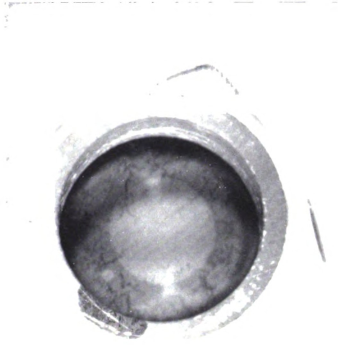

Figure C9.The diaphragm (light circular center) of specimen WF#60-6. White Torr Seal epoxy is seen outside of the protective fused silica tube. Inside the tube, are the DTF on Si (dark area), and the diaphragm are seen. The bar represents 1.3 mm.

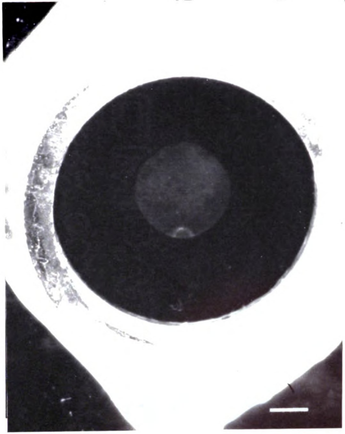

Figure C10. The diaphragm (light circular center) of specimen WF#60-12. The Torr Seal is on the outer edges and surrounds the protective fused silica tube. Inside the tube, are the DTF on Si (dark area), and the diaphragm. The bar represents 1mm.

Appendix C. III. Diaphragm Diameters.

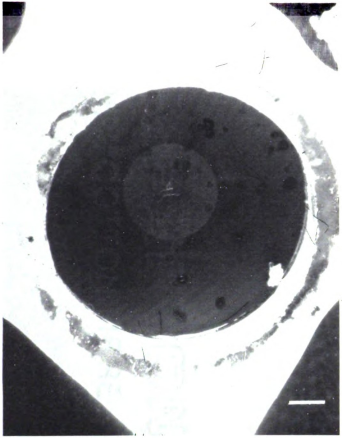

Figure C11. The diaphragm (light circular center) of specimen WF#60-15. The Torr Seal is on the outer edges surrounds the protective fused silica tube. Inside the tube are the DTF on Si (dark area), and the diaphragm. The bar represents 1 mm.

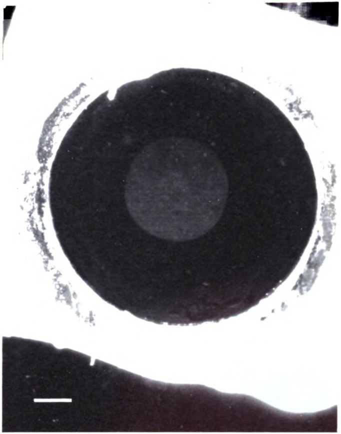

Figure C12. The diaphragm (light circular center) of specimen WF#60-23. The Torr Seal on the outer edges surrounds the protective fused silica tube. Inside the tube are the DTF on Si (dark area), and the diaphragm. The bar represents 1 mm.

Appendix C. IV. Interfacial Grains.

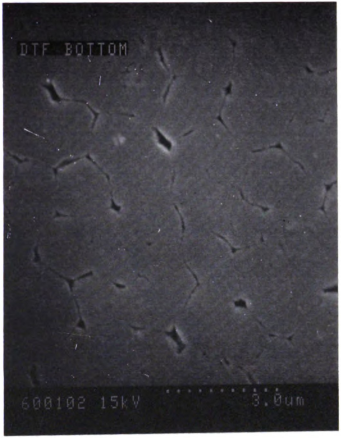

Figure C13. The interfacial surface of specimen WF#60-1. The individual grains are well defined. A grain size of 1.00 microns was determined form this micrograph. A 3 micron dot-bar is indicated.

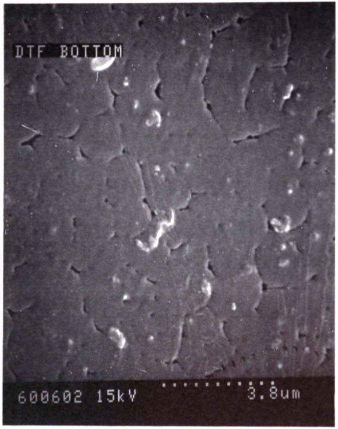

Figure C14. The interfacial surface of specimen WF#60-6. The individual grains are well defined. A grain size of 0.98 microns was determined form this micrograph. A 3.8 micron dot-bar is indicated.

Appendix C. IV. Interfacial Grains.

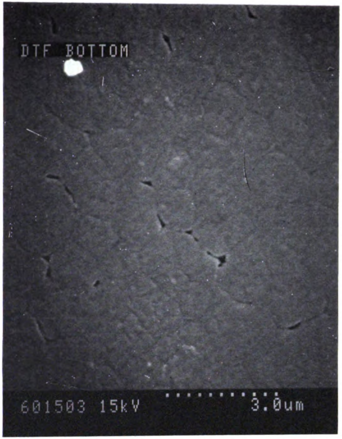

Figure C15. The interfacial surface of specimen WF#60-15. The individual grains are well defined. A grain size of 0.82 microns was determined form this micrograph. A 3 micron dot-bar is indicated.

Figure C16. The interfacial surface of specimen WF#60-17. The individual grains are well defined. A grain size of 1.01 microns was determined form this micrograph. A 3.8 micron dot-bar is indicated.

Appendix C. V. Other Observations.

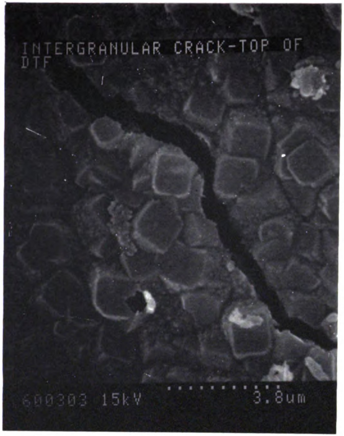

Figure C17. A crack on the deposition surface of specimen WF#60-3. Square (110) or (100) dominate the morphology. Some intragranular cracks appears to be present. A dot-bar of 3.8 microns is indicated.

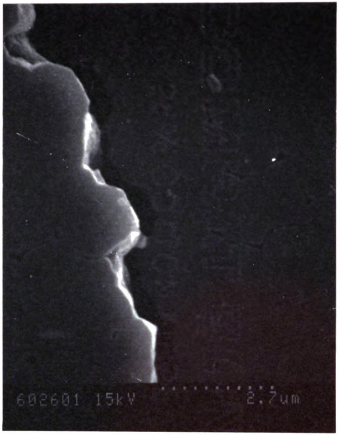

Figure C18. A crack on the interfacial surface of specimen WF#60-26. This crack is clearly intergranular. A dot-bar of 2.7 microns is indicated.

APPENDIX D

Data Acquisition Program. The program was written in quick basic. The data point s are read continuously during testing, and 2.33 points are saved every second. Five points are read and the highest one is written to the created file. After the test is stopped, the highest value written to the data file is also written on the monitor

APPENDIX D

```
'       HENRY.BAS

'       This program seems to work OK


        DIM D%(8)

        DIM DAT%(1000), CHAN%(1000)

        COMMON SHARED D%(), CHAN%(), DAT%()

        DECLARE SUB CIO8 (MD%, BYVAL ANYTHING%, F%)


        '$DYNAMIC

        DIM RAWDAT%(2000)

        '$STATIC

        Delay = 4

        NumOfPoints = 1


'---------- Initialize section -------------------------------------


        BA% = &H200                             ' Set the Base Address

        MD% = 0                                 ' Set Mode number to 0

        D%(0) = BA%                             '

        CALL CIO8(MD%, VARPTR(D%(0)), F%)       ' Send Initialization

        IF F% <> 0 THEN                         ' If there was a problem...

           GOSUB CallErrorCodes                 '

           CLS : PRINT "INITIALIZATION FAILURE" '

           PRINT Mes$: STOP                     '

        END IF                                  '

                                                '

        OUT (BA% + 3), 8                        ' Set the gain register


'       --------------------------------------------------------------------

'       Get the starting voltage to record
```

APPENDIX D

```
        CLS
        PRINT : PRINT STRING$(80, "=");
75      LOCATE 10, 10: PRINT STRING$(69, " ")
        LOCATE 12, 10: PRINT STRING$(69, " "): LOCATE 10, 10
        INPUT "Enter the pressure to start recording (in psi) ", Target$
        Target = VAL(Target$)

        LOCATE 12, 10
        PRINT USING "Using a value of ###.## psi, is this correct (Y/N) ?"; Target
100     OP$ = INKEY$: IF OP$ = "" THEN GOTO 100
        IF UCASE$(OP$) <> "Y" THEN GOTO 75

'       -----------------------------------------------------------------
'       Get the filename to save the data in

175     LOCATE 14, 10
        PRINT "Enter the name of the file to save data in (include paths) "
        LOCATE 15, 15: PRINT STRING$(64, " ")
        LOCATE 15, 15: INPUT "", FileName$
        ON ERROR GOTO 200
        OPEN FileName$ FOR OUTPUT AS #1
        GOTO 300

'       -----------------------------------------------------------------
'       Error routine if the file cannot be created

200     LOCATE 17, 10
        PRINT "There was a problem opening the file "; FileName$
        LOCATE 19, 10
```

```
        PRINT "Press any key to enter a different filename "
        DO WHILE (INKEY$ = ""): LOOP
        LOCATE 17, 10: PRINT STRING$(69, " ")
        LOCATE 19, 10: PRINT STRING$(69, " ")
        RESUME 175

'       -------------------------------------------------------------------
'       Set up the main screen

300     ON ERROR GOTO 0
        CLS
        COLOR 1
        LOCATE 8, 31: PRINT "Current Pressure"
        COLOR 12
        LOCATE 10, 33: PRINT "èèèèèèèèèèèèè£"
        LOCATE 11, 33: PRINT "¤            ¤"
        LOCATE 12, 33: PRINT "àèèèèèèèèèèè¥"
        COLOR 4
        LOCATE 16, 20
        PRINT USING "Waiting for the pressure to reach ###.## psi"; Target
        LOCATE 22, 23: PRINT "<< Press 'X' to halt the program >>";
        COLOR 12: LOCATE 22, 33: PRINT "X": COLOR 4

'       -------------------------------------------------------------------
'       Wait for the voltage to get high enough

400     OP$ = INKEY$: IF UCASE$(OP$) = "X" THEN GOTO Done2
        GOSUB Convert
        LOCATE 11, 36: PRINT USING "###.##"; Pressure;
        IF Pressure >= Target THEN GOTO 500 ELSE GOTO 400
```

APPENDIX D

```
'       ----------------------------------------------------------------
'       Start recording data


500     LOCATE 16, 20:  PRINT STRING$(50, " ")
        LOCATE 16, 20
        PRINT "            Recording data..."
        StartTime = TIMER
        PRINT #1, (TIMER - StartTime), Pressure

550     FOR x = 1 TO Delay
            LOCATE 16, 50: PRINT "/";
            GOSUB Convert
            IF Pressure >= MaxPressure THEN MaxPressure = Pressure
            LOCATE 11, 36: PRINT USING "###.##"; Pressure;
            OP$ = INKEY$: IF UCASE$(OP$) = "X" THEN GOTO Done1
        NEXT x

        PRINT #1, (TIMER - StartTime), Pressure
        LOCATE 16, 50: PRINT "\";
        NumOfPoints = NumOfPoints + 1
        OP$ = INKEY$: IF UCASE$(OP$) = "X" THEN GOTO Done1
        GOTO 550

'       ----------------------------------------------------------------
Convert:
        OUT (BA% + 2), 0                        ' Set channel number
        FOR k1 = 1 TO 10: NEXT k1               ' Slight pause
        OUT (BA% + 1), 0                        ' Trigger conversion
EOCLOOP:
```

APPENDIX D

```
        EOC = INP(BA% + 2) AND 128
        IF EOC = 128 THEN GOTO EOCLOOP          ' Checks in conversion is done
        XL% = INP(BA%)                          ' Read in low byte
        FOR k1 = 1 TO 10: NEXT k1               ' Slight pause
        XH% = INP(BA% + 1)                      ' Read in high byte
        ydata = XH% * 16 + XL% / 16 - 2048      ' Combine data
        Volts = ydata * (20 / 4096)
        Pressure = Volts * 10
RETURN

'       ----------------------------------------------------------------
Done1:
        CLS
        CLOSE
        LOCATE 10, 10
        PRINT "The data was saved in a file called "; FileName$
        LOCATE 12, 10
        PRINT USING "Data was recorded for ####.# seconds."; (TIMER - StartTime)
        LOCATE 14, 10
        PRINT NumOfPoints; " data points were saved."
        LOCATE 16, 10
        PRINT USING "Average points/second ##.## "; (NumOfPoints / (TIMER - StartTim
        LOCATE 18, 10
        PRINT "The maximum pressure was "; MaxPressure
        PRINT : PRINT : PRINT
        END

'       ----------------------------------------------------------------
Done2:
        CLS
```

```
        CLOSE

        LOCATE 10, 10

        PRINT USING "The program was stopped with the pressure at ###.## psi."; Pres

        LOCATE 12, 10

        PRINT "The target pressure was"; Target; "psi."

        PRINT : PRINT : PRINT

        END


'       -----------------------------------------------------------------

'       Error code interpreter


CallErrorCodes:


        SELECT CASE F%


        CASE 0

            Mes$ = "No error"

        CASE 1

            Mes$ = "Driver not initialized using Mode 0"

        CASE 2

            Mes$ = "Mode number out of range"

        CASE 3

            Mes$ = "Base address is out of range"

        CASE 4

            Mes$ = "MUX scan limits out of range"

        CASE 5

            Mes$ = "Channel number is out of range"

        CASE 6

             Mes$ = "A/D time out."

        CASE 7
```

APPENDIX D

```
     Mes$ = "Interrupt level out of range"
CASE 8
     Mes$ = "Mode 8 data transfer parameters out of range"
CASE 9
     Mes$ = "Mode 9 data transfer parameters out of range"
CASE 10
     Mes$ = "Counter number out of range"
CASE 11
     Mes$ = "Counter configuration number > 5 in mode 10"
CASE 12
     Mes$ = "OP# data greater than 15"
CASE 13
     Mes$ = "Trigger channel out of range"
CASE 14
     Mes$ = "Trigger level out of range"
CASE 15
     Mes$ = "Trigger slope not 1 or 0"
CASE (16 OR 17 OR 18 OR 19)
    Mes$ = "Not used"
CASE 40
     Mes$ = "Mode 55 configuration error"
CASE 41
     Mes$ = "Data out of range for modes 50 to 60"
CASE ELSE
     Mes$ = "No message for this error number"
END SELECT
RETURN
```

APPENDIX E

Plots of burst pressure versus the fourth power of the ratio, film thickness divided by diaphragm diameter. Plots are presented for sets DF-N1, DF-N2, DF-N4, DF-N5, and WF#25.

APPENDIX E

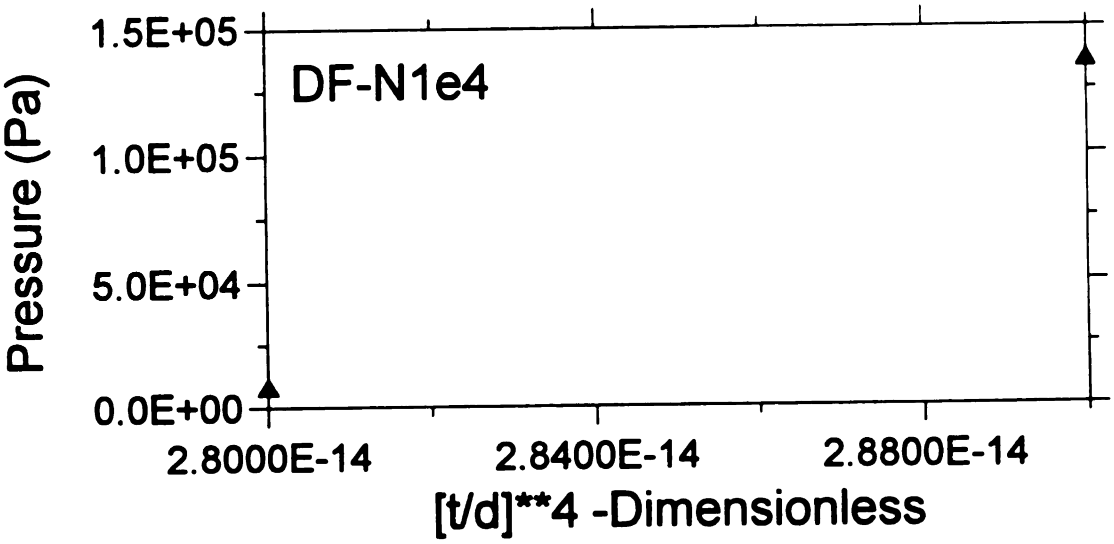

Figure E1. Insignificantly small data set DF-N1. Included only to complete appendix.

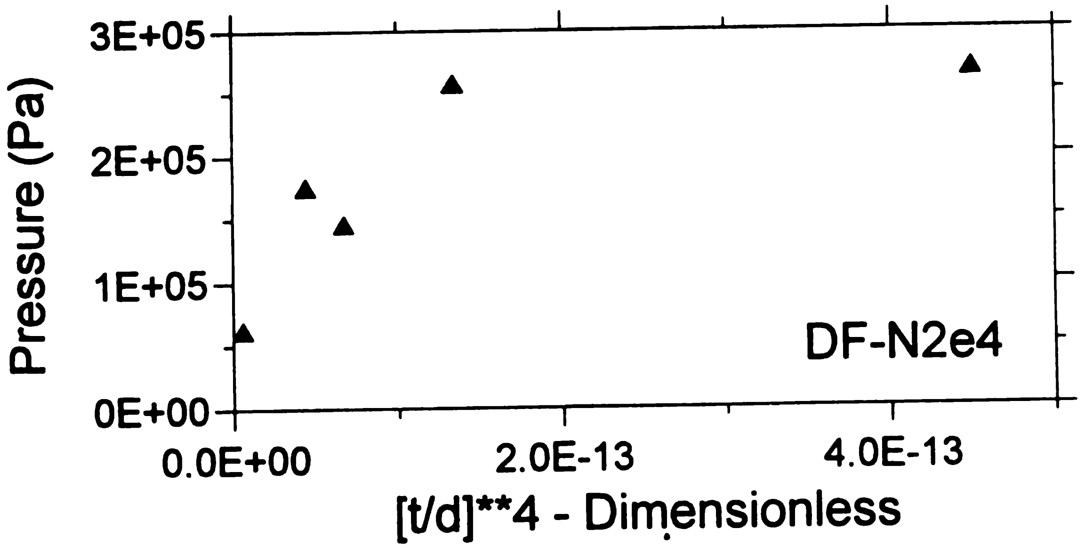

Figure E2. Plot of burst pressure versus the fourth power of the ratio, film thickness divided by diaphragm diameter for data set DF-N2.

APPENDIX E

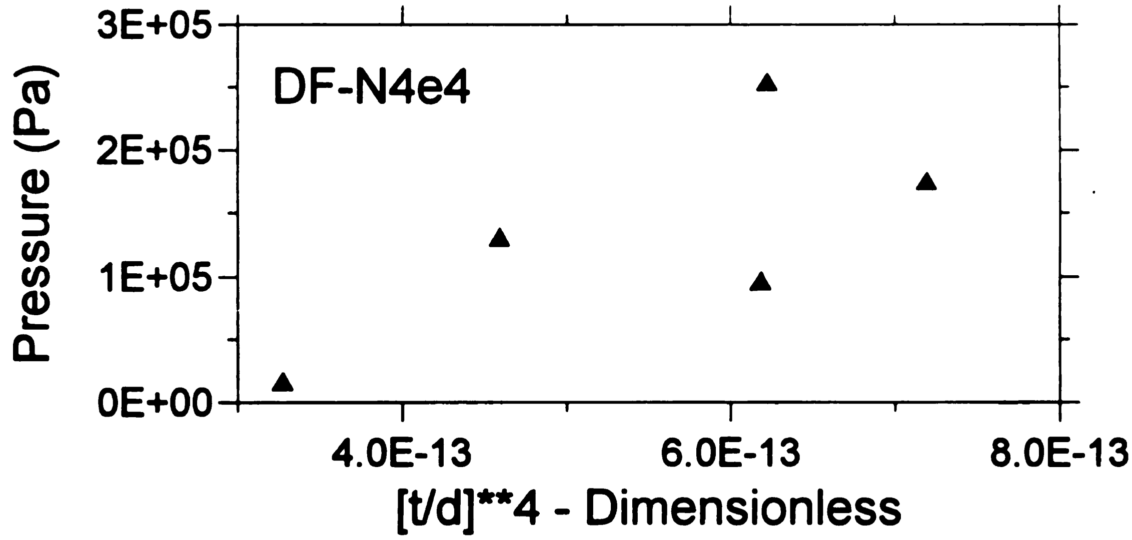

Figure E3. Plot of burst pressure versus the fourth power of the ratio, film thickness divided by diaphragm diameter for data set DF-N4.

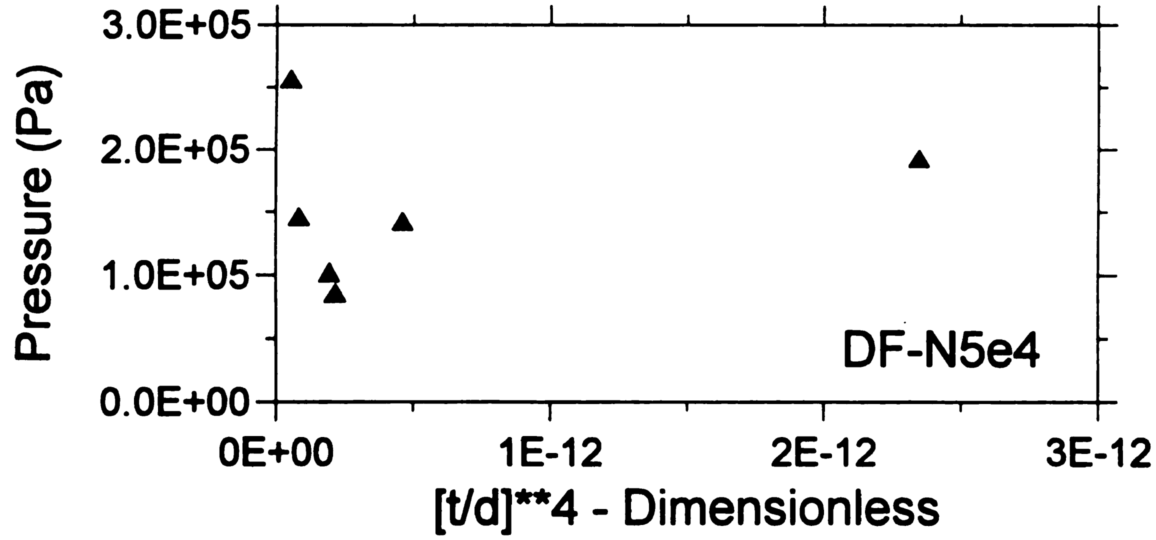

Figure E4. Plot of burst pressure versus the fourth power of the ratio, film thickness divided by diaphragm diameter for data set DF-N5.

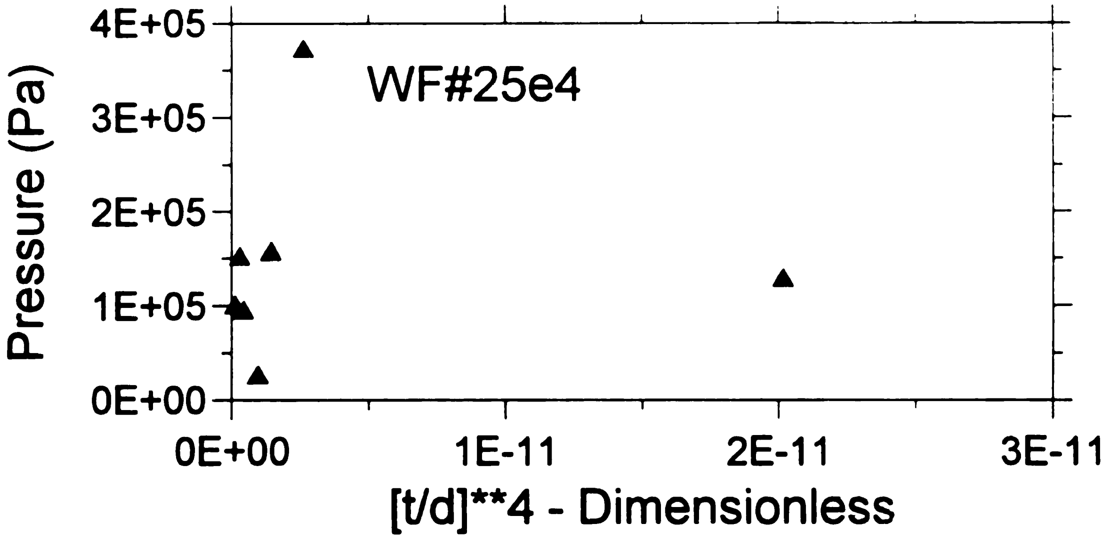

Figure E5. Plot of burst pressure versus the fourth power of the ratio, film thickness divided by diaphragm diameter for data set WF#25.

APPENDIX F

Plots of burst pressure versus the square root of the ratio, film thickness divided by diaphragm diameter. Plots are presented for sets DF-N1, DF-N2, DF-N4, DF-N5, WF#25, and WF#60.

APPENDIX F

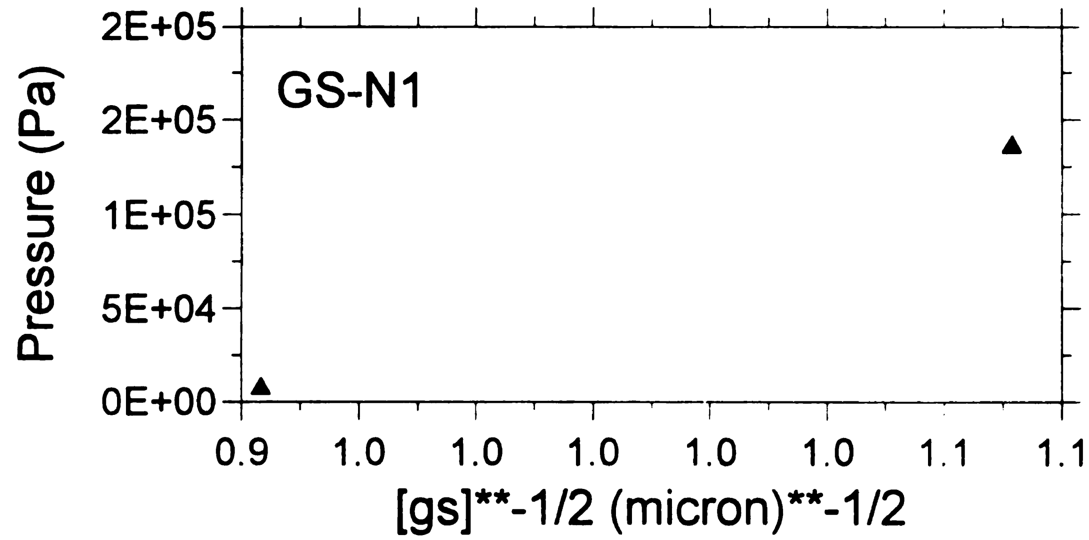

Figure F1. Insignificantly small data set DF-N1. Included only for the completion of Appendix F.

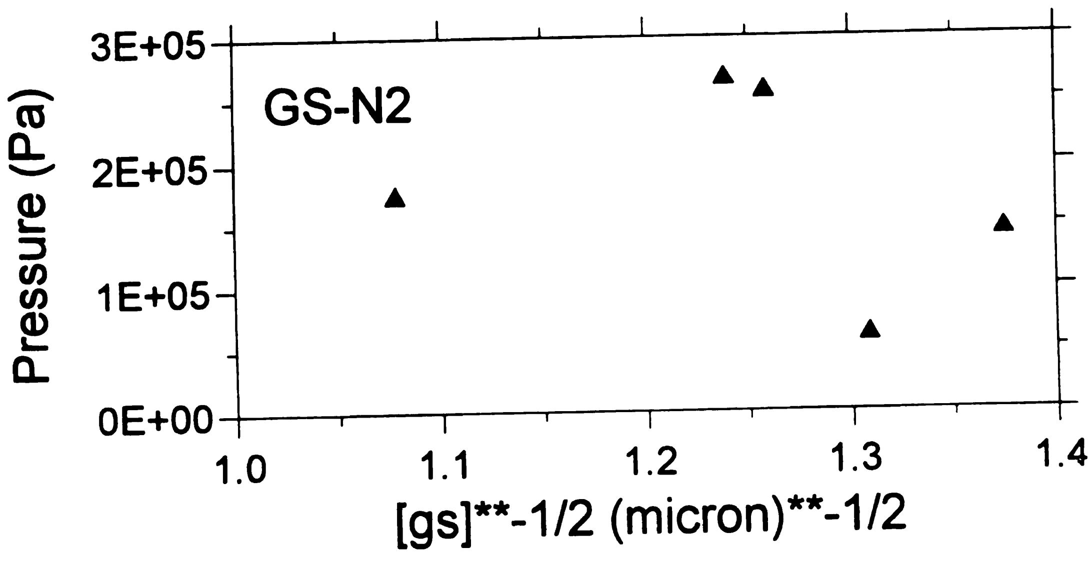

Figure F2. Plot of the burst pressure versus the square root of grain size for data set DF-N2.

APPENDIX F

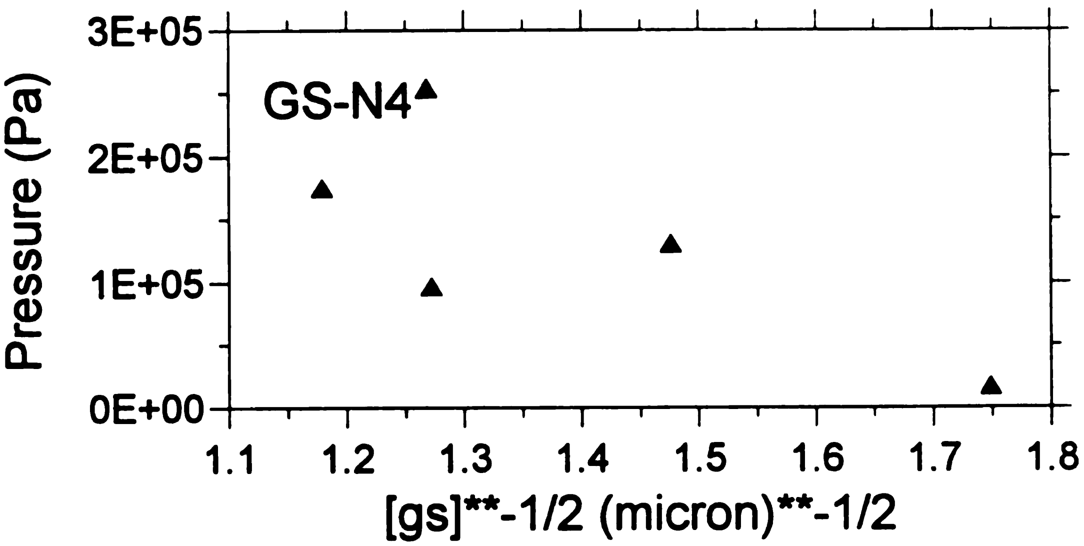

Figure F3. Plot of the burst pressure versus the square root of grain size for data set DF-N4.

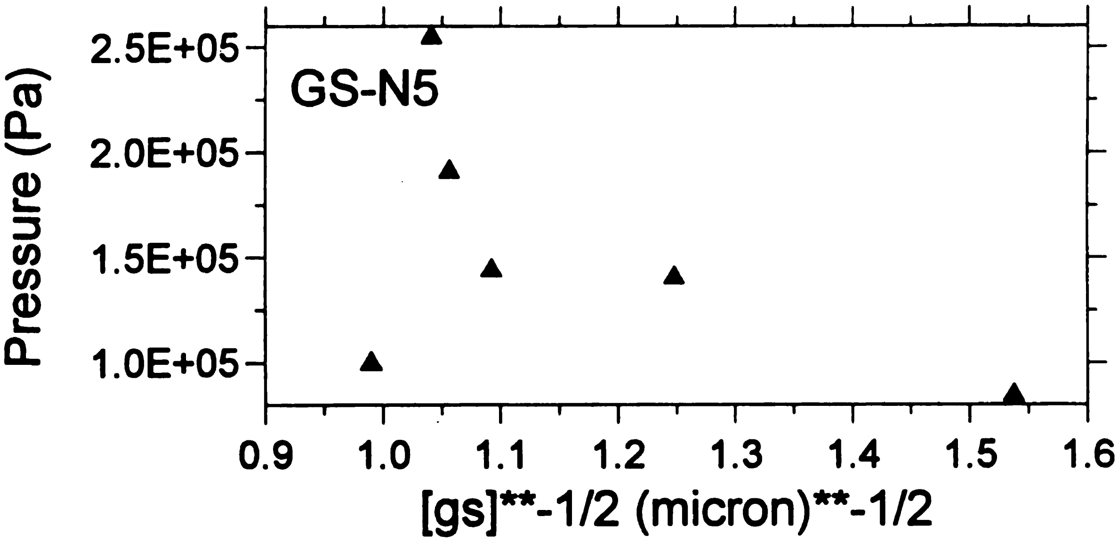

Figure F4. Plot of the burst pressure versus the square root of grain size for data set DF-N5.

APPENDIX F

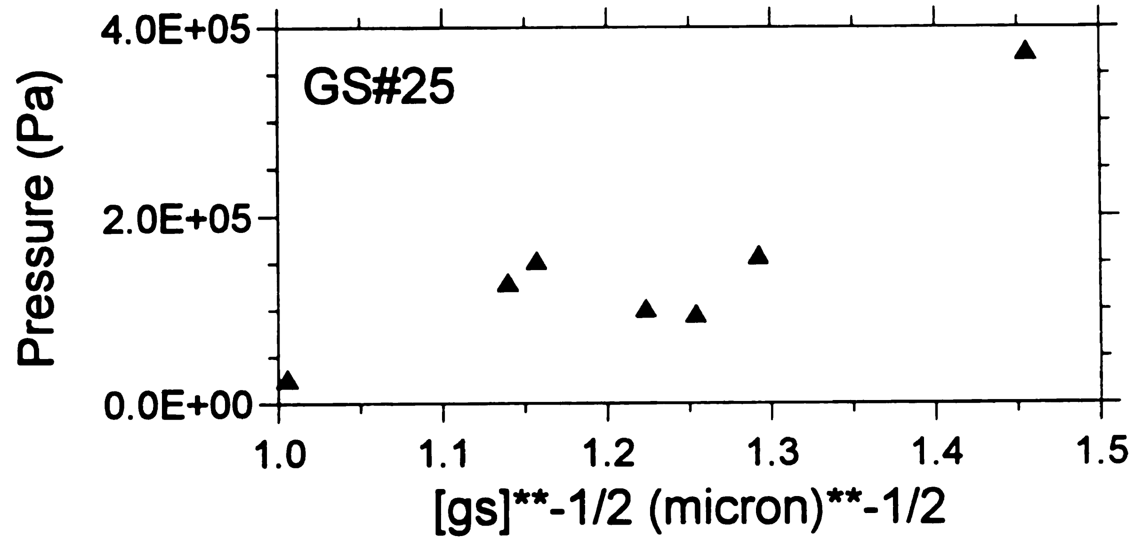

Figure F5. Plot of the burst pressure versus the square root of grain size for data set WF#25.

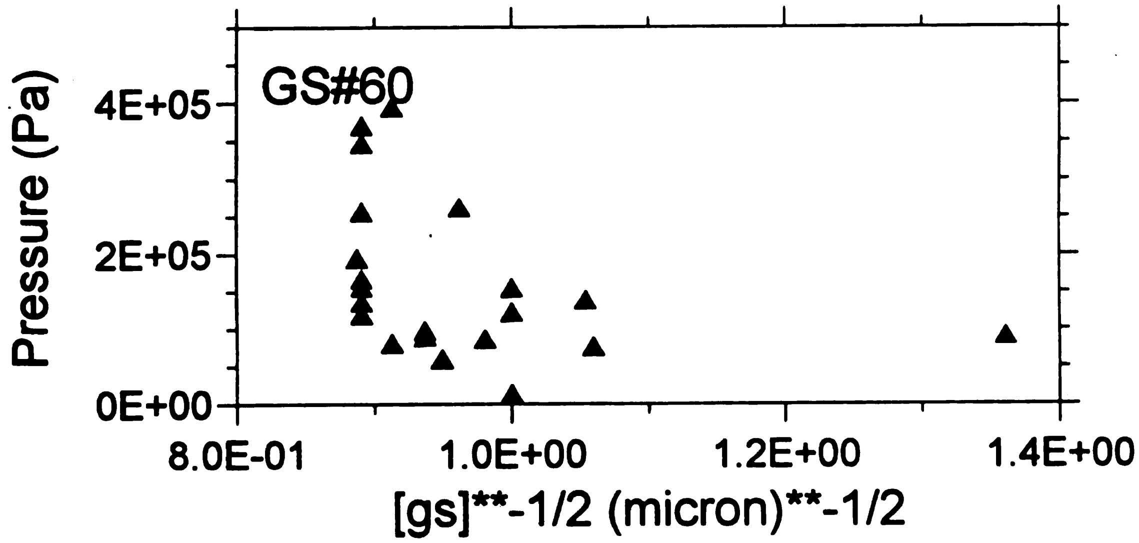

Figure F6. Plot of the burst pressure versus the square root of grain size for data set WF#60.

References

1. Life Application Bible, Tyndale House Publishers, Inc., Wheaton Ill., xii, (1988).
2. M.B. Hursthouse, J. Kane, and A.G. Massey, "Plastic Deformation and Anisotropy in the Hardness of Diamond", Nature, 228: 660-661, (1970).
3. R.M. Chenko and H.M. Strong, "Physical Property of Diamond", Report No. 75CRD089, General Electric Company Schenectady, N.Y.,October (1975).
4. Henry Windischmann and Glen F. Epps, "Properties of diamond membranes for x-ray lithography", J. Appl. Phys. 68 [11]: 5665-5673, (1990).
5. Karl E. Spear, "Diamond-Ceramics of the Future", J. Ceram. Soc., 72 [2], 171-191, (1989).
6. A. Masood, M. Aslam, M.A. Tamor, and T.J. Potter, "Techniques for Patterning of CVD Diamond Films on Non-Diamond Substrates", J. Electrochemic. Soc., 138, L67, (1991).
7. Michael Frenklach and Karl E. Spear, "Growth Mechanisms of Vapor-Deposited Diamond", J. Mater. Res., 3: 133-140, (1988).
8. Stephen J. Harris, "Gas-phase kinetics during diamond growth: CH_4 as-growth species", J. Appl. Phys. 65 [8]: 3044-3048, (1989).
9. Michael Frenklach, "The role of hydrogen in vapor deposition of diamond", J. Appl. Phys. 65 [12]: 5142-5149, (1989).
10. C.-P Chang, D.L. Flamm, D.E. Ibbotson, and J.A. Mucha. "Diamond crystal growth by plasma chemical vapor deposition", J. Appl. Phys. 63 [5]: 1744-1748, (1988).
11. John C. Angus, Herbert A. Will, and Wayne S. Stanko, "Growth of Diamond Seed Crystals by Vapor Deposition", J. Appl. Phys. 39 [6]: 2915-2922, (1967).
12. D.J. Pickrell, W. Zhu, A.R. Badzian, R.E. Newnham, and R. Messier, "Near-interface characterization of diamond films on silica", J. Mater. Res. 6 [6]: 1264-1277, (1991).
13. J.A. Mucha, D.L. Flamm, and D.E. Ibbotson, "On the role of oxygen and hydrogen in diamond-forming discharges", J. Appl. Phys. 65 [9]: 3448-3452, (1989).
14. H. Windischmann and Glenn F. Epps, "Intrinsic stress in diamond films prepared by microwave plasma CVD", J. of Appl. Phys. 69 [4]: 2231-2237, (1991).

15. B.S. Berry, W.C. Pritchet, J.J. Cuomo, C.R. Guarnieri, "Internal stress and elasticity of synthetic diamond thin films", Appl. Phys. Lett. 57 [3]: 302-303, (1990).

16. Xiang Xin Bi, P.C. Eklund, J.G. Zhang, and A.M. Rao, "Optical properties of chemical-vapor-deposited diamond films", J. Mater. Res. 5 [4]: 811-817, (1990).

17. Sumio Iijima, Yumi Aikawa, and Kazuhiro Baba, "Growth of diamond particles in chemical vapor deposition", J. Mater. Res. 6 [7]: 1491-1497, (1991).

18. Satya P. Chauhan, John C. Angus, and Nelson C. Gardener, "Kinetics of carbon on diamond powder", J. Appl. Phys. 47 [11]: 4746-4754, (1976).

19 T. DebRoy, K. Tankala, W.A. Yarbrough, and R. Messier, "Role of heat transfer and fluid flow in the chemical vapor deposition of diamond", J. Appl. Phys. 68 [5]: 2424-2432, (1990).

20. M.A. Tamor, "Practical control of CVD diamond film morphology: chemistry, geometry, and reality." *seminar*, Physics an Astronomy Bldg. Michigan State University, Oct. 29th, 1993.

21. Carol Gamlen, "Adherence of diamond thin films on silicon wafers and FTIR spectroscopy damaged ceramic materials.", Masters Thesis, Department of Materials Science and Mechanics, Michigan State University, (1990).

22. H. Keller, "Si-ExraKtionsoptik fur filamentlose Ionenquellen", Diplomar beit zum Thema, University of Wuppertal, Germany, June 1987.

23. Henry Webe, Graduate Student, Department of Material Science and Mechanics, Michigan State University, *created and installed software*, (1993).

24. Bill Glime, " Mechanical behavior of CVD diamond thin film diaphragms.", Master Thesis, Department of Materials Science and Mechanics, Michigan State University, (1994).

25. J. Zhang, Ph.D. candidate Electrical Engineering Department, *personal communication*, MSU, November 1993.

26. Walter A. Yardbrough and Russell Messier, "Current issues and problems in the chemical vapor deposition of diamond", Science 247: 688-695, (1990).

27. Stephen Timoshenko, Theory of Plates and Shells, 2nd ed., New York: McGraw-Hill, (1959).

28. Chuen-Yaun Chia, Nonlinear Analysis of Plates, 1st ed., New York: McGraw-Hill International Book Co., (1980).

29. B. Banerjee, "Large deflections of circular plates of variable thickness", Int. J. Solids Structures, 19 [2]:179-182, (1983).

30. R.F. Davis, Z. Sitar, B.E. Williams, H.S. Kong, H.J. Kim, J.W. Palour, J.A. Edmond. J. Ryu, J.T. Glass and C.H Carter, Jr., "Critical Evaluation of the Areas for Future Research Regarding the Wide Band Gap Semiconductors Diamond, Gallium Nitride and Silicon Carbide", Material Science and Engineering, BI, 77-104, (1988).

31. W.D. Kingery, H. K. Bowen, and D.R. Uhlmann, Introduction to Ceramics, 2nd Edition, Wiley-Interscience publication, 794, (1976).

32. Phillip A. Schmeitzer, "Corrosion Resistance Table: Metals, Nonmetals, and Rubbers", 2nd Edition, 90-97, (1986).